DISSERTATION

COMPUTATIONAL MODELING OF THE LOWER CERVICAL SPINE: FACET CARTILAGE DISTRIBUTION AND DISC REPLACEMENT

Submitted by

Wesley J. Womack

Mechanical Engineering Department

In partial fulfillment of the requirements

For the Degree of Doctor of Philosophy

Colorado State University

Fort Collins, CO

Summer 2009

COLORADO STATE UNIVERSITY

May 11th, 2009

WE HEREBY RECOMMEND THAT THE DISSERTATION PREPARED UNDER OUR SUPERVISION BY WESLEY J. WOMACK ENTITLED "COMPUTATIONAL MODELING OF THE LOWER CERVICAL SPINE: FACET CARTILAGE DISTRIBUTION AND DISC REPLACEMENT" BE ACCEPTED AS FULFILLING IN PART REQUIREMENTS FOR THE DEGREE OF DOCTOR OF PHILOSOPHY.

Committee on Graduate work

(Paul Heyliger)

(Susan James)

(Xianghong Qian)

Advisor (Christian Puttlitz)

Department Head (Allan Kirkpatrick)

ABSTRACT OF DISSERTATION

COMPUTATIONAL MODELING OF THE LOWER CERVICAL SPINE:
FACET CARTILAGE DISTRIBUTION AND DISC REPLACEMENT

Anterior cervical fusion has been the standard treatment following anterior cervical discectomy and provides sufficient short-term symptomatic relief, but growing evidence suggests that fusion contributes to adjacent-segment degeneration. Motion-sparing disc replacement implants are believed to reduce adjacent-segment degeneration by preserving motion at the treated level. Such implants have been shown to maintain the mobility of the intact spine, but the effects on load transfer between the anterior and posterior elements remain poorly understood.

In order to investigate the effects of disc replacement on load transfer in the lower cervical spine, a finite element model was generated using cadaver-based Computed Tomography (CT) imagery. The thickness distribution of the cartilage on the articular facets was measured experimentally, and material properties were taken from the literature. Mesh resolution was varied in order to establish model convergence, and cadaveric testing was undertaken to validate model predictions.

The validated model was altered to include a disc replacement prosthesis at the C4/C5 level. The effect of disc-replacement on range of motion, antero-posterior load distribution, total contact forces in the facets, as well as the distribution of contact pressure on the facets were examined, and the effect of different facet cartilage thickness models on load sharing and contact pressure distribution predictions were examined.

Model predictions indicate that the properly-sized implant retains the mobility, load sharing, and contact force magnitude and distribution of the intact case. Mobility, load sharing, nuclear pressures, and contact pressures at the adjacent motion segments were not strongly affected by the presence of the implant, indicating that disc replacement may not be a significant cause of post-operative adjacent-level degeneration.

Variation in articular cartilage distribution did not substantially affect mobility, contact forces, or load sharing. However, mean and peak contact pressure, contact area, and center of pressure predictions were strongly affected by the cartilage distribution used in the model. These results indicate that oversimplification of the cartilage thickness distribution will negatively affect the ability of the model to predict facet contact pressures, and thus subsequent cartilage degeneration.

Wesley J. Womack

Mechanical Engineering Department

Colorado State University

Fort Collins, CO 80523

Summer 2009

Acknowledgements

This work was supported by a grant provided by Synthes, to whom the author is greatly indebted. The guidance of Dr. Christian Puttlitz was essential in the preparation and editing of this manuscript, as well as in the design and execution of the experiments. The author would like to thank his committee members for their availability and guidance. The author would also like to thank Catherine Reid, Snehal Shetye, Ross Tichota, and Dan Woldtvedt for their help with physical experiments, Ugur Ayturk, Kirk Mcgilvray, and Brandon Santoni for help with experimental protocols and solution methods, and Mark Ringerud for faithfully maintaining the computer systems.

DEDICATION

This work is dedicated to my lovely wife Stefanie, who let me discuss calculus at the dinner table more than could be expected of a mere mortal.

TABLE OF CONTENTS

LIST OF FIGURES

LIST OF TABLES

List of Equations

1 Background

Anatomy of the Lower Cervical Spine

Geometry

The primary mechanical functions of the human spine include protection of the delicate spinal cord, transfer of mechanical loads from the head, muscles, and external loads to the pelvis, and the maintenance of structural stability and mobility of the spine. The normal human spine contains 24 vertebrae, which are divided into cervical, thoracic, and lumbar regions, and terminating caudally at the sacrum. The antero-posterior curvature of the spine facilitates its shock-absorbing ability, and varies according the region, being lordotic (curving toward the rear) in the cervical and lumber regions, and kyphotic (curving toward the front of the body) in the thoracic and sacral regions (Figure 1).

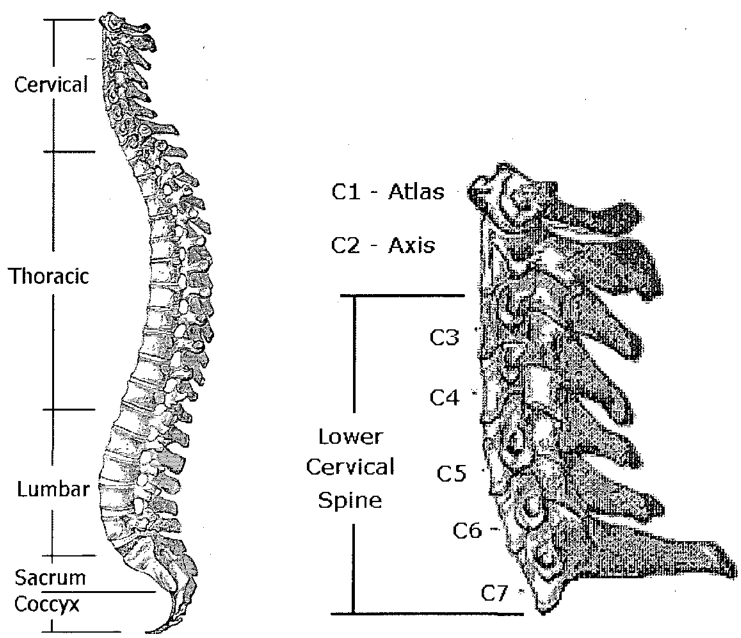

Figure 1 – Whole spine, denoting the major regions. Variation in lordosis and kyphosis is apparent (left). Cervical spine, including the atlas (C1) and axis (C2) (right). Adapted from Gray's Anatomy [36].

The seven cervical vertebrae are subdivided into the upper (occiput-C2) and lower (C3-C7) regions, which are easily distinguished by the unique geometry of the atlas (C1) and axis (C2) which contains a prominent process on the superior aspect, the dens. The five vertebrae of the lower cervical spine are similar in size and shape, having large transverse processes on both lateral aspects, which are perforated by transverse foramina through which vascular and nervous elements pass (Figure 2)[59].

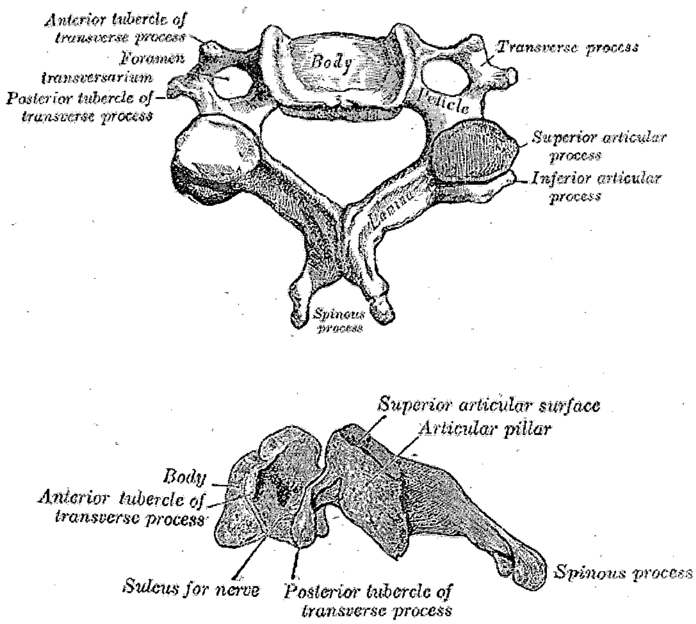

Figure 2 - Cervical vertebra, denoting the relevant anatomic features. Adapted from Gray's Anatomy [36].

The spinal cord is enclosed within the spinal canal, and protected at the posterior by the dense posterior process, which also serves as an attachment point for ligaments and musculature. The anterior body carries most of the compressive load applied to the cervical vertebrae, which is transferred through the intervertebral discs. The remaining fraction of compressive loads is transferred through the posterior facets, which are cartilaginous articulating joints. Joining the anterior body and the disc, the cartilaginous endplate provides a graded change in stiffness, as well as allows the passage of nutrients to the disc, which is avascular.

Several ligaments provide structural support for the lower cervical spine. The anterior longitudinal ligament (ALL) runs down the front of the spine, and is tightly bound to the surface of the vertebrae. Posterior to the disc, the posterior longitudinal ligament (PLL) plays a more active role during forward flexion. The ligamentum flavum (LF) spans the posterior aspect of the spinal canal, providing containment for the spinal cord (Figure 3).

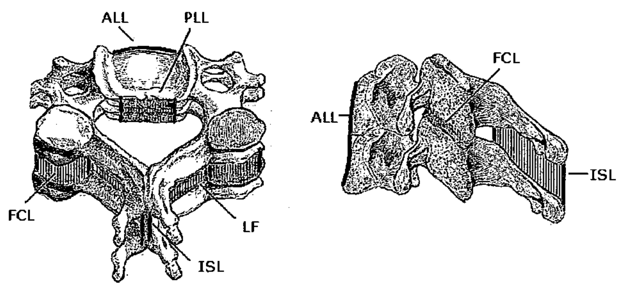

Figure 3 - Ligaments of the lower cervical spine – Adapted from Gray's Anatomy [36].

The posterior processes are connected by the interspinous ligaments (ISL), and the facet joints are encapsulated by the facet capsular ligaments (FCL), which provide support under lateral bending and torsional loads in addition to their function as a joint capsule [142]. Cryomycrotomy and radiographic and photographic techniques have been used to measure the geometric properties of the ligaments [142].

The intervertebral disc is of particular interest, and is itself divided into the outer annulus fibrosus and the nucleus pulposus. The hierarchical structure of the intervertebral disc plays an important role in its mechanical function, which is loaded principally in compression (Figure 4) [15,142].

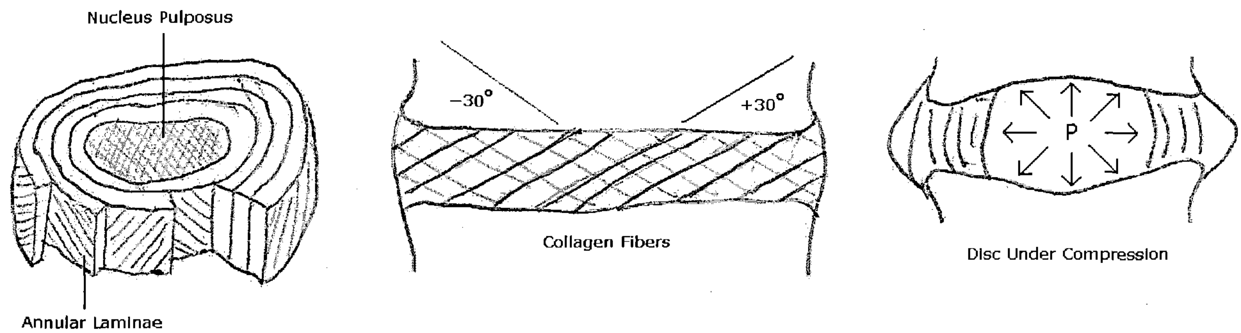

Figure 4- Schematic of the intervertebral disc, showing annular laminae with alternating fiber orientation. Adapted from Joshi [60].

As the disc is compressed, pressures generated in the more gelatinous nucleus induce circumferential stresses in the annulus fibrosus and bulging of the disc. In the cervical spine, the disc height at the posterior margin is approximately 50% of the anterior height [101]. The cross-sectional area of the nucleus, 1-2 cm^2 in the cervical spine, increases caudally, representing 25% of disc in the cervical spine and 50% in the lumbar region [76, 101, 142].

A feature unique to the cervical spine is the presence of uncinate processes, which are raised lateral margins at the superior surfaces of the anterior bodies. Another unique feature of the cervical spine is the development of uncovertebral clefts, also known as Lushka joints, at the lateral aspects of the intervertebral disc at mid-height [76]. Uncovertebral clefts develop as fissures at the lateral aspects of the disc in areas proximal to the uncinate processes that experience high torsional stresses, generally at age 9-14 [76]. Debate continues as to whether these clefts should be considered degenerative effects or true synovial joints [142].

The lateral facets carry a substantial fraction of the compressive loads in the cervical spine, and are responsible for the coupled rotations between torsion and lateral bending [86]. The lateral facets of the cervical spine are elliptical in shape, with aspect ratio increasing caudally from 1.0 at C3 to 1.6 at C7 [88, 91]. The facets are oriented obliquely to both the sagittal plane (70 deg at

C3 to 94 deg at C7) and the transverse plane (45 deg at C3 to 65 deg at C7) [91, 88]. Significant variability in facet orientation has been observed, and asymmetric facet orientation has been correlated with disc degeneration [88]. The facet joint may become dislocated or 'locked' due to high combined flexural and torsional loads – around 10 N-m, compared to the physiologic load range of approximately 2 N-m. This loading scenario may result in damage to the germane soft tissues and significant instability after reduction of the dislocation [21]. The cervical facets are approximately 12 mm wide, and are covered with a layer of articular cartilage with spatially varying thickness up to 0.5 mm [91, 141].

The lordotic curvature of the cervical spine has been measured radiographically and described in terms of radius of curvature and intersegmental relative rotation angle (RRA, 6-7 deg) and total cervical lordosis or absolute rotation angle (ARA, 44 deg, Figure 5)[9, 44, 45, 63].

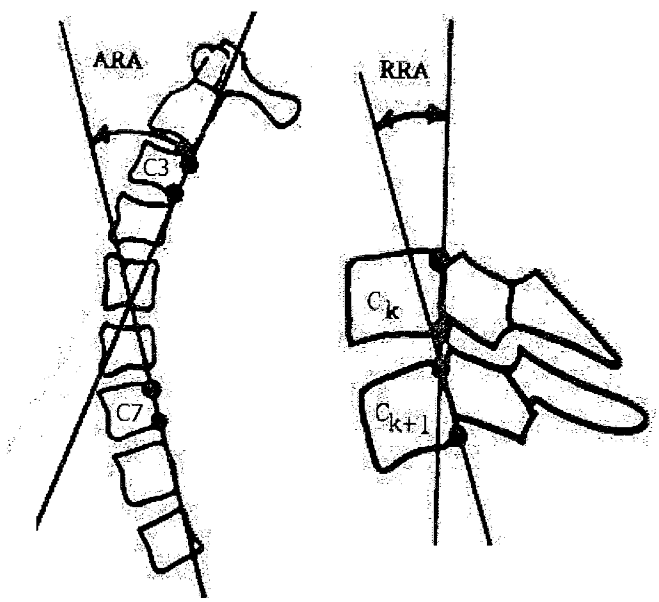

Figure 5 - The cervical lordotic curvature, showing absolute and relative rotation angles – adapted from Harrison et al. [45]

However, substantial variability exists in observed cervical lordosis in the asymptomatic spine, which varies with age [44]. While much effort is spent to correct abnormal sagittal curvatures, some researchers have found that a loss of lordosis may not be well correlated with symptoms such as pain and disability, with asymmetry being more common than not [44]. This indicates that pain and/or loss of mobility are preferred to radiographic lordosis as measures of clinical interest.

The anterior bodies of the cervical vertebrae are composed mostly of spongy trabecular (cancellous) bone within a thin cortical shell. Osteoporosis is known to result in a thinning of the cortical shell in addition to disadvantageous changes in the structure and density of the cancellous bone [96]. The cortical shell thickness of the anterior body in the lower cervical spine is 0.4-0.7 mm, and exhibits systematic variation spatially and between levels and anatomic locations [96]. Much thicker cortical bone is observed in the posterior elements.

Material Properties

Cortical and Trabecular Bone

Both cortical and trabecular bone are complex multiphase composite materials with hierarchical molecular and geometric structures at relevant scales from 2 nm to 500 μm [110]. Organic phase constituents (principally type I collagen fibers) embedded in an apatite matrix (calcium phosphate and calcium carbonate) are arranged in a complex lamellar haversian structure, the interaction of which contributes significantly to the bone's toughness [13, 110, 140]. Water accounts for some 20% of the wet weight of bone, while the mineral phase constitutes 77% of the remainder [13]. 90-95% of the organic phase consists of collagen (Figure 6) [13].

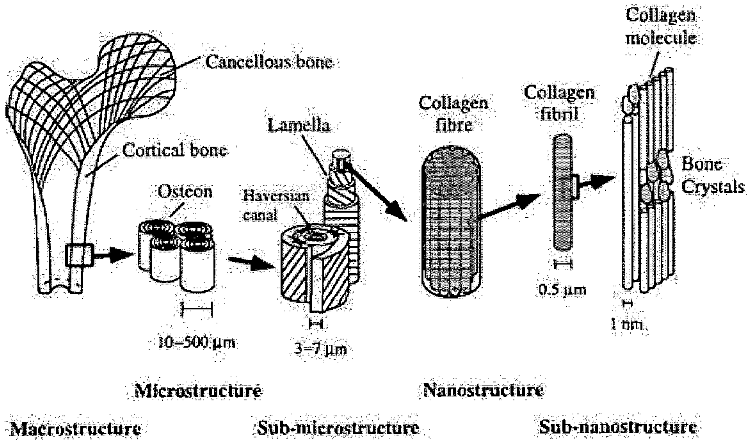

Figure 6 – Schematic of the hierarchical structure of bone [110]

Bone exhibits a capacity for self-repair, as new bone is deposited and tissue is resorbed through the remodeling process [13, 83]. The elastic properties of cortical bone vary with species, age, orientation, loading rate, and anatomic location [22, 108, 137]. The density, strength, and elastic moduli of trabecular bone have been positively correlated with computed tomography (CT)-based density measurements, and widely varying linear, polynomial, power, and exponential relationships have been proposed [49, 108]. Correlation of CT density to elastic moduli is less significant in cortical bone, although a positive linear relationship has been observed [22]. This may be due to the much greater variability in density and elastic parameters observed in trabecular bone [108]. Elastic moduli for trabecular bone vary with density from 0-4000 MPa, and 10-20 GPa for cortical bone [13, 22, 49, 108]. Additionally, the stiffness and strength of cortical bone increase logarithmically with loading rate and decrease with age [137, 150].

Differentiation between dense trabecular bone and cortical bone can be arbitrary, and is usually distinguished on the basis of porosity. Cortical bone is 5-30% porous (nonmineralized), while trabecular bone may exhibit more than 90% porosity [13]. Denser trabecular bone is observed radiographically in the posterior elements than in the anterior bodies. Additionally, the trabecular spicules in the anterior body exhibit a preferred axial orientation commensurate with their primary mechanical loading configuration, resulting in some anisotropy in the elastic parameters. The macroscopic structure of cancellous bone consists principally of interconnected plates and spicules, the thickness and connectivity of which vary with age and apparent density. Cortical and cancellous bone exhibit similar properties and characteristics at a microscopic level, with apparent-level differences that are largely attributable to differences in macrostructure [13].

Intervertebral Disc

The annulus is composed of approximately 35 distinct concentric lamellae, which vary in thickness both as a function of radial and angular position, from 130 to 300 μm, with thickness increasing inward [15]. The lamellae are unidirectionally reinforced by collagen fibers which provide the major component of circumferential stiffness to the annulus. The collagenous fibers of the annular lamellae are oriented at a 30 to 45 degree angle to the horizontal, and the fiber angles alternate between successive lamellae in a composite layup structure [66]. Additionally, the fiber orientation varies with radial position, from +- 30 deg at the outermost lamellae to +- 45 deg adjacent to the nucleus [57]. Fiber orientation and structure in the annulus has been verified using a variety of techniques, including transmission optical microscopy, electron micrography, diffusion tensor microscopy and cross-polarization techniques [15, 51, 55, 57, 101]. The collagen fibers themselves exhibit a planar crimped morphology with a period of 20-26 μm and a crimp angle that varies from 20 degrees at the perimeter to 45 degrees at the innermost lamella [15]. The fibers are structurally anchored to the cartilage endplates, restricting their radial expansion [15]. Reinforcing fibers in the annulus are composed of both type I and type II collagen, varying from 95% type I at the perimeter to 95% type II at the nucleus

[15]. The fibrils themselves range in diameter from 10 to 40 nm, which may be related to changes in glycosaminoglycan content during development as well as the critical length for load transfer from the ground substance to the reinforcing fibers [51].

The molecular structure of the collagen fibers in the annulus, combined with their ply layup structure, results in a highly nonlinear, anisotropic and hyperelastic mechanical behavior for the annulus. Radial tensile and confined compression testing of annulus reveals the hyperelastic behavior of the annulus matrix ground substance [66]. Axial and circumferential testing of individual annular lamellae and multi-lamellar samples demonstrates that mechanical response of the collagen fiber component of the annulus is much stiffer than the ground substance. Significant anisotropy has been ascribed to the fiber orientation, such that the annulus is approximately 100 times stiffer circumferentially than radially [54, 66].

The youthful nucleus pulposus is a gelatinous material composed largely of water (88%), proteoglycans, and type II collagen [15, 87]. The material and mechanical properties of the nucleus pulposus vary with age, becoming generally stiffer and less hydrated as degeneration progresses. Differentiation between the annulus and nucleus in the severely degenerated nucleus becomes obscured; after age 55 the nucleus pulposus is largely fibrous, particularly in the cervical region [76]. In the annulus, severe tears develop with degeneration, and along with proteoglycanous cysts, may lead to nuclear exudation and nerve compression [66].

Articular Cartilage

The articular cartilage of the lateral facets is a complex multiphase structure consisting of several constituents and multiple layers. It is porous and permeable, and exhibits viscoelastic and hyperelastic mechanical behaviors, as well as orthotropic and asymmetric tension-compression behavior [64]. The porous solid phase consists principally of collagen fibers and proteoglycans [3]. The fluid phase, which constitutes 70-90% of the cartilage mass, is able to move along pressure gradients, resulting in viscoelastic behavior. Swelling pressure is maintained by the presence of hydrophilic proteoglycans in the solid phase [3, 4]. Equilibrium moduli of 0.13 to 1.9 MPa have been observed. The modulus varies inversely with water content, as reduced solid phase content provides less resistance following liquid phase exudation [3]. Instantaneous moduli vary from 1 to 40 MPa and are functionally dependant upon strain and orientation. Poisson values range from 0.05 to 1.3 [3]. Structurally, articular cartilage consists of superficial, middle, and deep zones, which differ in collagen fiber orientation and density, as well as the content and morphology of chondrocytes.

Physiologic strains up to 14% have been recorded in articular cartilage, which is unsurprising given the relatively low modulus and substantial in vivo contact pressures (2-12 MPa, [4]). Proteoglycan-induced swelling pressures and interstitial fluid contribute heavily to the hyperelastic response, preventing excessive compressive strains [4].

Ligaments

The ligaments of the cervical spine are innervated structures that serve to provide structural stability while maintaining physiologic mobility [127]. The nonlinear elastic response of the ligaments maintains the integrity of the spine under traumatic loads [142, 95]. The principal constituents of the ligaments are the organic molecules collagen and elastin, which are arranged parallel to the ligaments in varying proportions, such that the elastic moduli of the cervical ligaments range for 3-45 MPa [142]. The ligaments support load only in tension, but exhibit varying amounts of pretension in the neutral position [142]. The cervical spine exhibits substantial mobility, and ligament strains during normal motion may exceed 30%, with failure occurring at extension of 3-13 mm [95, 127]. Substantial variation exists in experimentally reported ligament strain values, largely due to inter-observer variation in the choice of gage length and ambiguity in defining the neutral position when testing excised ligaments. For example, the anterior longitudinal ligament runs the length of the lower cervical spine, with insertion sites at the anterior aspect of each vertebra and spanning the disc spaces. Some researchers consider the distance between endplates as the reference length because the ligament is attached there, while others consider the anterior mid-height positions of the spanned vertebrae as endpoints, because the ligament is not truncated at the endplate [95, 142]. Additionally, both bone-ligament-bone constructs and ligament-only test configurations have been used [78]. When using ligament stress-strain data in mathematical models, it is critical that the model definition of ligament geometry is in agreement with the definition used in the material response dataset selected.

Both the presence of elastin and the crimped architecture of collagen contribute to the nonlinear toe region of the ligaments [127]. The cervical ligaments vary in length, modulus, and cross-sectional area, with failure loads ranging from 30-250 N, which varies substantially due to anatomic location [127].

History of Disc Arthroplasty

The historical standard treatment program for patients with symptomatic degenerative disc disease in the cervical spine is anterior cervical discectomy and fusion (ACDF), with over 187,000 anterior cervical spine procedures performed annually in the United States [24, 79, 102, 124]. However, there is growing concern that spinal fusion may increase the propensity toward progressive degeneration in the adjacent motion segments [70, 87, 99]. Cadaveric studies have shown increased intradiscal pressures and intersegmental motion at adjacent segments following ACDF [70, 111]. Clinical studies reveal long-term adjacent-level degeneration rates of 25-50%, with repeat operation rates of 6-17% [24, 70, 102, 111]. However, while radiographic adjacent-segment changes consistent with instability have been noted after ACDF, the effects are not consistently associated with the presentation of recurrent symptoms; thus it is as yet uncertain to what degree ACDF is responsible for subsequent symptoms as opposed to the natural progression of spondylosis [25]. Notably, the primary goal of ACDF is the relief of neural compression, fusion being a means to that end rather than a primary surgical goal [70, 124]. The increased degeneration rate at adjacent levels following ACDF has motivated a move toward treatments that maintain the intact mobility and load distribution.

The first human cervical arthroplasty was attempted in 1966 by Fernström with poor results [70, 87]. Many motion-preserving spinal implants have been developed since 1950, chiefly for the lumbar spine [70]. In 1989, the metal-on-metal ProDisc design was introduced with favorable results – more than 70% of patients report good results 10 years post-operatively [70]. The updated ProDisc II design was introduced some ten years later. In 1991, clinical trials for the Cummins-Bristol implant were initiated, and 5-year results indicated that while motion was preserved for most patients, dysphagia (difficulty swallowing) developed in all patients [102, 111]. The Prestige disc slimmed down the bulky anterior profile of the Cummins-Bristol design, and reports indicate that motion is preserved and adjacent-level degeneration is reduced relative to ACDF (Figure 7)[70, 124].

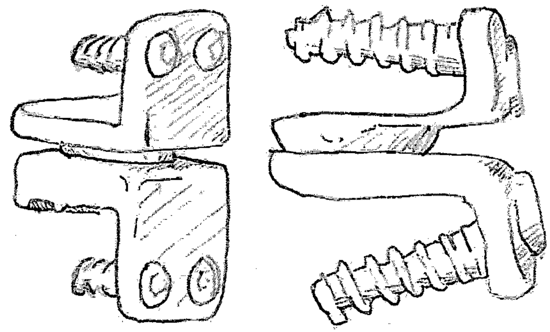

Figure 7- Bristol-Cummins disc (left), Prestige Disc (right)

The Bryan disc, for which US clinical trials were initiated in 2002, utilizes a polyurethane core between two porous titanium endplates. Clinical success rates of over 85% have been reported [70, 124]. Preliminary clinical results (2003) for the similar porous coated motion (PCM) device indicate good results as well [70]. Recently, the metal-on-polyethylene ball-and-socket ProDisc-C was introduced, having a plasma-sprayed central keel for the provision of implant stability (Figure 8)[70, 124].

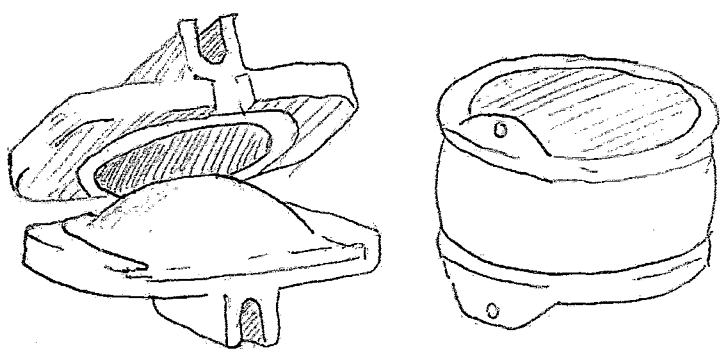

Figure 8 – ProDisc-C (left), and Bryan disc (right)

The demands placed on spinal motion-preserving implants are high – the implant must maintain both the intact antero-posterior load distribution profile and instantaneous center of rotation, and will undergo as many as 30 million cycles during its lifetime [70]. Additionally, devices must maintain both stability and mobility [87]. Biomaterials considerations include concerns for friction, toughness, strength, toxicity, resistance to corrosion, inflammatory response to wear debris, and desirable bone ingrowth at the endplates [87, 124]. As such, cervical disc implants tend to utilize the same materials as other orthopedic implants – titanium, stainless steel, UHMWPE, ceramics, cobalt-chromium-molybdenum alloys (CoCrMo), and hydroxyapatite and related coatings [87, 124]. While the foreign-body response to wear debris causing osteolysis is the primary causal factor for loosening requiring revision surgery, the volumetric wear rate for disc replacement implants (<1 mm^3/year) is much less than that observed in hip arthrodesis (50-100 mm^3/year) for which wear debris is a significant problem [87, 124].

Clinical Outcomes

Changes in sagittal alignment (loss of lordosis) after ACDF have been associated with adjacent-segment degeneration and other adverse affects, but it is unclear as yet whether the same relationship exists when mobility is maintained [62, 99, 102]. A prospective radiographic and clinical study in 2004 on patients receiving the Bryan disc showed an average ROM at the implanted level of 8.3 deg after 1 year, although a mean segmental *kyphosis* of 6.1 deg was observed postoperatively at the focal level [99]. Interestingly, while segmental lordosis was not maintained, ROM was, and more than 90% of patients reported positive outcomes after 1 year [99]. Another study using the Bryan disc resulted in loss of lordosis, again commensurate with good to excellent outcomes and restored ROM [118]. It has been proposed that the surprising increase in mobility at *all* cervical levels following arthroplasty may be due to the relief of preoperative pain [25]. Preliminary and long-term results following implantation of the Prestige I & II showed positive outcomes and maintenance of mobility with no evidence of adjacent-level degeneration [102, 111]. Cadaveric studies using the ProDisc-C resulted in little change in ROM, while clinical results indicate some reductions in ROM over time [24]. Both ACDF and arthroplasty significantly reduced pain over both the immediate and long-term [24].

Finite Element Modeling of the Lower Cervical Spine

The principal motivations for use of finite element methods in biomechanics include repeatability, absence of inter-specimen variability, ease of parametric variation, the ability to examine experimentally inscrutable data, and cost and time savings [11, 43]. The finite element method (FEM) was first applied to the vertebral column in 1973, with the earliest (2-D) models treating vertebrae as rigid masses [143]. Later 3-D models used simplified representations of bone geometry, with planar facets and identically-shaped vertebrae [20]. Most models have failed to represent the Lushka joints and uncinate processes altogether, which has been shown to have a substantial effect on model predictions [20]. Many models utilize geometry with idealized geometry produced by CAD packages rather than directly from anatomic imagery data. This approach improves meshing repeatability and substantially decreases the time required for mesh generation, but oversimplification of relevant geometric factors can degrade the utility of the models generated [43]. Geometry of the highest fidelity models has been based on qCT, MRI, and cryomicrotome data [11, 84, 143].

Cervical spine models generally apply pure moment (0.5-2.0 N-m), axial compression, or mixed loading conditions [67, 143]. Axial loading may be applied as a point load, a follower load, through thermal strain in cable elements, or by other means.

Material Properties

Cortical bone has generally been modeled as isotropic and linearly elastic, with E=10-15 GPa and ν=0.2-0.39 [11, 48, 105, 143]. Trabecular bone has generally been modeled as a single set of elements with E=100-500 MPa and ν=0.2-0.39, although some researchers have included variation in trabecular modulus with density [11]. The endplates of the anterior body have been modeled as cortical bone, as 2-D shell elements, and as an independent isotropic elastic material with E=500-2000 MPa and ν=0.3-0.4 [20, 84, 143]. The nucleus pulposus has been variously modeled as linearly elastic (E=0.2-200 MPa and ν=0.4-0.4999), hyperelastic, and as an incompressible fluid, and porosity/permeability is sometimes included [20, 84, 119]. Some authors have not distinguished between annulus and nucleus [48, 142]. Annulus fibrosus has been modeled variously as a homogenous linearly elastic isotropic or orthotropic material with E=3.4 MPa and ν=0.4, and with invariant-based strain energy formulations (Neo-Hookean, Mooney-Rivlin, etc) [67]. Other researchers seeking to accommodate the anisotropy of the annulus have utilized discretely fiber-reinforced structural finite element models with either linearly elastic (E=2.6-12.3 MPa, ν=0.35-0.45) or hyperelastic/poroelastic matrix formulations and linear or nonlinear spring or truss elements for the fiber families, which are arranged as 4-6 pairs of concentric rings. [26, 43, 67, 84, 125, 143]

Representation of the anisotropic behavior of the annulus requires either an anisotropic elastic or strain energy formulation or discrete structural fiber reinforcement [72]. Nearly all FEM's using discretely fiber reinforced annuli model the fiber elements as being directly connected to individual nodes of the solid matrix elements [125]. While this method has its advantages, it does not permit the experimentally observed variation in interlamellar angle with radial position to be controlled. Additionally, angular variation in the thickness of the annulus must either be neglected or result in unaccounted variation in fiber angle [125]. Using a single set of material properties for spring-based fiber elements induces additional inaccuracy due to variation in disc thickness. Additionally, few researchers have modeled the initial swelling pressure in the disc, which is relevant in that it places the annular fibers under some tension in the neutral position; models including this factor generally do so using pore pressure methodology [84].

The facet joint has been modeled using simple gap elements, and using linearly elastic (E=3.4-30 MPa and ν=0.45-0.49) and hyperelastic/poroelastic cartilage with contact formulations [20, 134, 143]. Nearly all models utilize idealized representations of facet geometry as flat or cylindrical [119]. Cartilage has generally been modeled as a single-element thick extrusion, and some researchers have neglected facet cartilage altogether, using gap elements with thickness [119]. It is clear that the cartilage thickness distribution, shape, and degree of conformance of the lateral facets are relevant parameters for the prediction of contact pressures, cartilage stresses, and coupled motions.

The ligaments of the cervical spine have been modeled as linearly elastic (E= 0.2-185 MPa and ν=0.3-0.36) and hyperelastic solids and 2-D shells, and as discrete linear and nonlinear springs [67, 105, 142, 143]. Some researchers have included a toe region, while few have included ligament pretension [11]. Discrete representation of the ligaments carries the advantage that unrealistic shear stresses are not induced under physiologic shear strains.

Convergence and Validation

Few published finite element models present convergence data, and many, by inspection, are superficially very coarse [48, 67, 119]. Experimental validation is a key, and often neglected, step in mathematical modeling [11, 143]. While it is most common to utilize load-deflection and coupled rotation results as validation metrics, it is important to validate the ability of any model to predict the specific parameters of interest [84, 105, 143]. For example, it is not possible to validate contact pressure distribution predictions in the facet joint based on ROM data, which is relatively insensitive to the degree of congruity of the articulating surfaces [119]. Additionally, parametric studies have shown that overall ROM and disc stress data are insensitive to variation in the bony elements, indicating that ROM data cannot be used to validate predictions of relevant endplate stresses [67]. It is useful to provide validation under a variety of load cases and conditions in order to verify that one has not merely observed coincidental agreement between the experimentally observed and model-predicted data. It should be noted that while finite element models are frequently used to elucidate data that are not experimentally measurable for validation or otherwise, some appropriately justified validative metric must still be applied [26]. For this reason, internal interpolative and extrapolative validation methods are commonly used in attempts to quantify the external extrapolative power of a model [129]. Metrics used for validation of pertinent data must constitute conditions for accuracy that are not only necessary but sufficient.

Specific Aims

Three specific aims were developed for this research effort.

1. Develop an experimentally validated and converged finite element model of the lower cervical spine (Chapters 2-4)
2. Examine the effects of facet cartilage thickness representation on contact parameters and kinematics (Chapter 5)
3. Examine the effects of disc replacement on load transfer at the treated and adjacent levels (Chapter 6)

2 Model Generation

Geometry

Bony Geometry

The bony geometry of the finite element model was prepared from cadaveric qCT imagery data [43]. One fresh-frozen cadaveric cervical spine (Female, 64, 164 lbs, 5'7") was scanned at 0.5 mm transverse resolution in 1.0 mm increments [43]. Amira visualization software (Mercury Computer Systems, Chelmsford, MA) was used to generate surface representations of the bony geometry based on Hounsfield attenuation values, which ranged from -1217 to 2124 for the dataset. Intensity querying was performed in order to determine an appropriate HU value (350) for thresholding of the bony exterior [37]. Imagery information external to the bone was masked, and the mean (698) and RMS (817) HU values of the bone were determined (Figure 9).

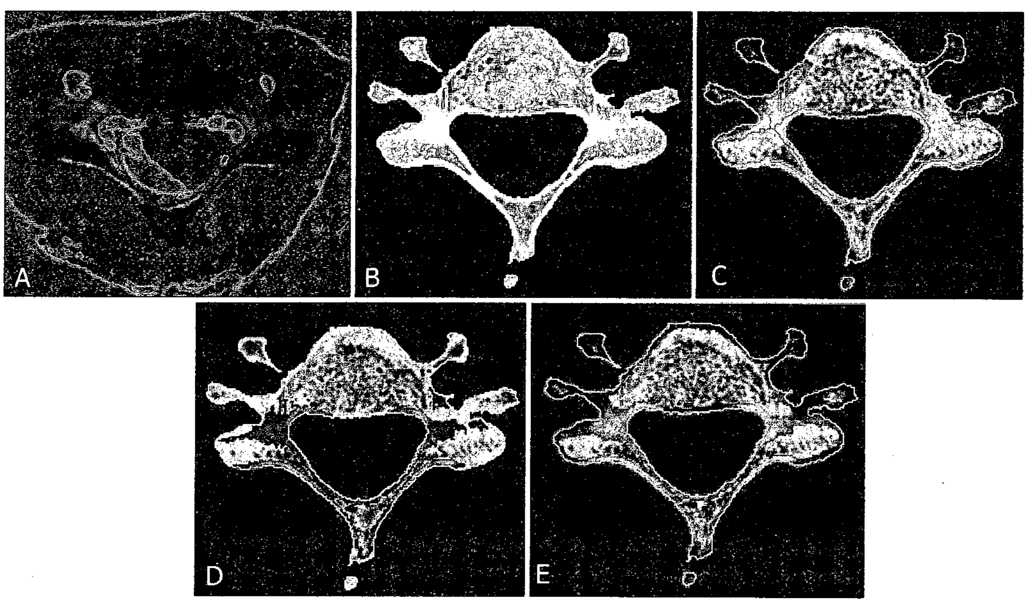

Figure 9 - Image segmentation process for a representative slice. A) Bone is selected B) and masked, C) shell offset, D) threshold volume, and E) final cortical volume.

The difference between the mean and RMS values is indicative of the presence of void space in the trabecular region, which is reflected as voxels with negative HU values. Image intensity values were probed along a line penetrating the cortical shell, and gradient-based thresholding was used to determine the threshold HU value for optimal recognition of the cortical shell. Due to variation in the HU density of the cortical shell as well as localized perforations, pure thresholding could not be used for cortical shell segmentation. A volumetric growing technique was used to select a constant thickness volume along the perimeter of the bone of 1-5 voxels thickness. Comparison with the cortical threshold value revealed that a 3-voxel shell provided an optimal representation of the cortical shell in the thinnest region, the anterior body, which also exhibited the lowest density cortical bone [96, 143]. Cortical bone that was not selected in this manner was added to the segmentation set by thresholding voxels over 1000 HU and utilizing island-removal techniques. Threshold values of 500-1500 were examined in this manner. Voxel segmentation was verified by comparison with the raw imagery.

Voxel segmentation sets were used to generate triangular surface (.stl) data, which were compared to the raw imagery for verification. Vertebral orientations were calculated by fitting lines to the anterior, posterior, dorsal and ventral aspects of the anterior bodies, and intervertebral relative rotations and overall lordosis were compared to published data (Figure 10)[9, 45, 92, 96]. Ten centrally-located section planes were sampled for each vertebra. Custom-written software was used to rotate the surfaces such that the anatomic planes of the spine were optimally oriented with the imagery coordinate system.

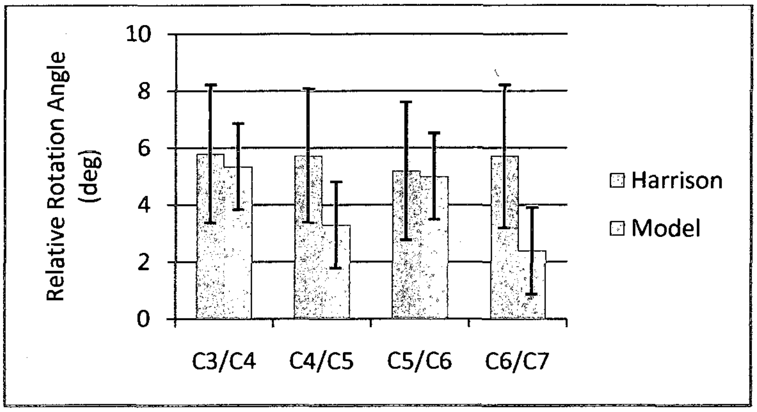

Figure 10 - Intersegmental relative rotation angles from the model compared with data published by Harrison et al [45].

Initially, a mesh was prepared using a smoothed marching-cubes technique, but this resulted in either jagged surfaces or ill-shaped elements [131]. Four hexahedral meshes were generated using TrueGrid software (XYZ Scientific, Livermore, CA) at parametrically-controlled varying resolutions using the .stl surface data. The mesh topology was designed to allow for optimal representation of the mesh-sensitive soft tissues. The thickness of the cortical shell elements in the anterior body was examined to ensure that the mesh was sufficiently fine to represent this geometry [96]. By virtue of the modeling technique used for the trabecular bone, it was necessary that the cortical shell thickness was less than or equal to the physiologic value, which was an applied constraint.

Articular Cartilage

Articular cartilage was modeled as a single-element thick layer of cartilage extruded from the qCT-based osteochondral surface for the purpose of model convergence. All subsequent models utilize a three-element thick extruded cartilage model, with the superficial, middle, and deep layers accounting for 15%, 50%, and 35% of the total thickness, respectively. Accurate representation of the shape of the osteochondral interfacial surface and the superficial articular surface is particularly important for accurate prediction of contact pressures; however, Onan et al showed that qCT-based osteochondral surface definitions and mechanically digitized osteochondral and articular surface definitions were in good agreement, validating the use of qCT-based osteochondral surfaces [86]. Custom-written software was used to control the spatially-varying thickness distribution of the articular cartilage. Published data on the maximum and mean thickness of the articular cartilage at each facet were used in addition to a nonlinear spatial distribution algorithm to define the cartilage thickness for the base model [136, 141]. A local cylindrical coordinate system was generated central to each facet, and the nodes on the facet perimeter were used to assign relative radius values (0 at the center, 1 at the perimeter) to each node. The cartilage thickness at each node was assigned as a nonlinear function of the transformed radius [136]. Offset orientation of each superficial node relative to the osteochondral node was controlled as a linear combination of a locally perpendicular unit vector and the facet-specific cylindrical z-axis, with modest radially-varying central biasing. (See Appendix)

Intervertebral Disc

During voxel segmentation, disc space voxels were selected spanning adjacent vertebrae. The nuclear volume of each disc was identified by modeling a barrel-shaped volumetric mask. The masked volume was oriented parallel to the lengthwise axis of each specific disc, and the nucleus was prescribed as 15-20% of the cross-sectional area (Figure 11) [76, 101].

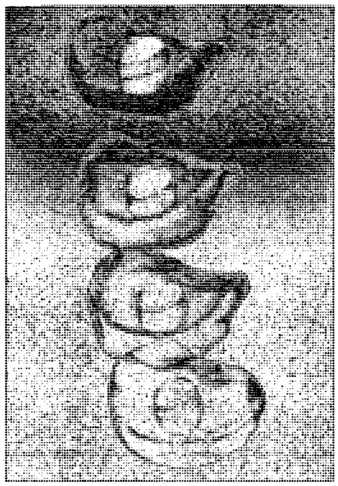

Figure 11 – Geometry used for intervertebral disc and nuclear volume definitions.

Annular fibers were created at two different resolutions using custom-written software. Multiple circumferential curves were created and evenly distributed throughout the annulus, and the curves were used as constraints for the nodal positions of the annular fibers (Figure 12).

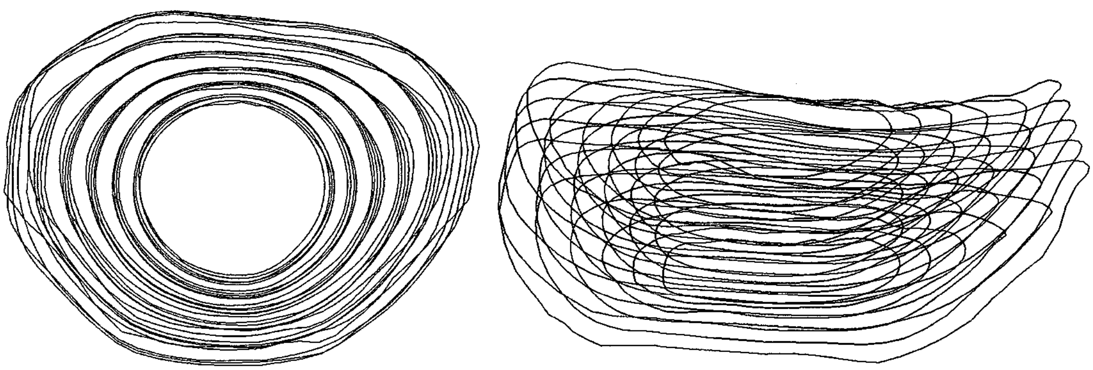

Figure 12- Base curves for the definition of the C5/C6 annular fibers at low resolution; 6 pairs of lamellar families with 4 sets of fibers each.

Multiple (6-9) pairs of fiber families were constructed such that the mean interlamellar fiber angle for each pair of fiber families was controlled, varying from 60 deg at the periphery to 90 deg at the nuclear margin [55, 57]. Six pairs of fiber families were used for the extra-low- and low-resolution models during the convergence study, and nine pairs of fiber families were used for the higher-resolution convergence models and all subsequent models (Figure 13).

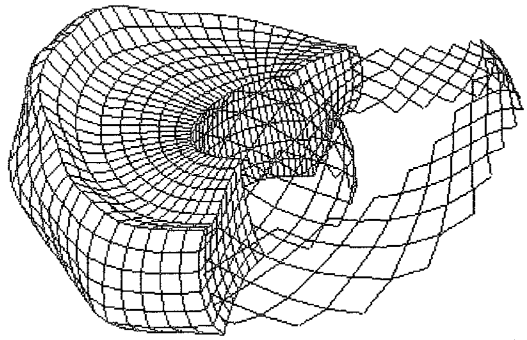

Figure 13– Two pairs of fiber families shown for the C5/C6 annulus at higher resolution. Fiber angles are maintained as disc height varies. Variation of fiber angle with radius is apparent.

Interlamellar fiber angle was controlled by optimization of the fiber node positions along the constraint curves. Using this technique, it was possible to maintain control of the fiber angles throughout the disc. The fibers were represented as nonlinear spring elements, and the mechanical properties of each spring element were controlled by binning the fibers into 64 sets by length and effective cross-sectional area, which is the area of the disc for which reinforcement is represented by each fiber. In this manner the spatially varying fiber size and density were accommodated.

Ligaments

Ligaments were modeled as parametric nonlinear spring elements. Multiple springs (6-11) were used to represent each ligament, excluding the capsular ligaments. The mechanical response of each spring was scaled according to the number of elements used to represent each ligament. A custom-written program was used In order to ensure inter-model correlation of ligament positions. After all ligaments had been defined for the first mesh, nodal positions in the subsequent meshes were queried and each ligament attachment node in the original mesh was substituted with the nearest node in the target mesh.

Mesh Quality Optimization

Finite element solution quality and convergence rates are highly sensitive to mesh quality, especially when large deformations and nonlinear material and geometric responses are involved. Several measures of mesh quality have been proposed by various researchers, but no universally optimal measure is generally accepted. Simple Laplace optimization can move interior nodes to the mean or mode positions of the neighboring nodes, but this can result in skewness and element inversion for some mesh topologies. Minimally, a hexahedral element must have a positive Jacobian, which is essentially a volumetrically-invariant measure of the element shape that will become negative if the element is inverted [149]. Additionally, it is frequently beneficial to maintain element aspect ratios close to unity. A custom-written program was created to optimize mesh quality while maintaining external and interfacial geometry. A node-based scalar measure of mesh quality was developed that consists of a linear combination of the scaled Jacobians and aspect ratios of all elements associated with the node, unity being optimal. The gradient of mesh quality with nodal position is calculated for each node, and a sloppy line search ($N_{max}=5$) is employed with search radius equal to a fraction of the distance to the nearest neighboring node. Each interior non-interfacial node is moved to the optimal position observed in the line search. This operation is performed simultaneously and independently to all nodes, and is performed iteratively until mean and minimum mesh quality targets have been achieved or mesh quality has been optimized for the given topology (Figure 14).

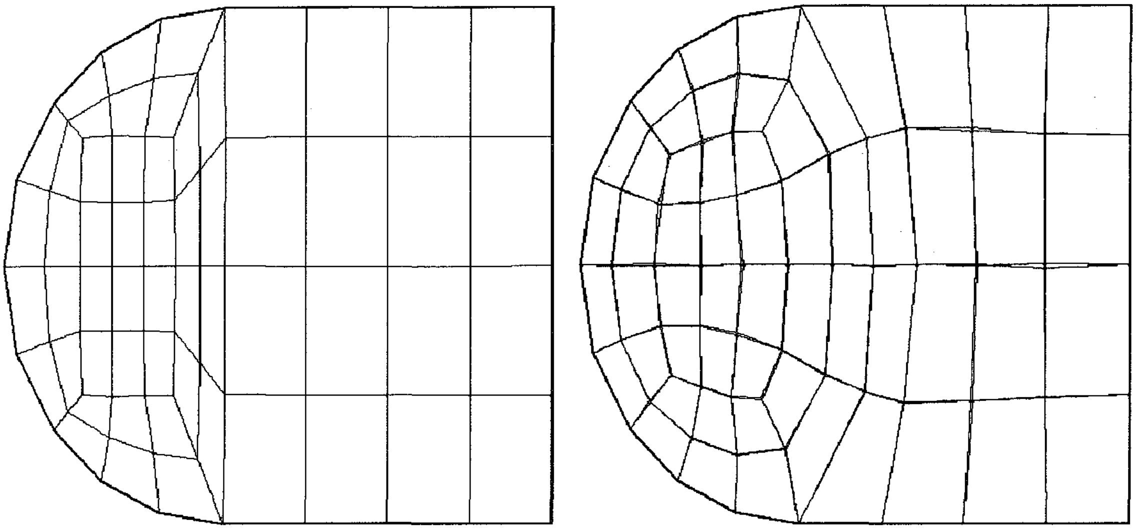

	Before optimization	After optimization
Minimum Jacobian	0.41	0.65
Average Jacobian	0.93	0.97
Maximum Aspect Ratio	4.50	3.38
Average Aspect Ratio	2.07	1.84

Figure 14 – Sample mesh before (left) and after (right) optimization. Element shapes improve and geometry is maintained.

Transverse Foramina

During the course of model generation, three accessory foramina were observed: one at C5 and two at C6. Jaffar et al examined the occurrence rate of accessory foramina in the cervical spine, and found that accessory foramina were most common at the C5 and C6 levels, with incidence rates of 50% and 70%, respectively [59]. Additionally, the cross-sectional areas of the primary transverse foramina as modeled compared favorably to those measured by Jaffar et al, measuring form 25 to 34 mm^2 (Figure 15) [59].

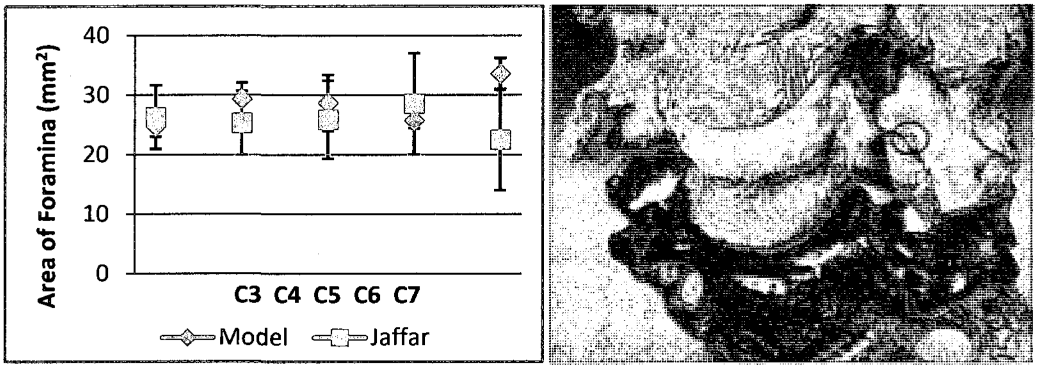

Figure 15 - Published and modeled foramina areas (left), and accessory foramina (right) [59].

Endplate Thickness

Resection of the cartilaginous endplates has been shown to reduce the compressive strength of vertebrae, as well as increasing the tendency toward subsidence of fusion cages [100]. For this reason, it is anticipated that accurate representation of endplate thickness is important for finite element models involving arthroplasty and/or arthrodesis. To this end, the thickness of the cartilaginous endplates of the anterior column was adjusted in accordance with the observations of Schmitz and Pitzen (Figure 16)[100, 117].

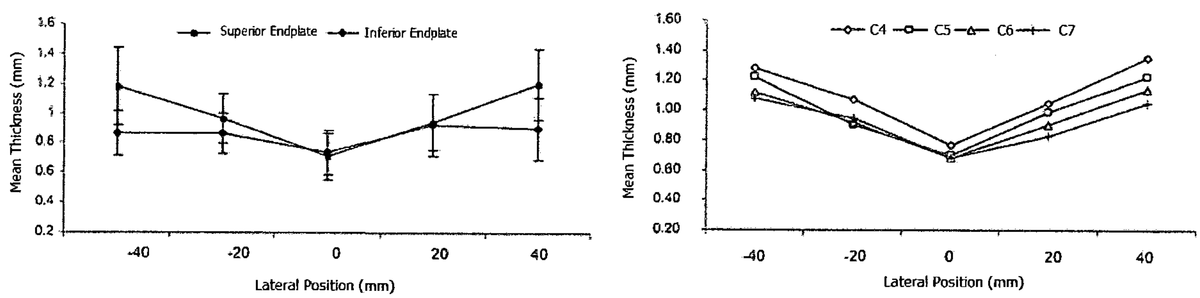

Figure 16– Endplate thickness variation through a coronal slice, adapted from Pitzen [100].

They observed regional variation in endplate thickness after accounting for local perforations, with generally thicker endplate along the perimeter [117]. The endplate thickness of the model was specified numerically at the perimeter and adjacent to the nucleus, and varied between the regions (Figure 16). Additionally, differences between vertebral levels and between the inferior and superior endplates were accounted for [96, 100].

Material Properties

Cortical and Trabecular Bone

A linear relationship between CT density and axial modulus in the lumbar anterior body was observed by Rho et al (Equation 1) [107].

$$E_3(MPa) = 6.68 * CT\# - 94$$

Equation 1 – Trabecular modulus vs. CT density, from Rho [108]

Because the primary load orientation in the anterior body is axial and any anisotropic trabecular orientation in the posterior elements, if it exists, is unknown, both the cortical and trabecular bone were modeled as linearly elastic and isotropic for the purpose of model convergence. Subsequent models utilized a transversely-isotropic linearly elastic representation of trabecular bone with a Poisson ratio (ν) of 0.3, as follows (Equation 2)[108].

$$\begin{gathered} E_1 = E_2 = 0.345 * E_3 \\ G_{13} = G_{23} = E_3 \div 2.6 \\ G_{12} = E_1 \div 2.6 \end{gathered}$$

Equation 2 – Orthotropic trabecular moduli.

Cortical bone was parameterized with an elastic modulus of 11,000 MPa and a Poisson ratio (ν) of 0.3. Relevant spatial variation in trabecular bone density and modulus was accommodated by binning the trabecular bone elements into nine different groups with different moduli (Equation 1) and the Poisson ratio was held constant at 0.3. This operation was performed by registering the finite element model to the original CT dataset using a custom-written program

(Visual Basic 6.0, Microsoft Corporation, Redmond, WA). For each trabecular element, 125 points interpolated throughout the volume of the element (5x5x5) were located, and the CT density for the correspondent voxel containing each point was queried. Volumetrically-weighted averaging was performed and a single density value was assigned to each element. Histographic analysis of the density distribution was performed and the elements were binned into ten sets containing approximately equal numbers of elements (Figure 17).

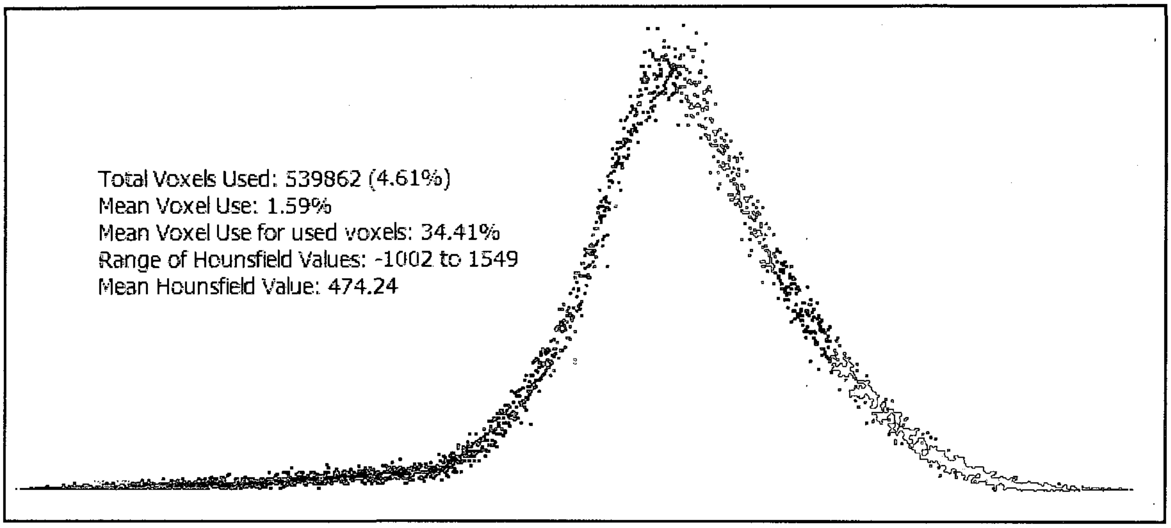

Figure 17 - Histographic analysis of CT-based density (Hounsfield #) for a representative model.

The minimum, maximum, and mean Hounsfield values for the elements in each set were recorded, and the mean Hounsfield value was used to assign the modulus for each set.

Internal validative checks on this method were performed by additionally analyzing the cortical and disc annulus elements, comparing results for the different mesh resolutions, and by graphically identifying the voxels used in Hounsfield analysis (Figure 18). Mean trabecular HU values for the different meshes were comparable, and the mean HU values for all materials were within the anticipated ranges.

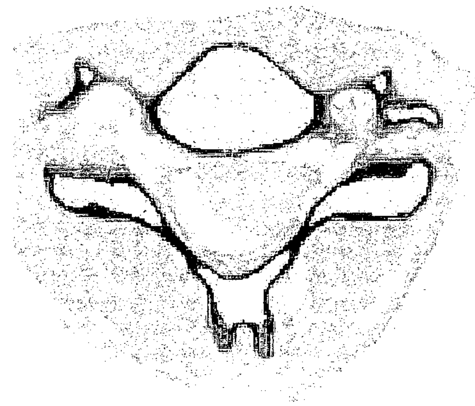

Figure 18 - Reverse-color image showing overlay of referenced trabecular voxels on qCT imagery

Even though a single-element cortical thickness was used throughout the model, the parameterized modulus of the densest trabecular bone approached that of the cortical bone (Figure 19)[108].

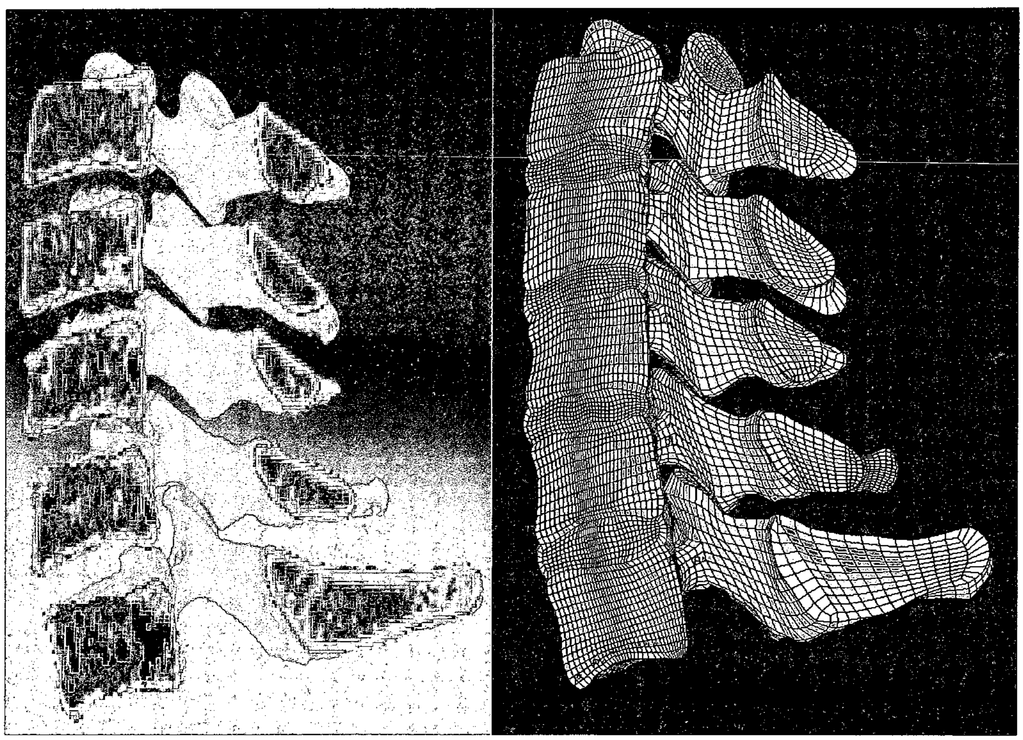

Figure 19 - Lateral qCT cross-section (left), and model cross-section with elements colored by modulus (right), showing correlation between raw imagery and mechanical property distribution.

The endplates were parameterized with modulus 1000 MPa and Poisson ratio of 0.3 [10, 143].

Articular Cartilage

Articular cartilage was modeled as a second-order reduced polynomial hyperelastic material with initial Poisson ratio ν=0.4 and a bulk initial modulus of 1.8 MPa. The hyperelastic coefficients were fitted to nonlinear confined compression data [64]. This approach was used to simulate the short-term response of the cartilage [3]. A lower Poisson ratio could be used to simulate long-term behavior using this single-phase approach. Due to the short time scales involved in loading of the articular facets, a single-phase representation was deemed appropriate. The middle zone cartilage layer was assigned the material properties of full-thickness cartilage, whereas the superficial and deep zones were defined as having half and twice the bulk stiffness, respectively, with initial moduli of 0.9 and 3.5 MPa [114].

Intervertebral Disc

The nucleus pulposus was parameterized as a nearly incompressible linearly elastic material with modulus 1.5 MPa and Poisson ratio of 0.499 [29, 84]. A structural elastic approach was used to model the annulus fibrosus, with nonlinear spring elements embedded in an isotropic hyperelastic matrix [26, 29, 125]. It is assumed that any material anisotropy is due to the presence and orientation of the fibers [66]. The annulus ground substance was modeled as a second-order reduced polynomial hyperelastic material with Poisson ratio of 0.45 (D1=2.495, C10=4.146E-2, C20=7.267E-2) [41, 130]. Fibers were modeled as nonlinear spring elements. The prestress in the disc was modeled by applying an isotropic thermal strain of 10% to the nucleus, and 5% in the annulus. This approach induced tension in the fibers and compressive pressure in the nucleus and matrix [63]. The nonlinear definition of the spring elements was optimized for representation of the circumferential response of the annular laminae [130].

Ligaments

The nonlinear behavior of the ligaments was based on bone-ligament-bone force-extension data published by Yoganandan et al [142]. This approach was considered to be the most reliable, as few assumptions need to be made regarding ligament geometry (Figure 20).

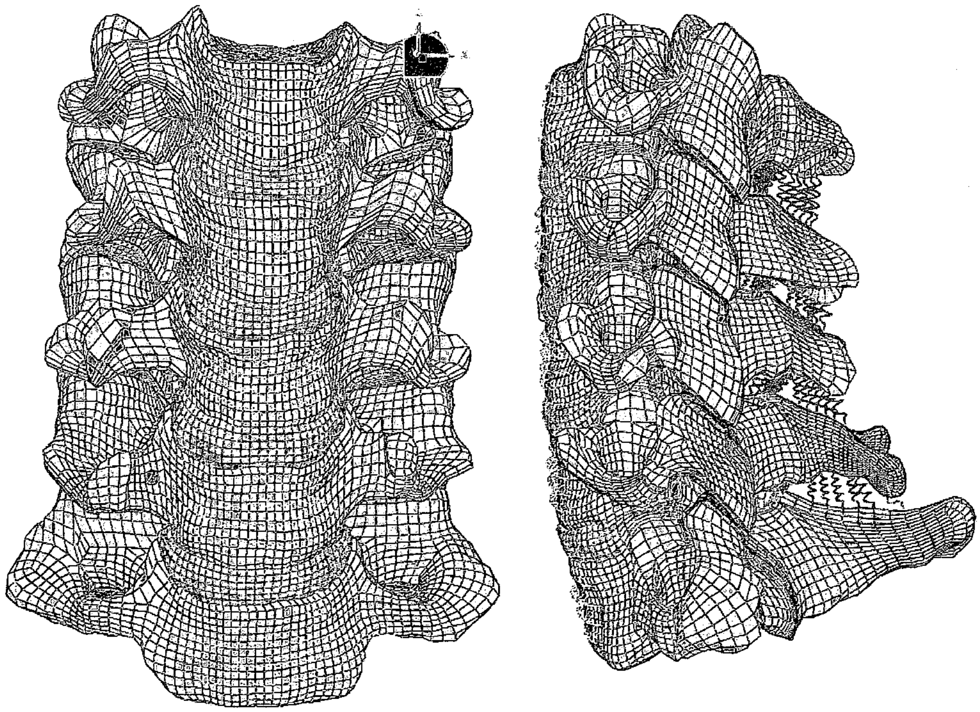

Figure 20 - High resolution model, with ligaments highlighted on the right

The toe region and pretension were defined parametrically, with 1-10 N of preload per ligament, and bilinear toe regions of 0.5 to 1.5 mm [82, 142]. The exact pretension values are unknown. Pretension was estimated by performing an analysis step in which ligament pretensions and thermal strains in the disc were allowed to equilibrate as facet contact was established. Ligament pretensions were iteratively adjusted so that the resting (equilibrium) position was approximately the same as the initial position, indicating an appropriate balance.

3 Model Convergence

Four models were developed in order to verify model convergence. The model topology, which was consistent between models, was optimized for control of soft tissue mesh quality. The models ranged from 59,000 to 144,000 elements corresponding to 69,000 to 159,000 nodes (Table 1).

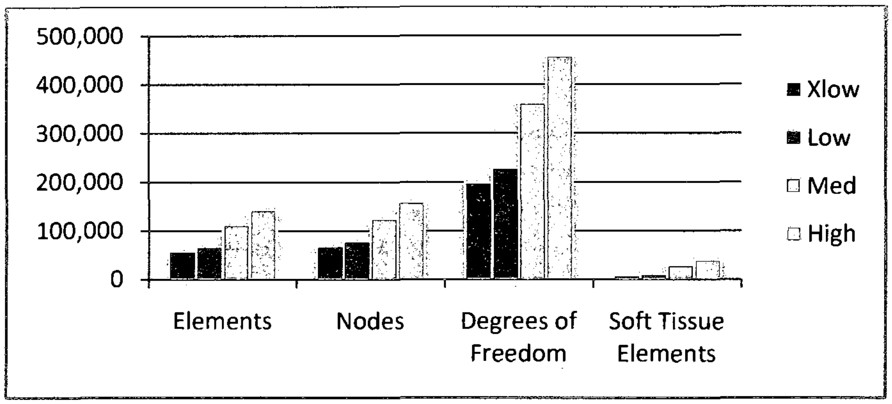

Table 1 - Convergence model parameters. Model topology was designed for maximum variation in soft tissue mesh resolution. Soft tissue elements increased 375% from the lowest to highest mesh resolutions.

Model convergence was examined for all load cases throughout the load range. The average principal stresses and strains in the C6/C7 annulus, principal strains on the posterior laminae in the region of strain rosette placement, mean nuclear pressures, disc bulge, facet contact pressures and forces, strain energy and total range of motion were examined. Summary data are averaged over all load cases and over the full load ranges, excluding disc bulge and range of motion data, which are total range values (Table 2)

In Figures 21-27, values for all four models are presented with varying line thickness with dotted, dashed, long-dashed, and solid lines for the lowest through highest resolution meshes, respectively.

Mesh	C6/C7 Annulus Stress/Strain			Facet contact forces				Cortical Strain on Pedicles C4-C6		Δ Nuclear Pressure		Disc Bulge	Range of Motion		
	Max. Principal Stress	Min. Principal Stress	Max. Principal Strain	C4/C5 Left	C4/C5 Right	C5/C6 Left	C5/C6 Right	Max. Principal Strain	Min. Principal Strain	C4/C5 Nucleus	All Nuclei	C6/C7 (Flexion)	Flexion Extension	Lateral Bending	Axial Torsion
Xlow	-6.0%	-7.4%	6.2%	-1.2%	10.0%	-0.9%	7.2%	-0.5%	2.8%	-3.2%	-1.9%	-1.5%	1.2%	13.5%	14.3%
Low	-6.1%	-5.5%	8.3%	-5.0%	-4.2%	-2.6%	-9.4%	-8.7%	-5.5%	1.3%	2.3%	-1.2%	2.0%	4.6%	4.0%
Medium	6.9%	-5.2%	-6.5%	-1.5%	-1.7%	-3.7%	-2.6%	-2.3%	-1.8%	-0.1%	0.3%	-2.6%	0.8%	2.1%	0.8%

Table 2 - Model convergence summary. Differences between selected models and highest resolution model for selected values. Average differences over all load cases and load ranges are given, excluding disc bulge and range of motion, which are differences between total range values. Values exceeding 5% and 10% are highlighted.

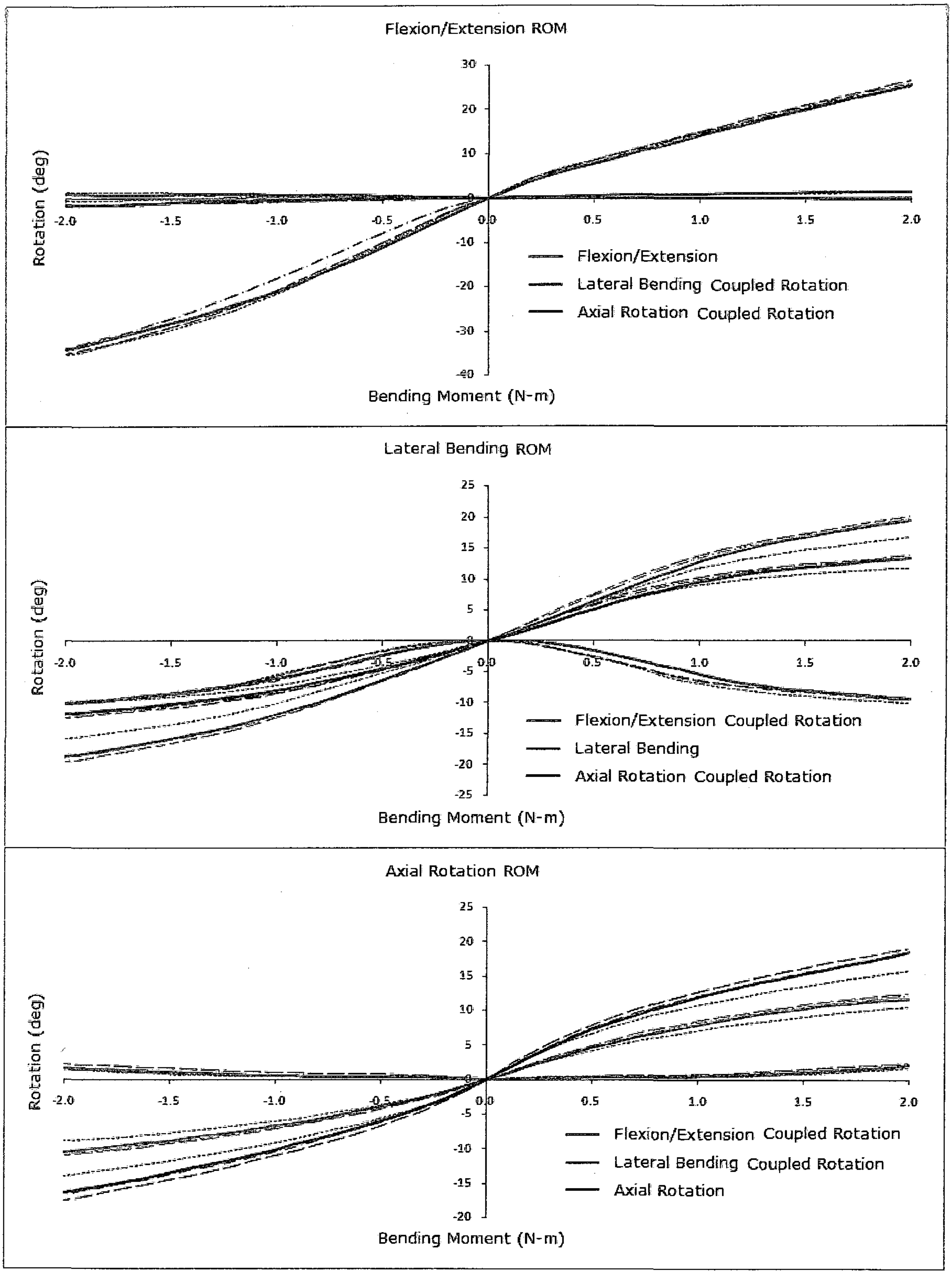

Figure 21 – Convergence - Range of Motion for the C3-C7 segment

Mesh resolutions: High, Middle, Low, Extra Low

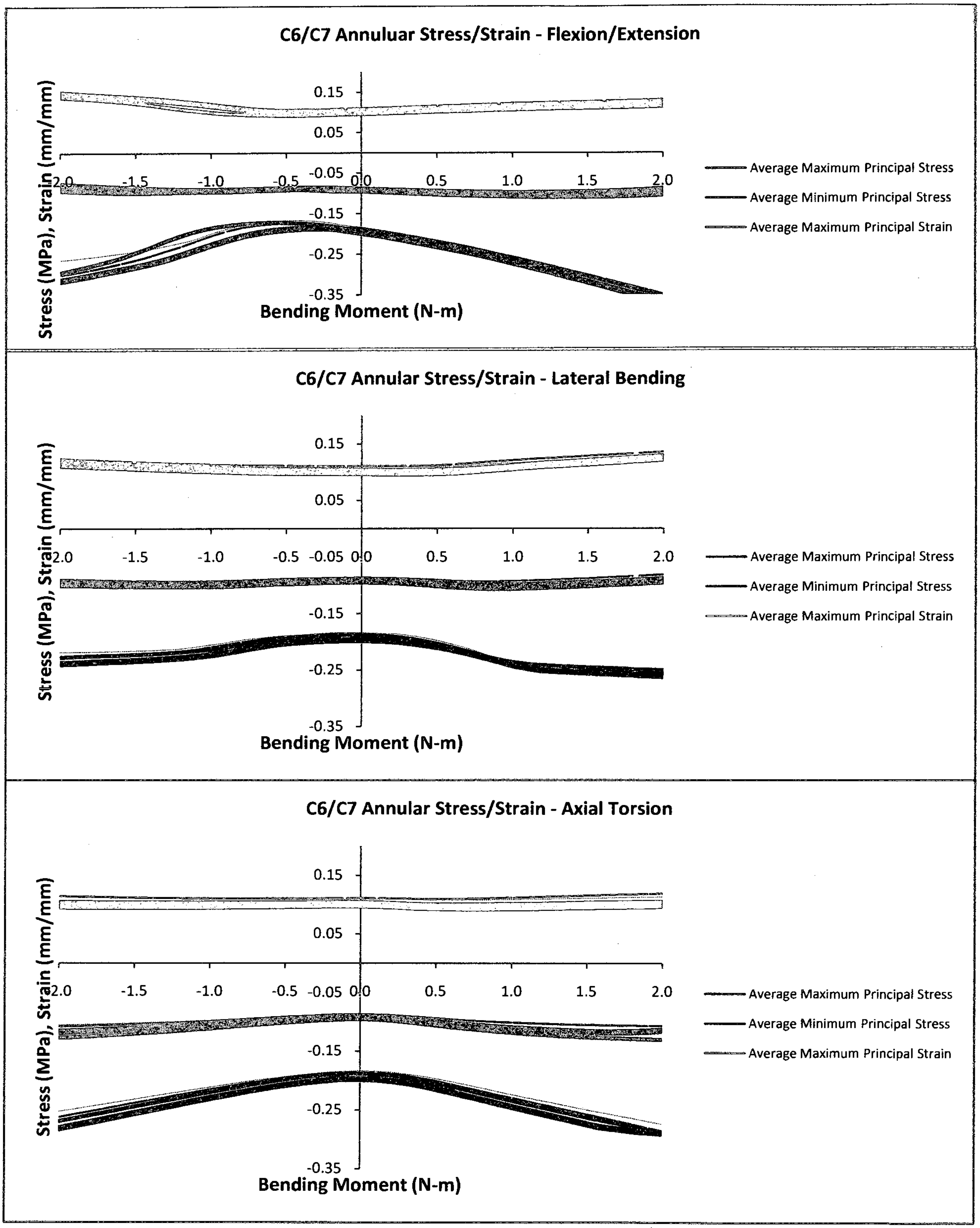

Figure 22 - Convergence - Principal stresses and strains averaged over the C6/C7 annulus

Mesh resolutions: High Middle Low Extra Low

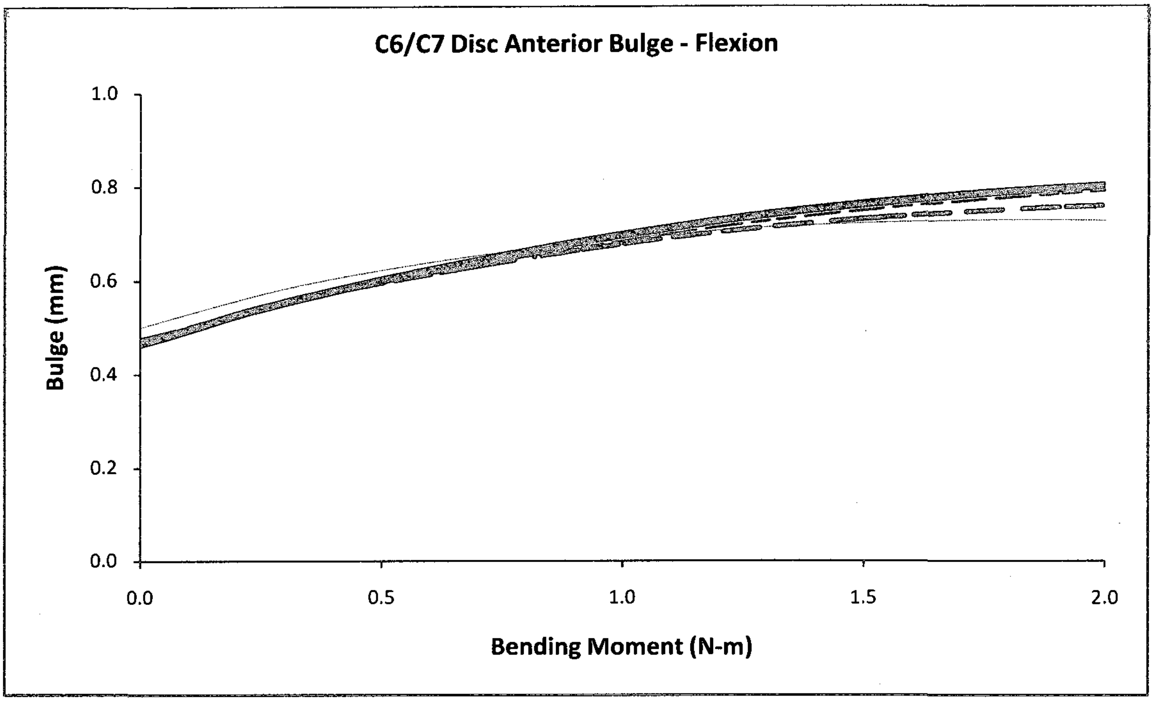

Figure 23 - Convergence - Anterior bulge of the C6/C7 Annulus during forward flexion.

Mesh resolutions: High Middle Low Extra Low

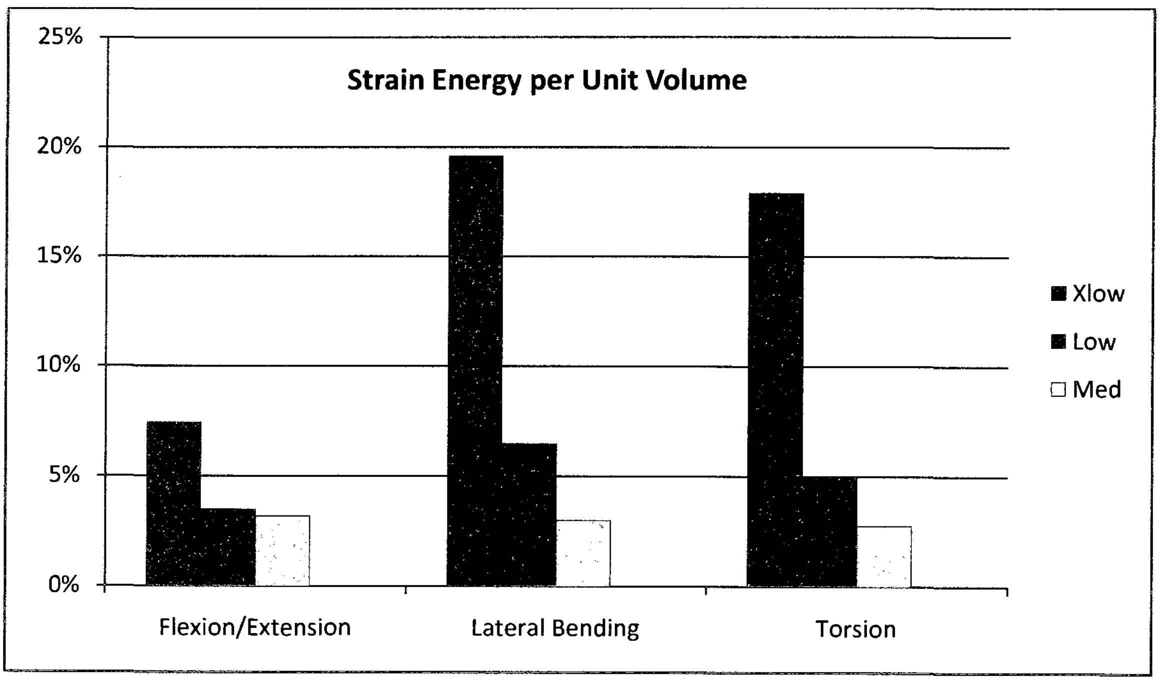

Figure 24 - Convergence - Strain Energy per unit volume at ± 2 N-m, expressed as the percentage difference from the values for the high resolution model.

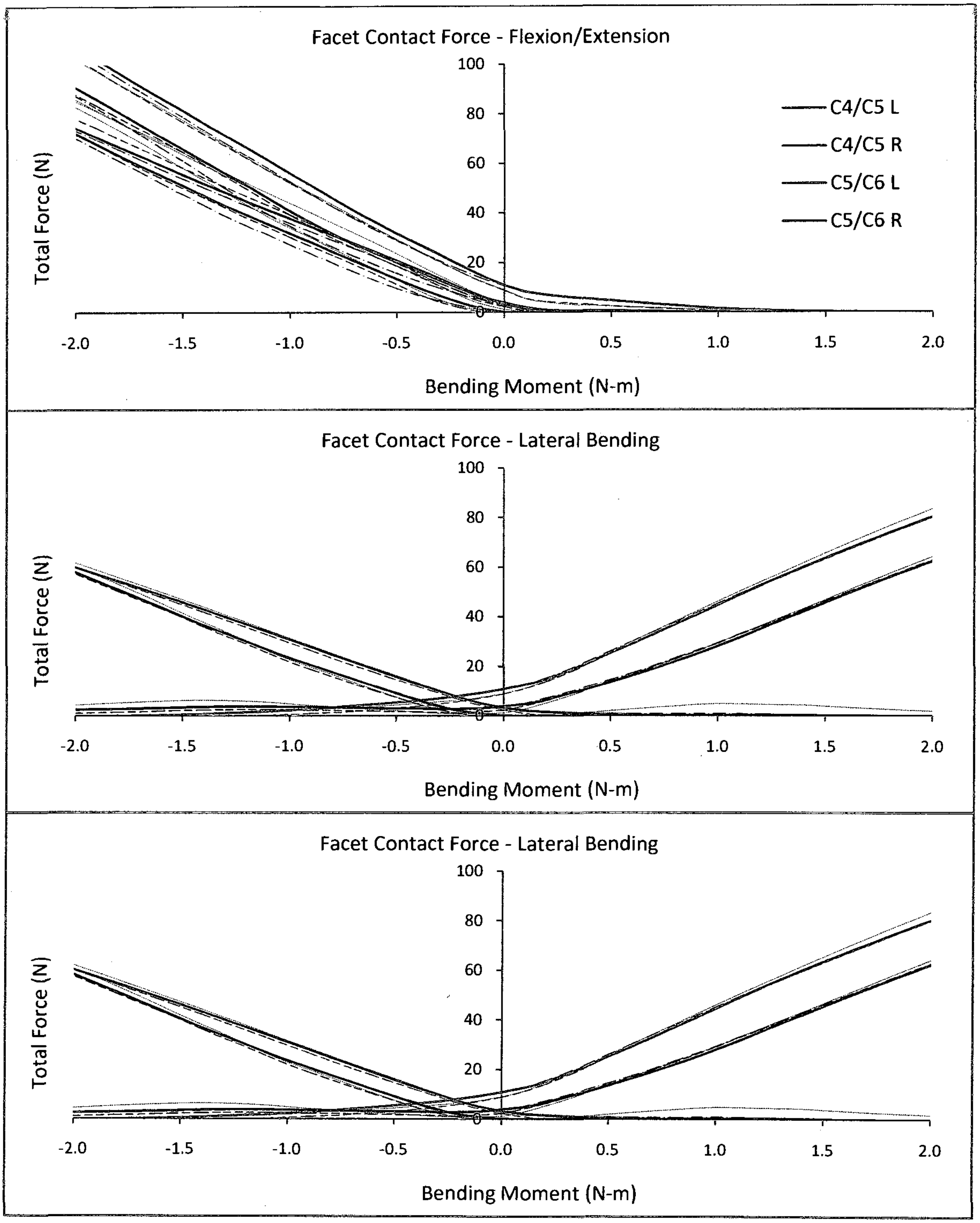

Figure 25 - Convergence - Total facet joint contact forces for the C4/C5 and C5/C6 articulations

Mesh resolutions: High Middle Low Extra Low

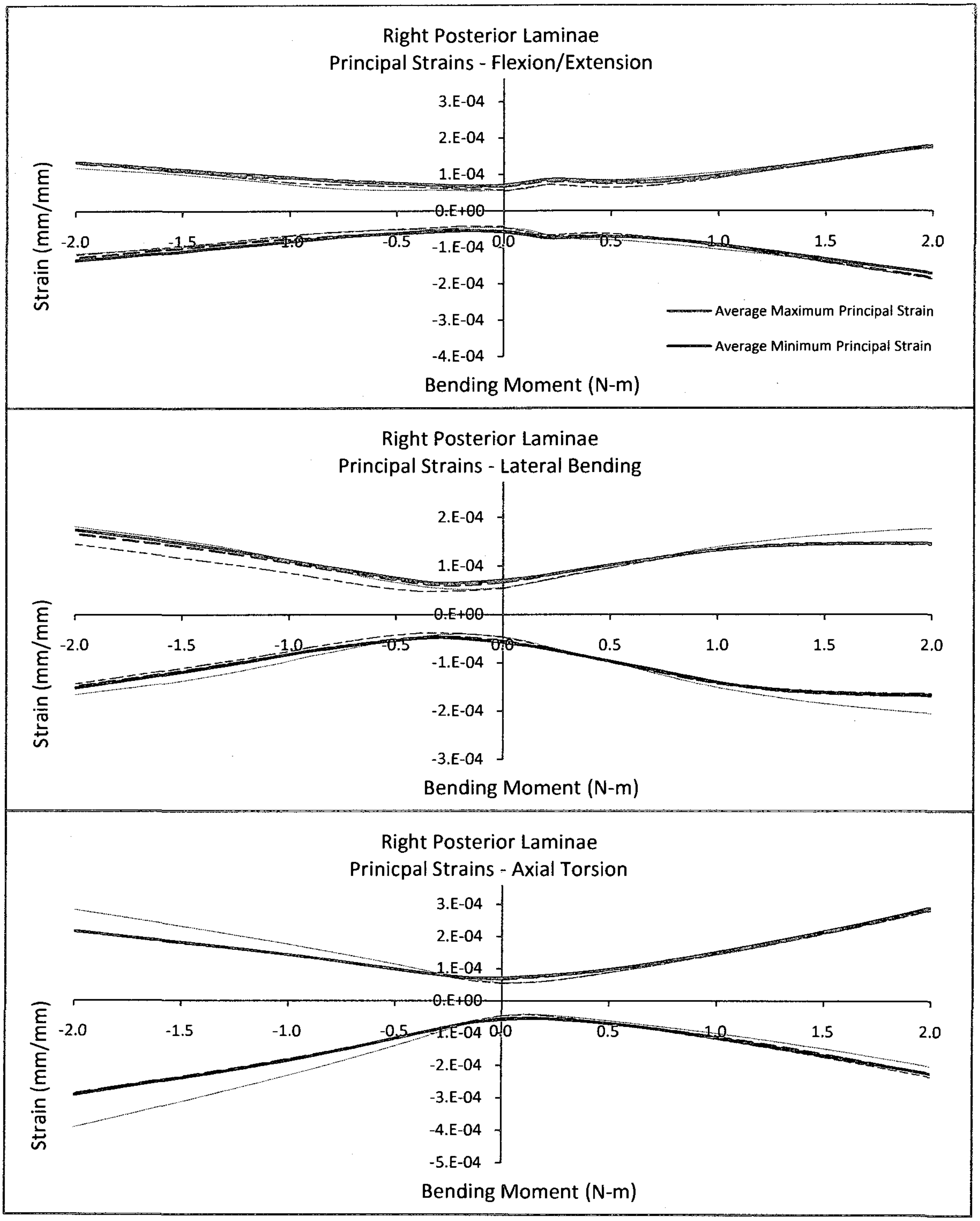

Figure 26 - Convergence - Principal strains on the right posterior laminae of C4-C6 in the regions of gage placement

Mesh resolutions: High Middle Low Extra Low

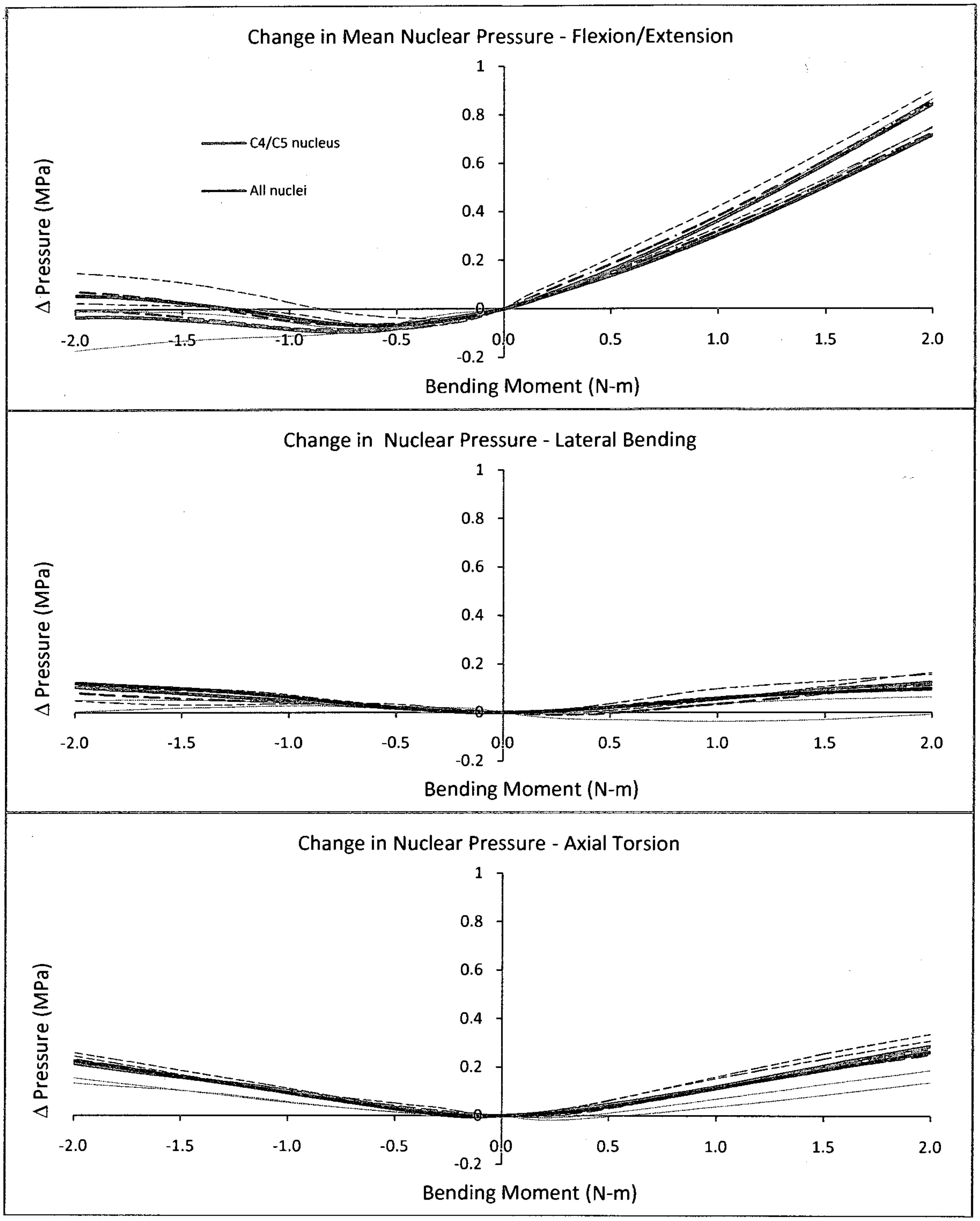

Figure 27 - Convergence - Change in mean nuclear pressures with loading

Mesh resolutions: High Middle Low Extra Low

Convergence thresholds of 5% and 10% were investigated, and convergence within 6.9% (of highest-resolution mesh values) was obtained for all parameters for the medium resolution mesh (Table 2)

Facet contact forces were observed to be less sensitive to mesh resolution than contact areas and contact pressures. Contact area is strongly dependant on the congruence of the contact pairs, which is a function of the mesh resolution. Contact forces, however, are less sensitive to the articular geometry (Figure 28).

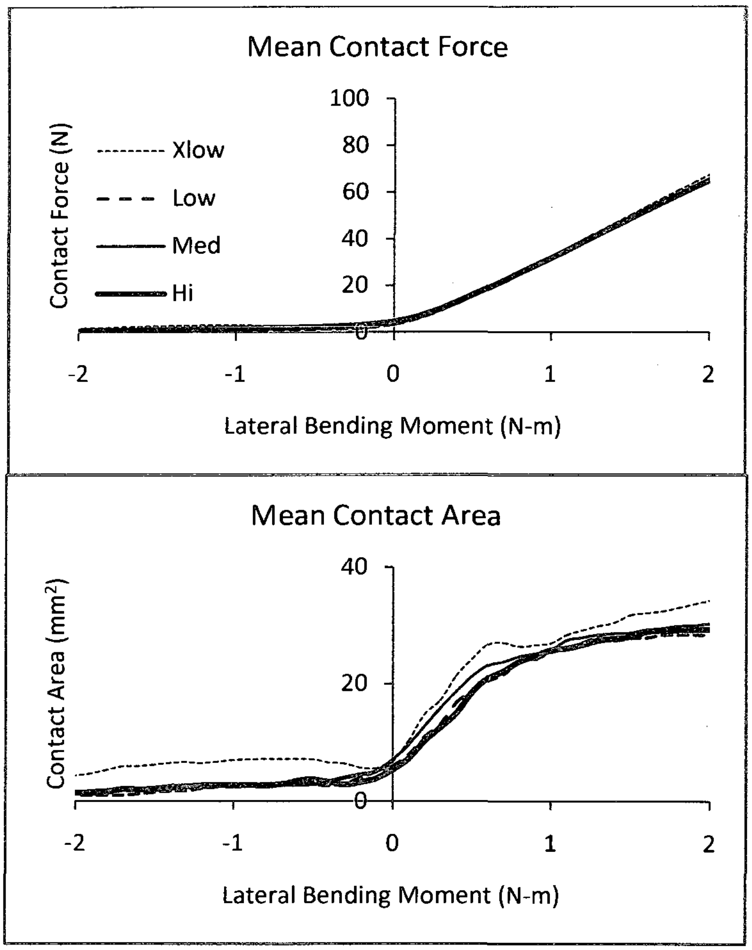

Figure 28 - Facet contact forces and areas under lateral bending, averaged over all contact pairs. Contact area exhibits higher sensitivity than contact force to mesh resolution.

Inter-model variation in mean nuclear pressure remained within 10% of the range of pressure throughout the nuclear volume for all models over all load cases (Figure 27). Anterior bulge of the C6/C7 disc was calculated as the difference between the maximum anterior displacement of the nodes on the central anterior surface of the annulus and half the maximum anterior displacement of the nodes on the central anterior surface of the inferior endplate of C6 during flexion, C7 remaining essentially stationary. Inter-model variation in C6/C7 disc bulge remained within 10% of the full scale value for all models over the flexion range of motion (Figure 23).

Inter-model variability in the principal strains on the right posterior laminae was within 2% on average and 15% in the worst case of the range of maximum and minimum principal strains, respectively, in the sampled regions (Figure 26). This indicates that the strain gradient in the sampled region is nontrivial, an observation that was borne out during experimental validation.

Inter-model variation in average annular principal stresses and strains remained within 4% of the respective ranges in the worst case, and within 7% of the full-scale value on average (Figure 22). Spatial variation in the annular principal stresses and strains was substantial, with the range of each quantity being of the same order as the peak value.

Total ranges of motion for the low and middle resolution models were within 5% of the highest resolution model in the worst case, while the lowest resolution mesh was overly stiff, with peak ROM differences of approximately 15% in lateral bending and torsion (Figure 21).

Whole-model strain energy per unit volume was examined over the complete range of motion, and it was observed that most of the difference in this measure between the models was introduced during the initialization step. Relative differences in specific strain energy under load are presented in Figure 24.

Based on the convergence data obtained, the third (middle) resolution mesh was considered sufficiently converged for the parameters investigated. All cartilage-thickness variational models and implant models were based on this mesh. The mesh resolution of all implants as modeled exceeded the mesh resolution of the C4/C5 intervertebral disc of the highest-resolution mesh.

4 Model Validation

The finite element models were validated both internally and externally as described below [129]. Geometric checks were performed by overlaying various parts of model data, by visual comparison, as well as by numerical comparison with published geometric parameters. Experimental cadaveric data were collected as well.

Validation of Annulus Properties

The material model used for the annulus fibrosus was created using a process of calibration and internal validation. A hyperelastic annulus ground substance and discrete fiber reinforcement using nonlinear spring elements were used. The annulus was modeled after the experimental multidirectional tension and confined/unconfined compression data presented by Wagner et al [130]. The hyperelastic coefficients of the annulus ground substance were fitted to the radial tension data, under the assumption that fiber reinforcement plays little role under radial tensile strain. The Poisson ratio was determined based on the radial confined compression data. A finite element model was then developed with 27 linear brick elements embedded with 600 nonlinear spring elements, having 1410 total degrees of freedom (Figure 29).

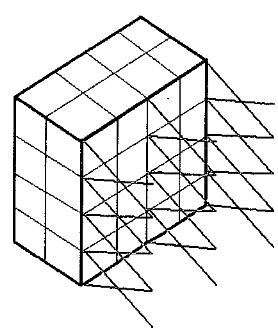

Figure 29 - Schematic of model used for validation of the material properties of the annulus. Cutaway with some fibers hidden.

The fibers were arranged in 6 pairs of lamellar families with an interlamellar angle of 60 deg. The boundary conditions of the model in each load case were modeled after the experimental protocols presented by Wagner et al [130]. A 10% circumferential tensile strain was applied, and the displacement and reaction force profiles during loading were recorded and converted to overall (bulk level) stress/strain values. The tabular data defining the nonlinear response of the spring elements were iteratively modified to fit the circumferential tensile response. Internal validation was performed by examining the model under circumferential compression and axial tension and compression, which were not used to define the material properties. The model response under all load cases was within 0.4 standard deviations of the experimental means (Figure 30).

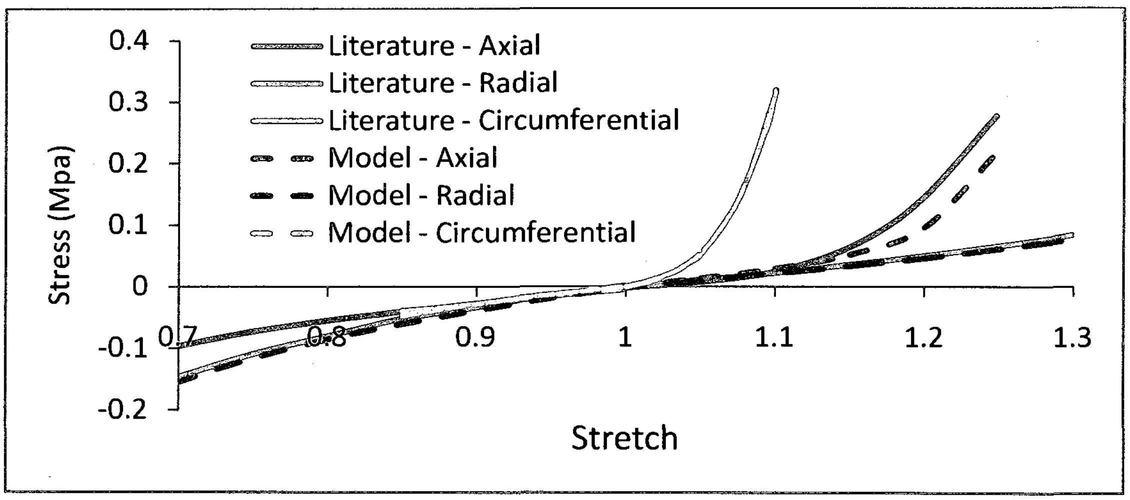

Figure 30 – Comparison of annulus fibrosus models with experimental results [130].

Fiber representation using linearly elastic and hyperelastic (Neo-Hookean, Mooney-Rivlin formulations) models was examined, but acceptable performance was not achieved by these methods.

Cadaver Experiments

Six fresh-frozen human cadaveric cervical spines were obtained, and the C3-C7 segments were isolated. Muscle and extraneous tissues were removed, with care taken to preserve the ligamentous structures. The anterior aspect of C3 and the posterior aspect of C7 were potted for mechanical testing. Strain rosettes were attached on the right posterior laminae of C4-C6, as this region was accessible and otherwise unencumbered (Vishay Intertechnology Inc., Malvern, PA). A small pressure transducer was implanted in the C4/C5 nucleus after penetration with a K-wire (Model 060S, Precision Measurement Company, Ann Arbor, MI). Triad markers for motion capture were attached using modified K-wires at all levels, and motion data were collected at 10 Hz (Motion Analysis Corporation, Santa Rosa, CA). A 40 N follower load was selectively applied using a weight and pulley system with positional control at C3, C5, and C7. Pure moments up to 2 N-m were applied quasi-statically in all six principal directions using a custom-built spine testing apparatus (Figure 31). Tekscan pressure sensors were used to measure contact pressures and forces in the C4/C5 and C5/C6 articulations (Model 6900 Tekscan Inc, South Boston, MA). A six degree-of-freedom load cell mounted caudally recorded reaction forces and moments at 50 Hz. Hydration was maintained using physiologic saline at fifteen minute intervals during cadaveric testing.

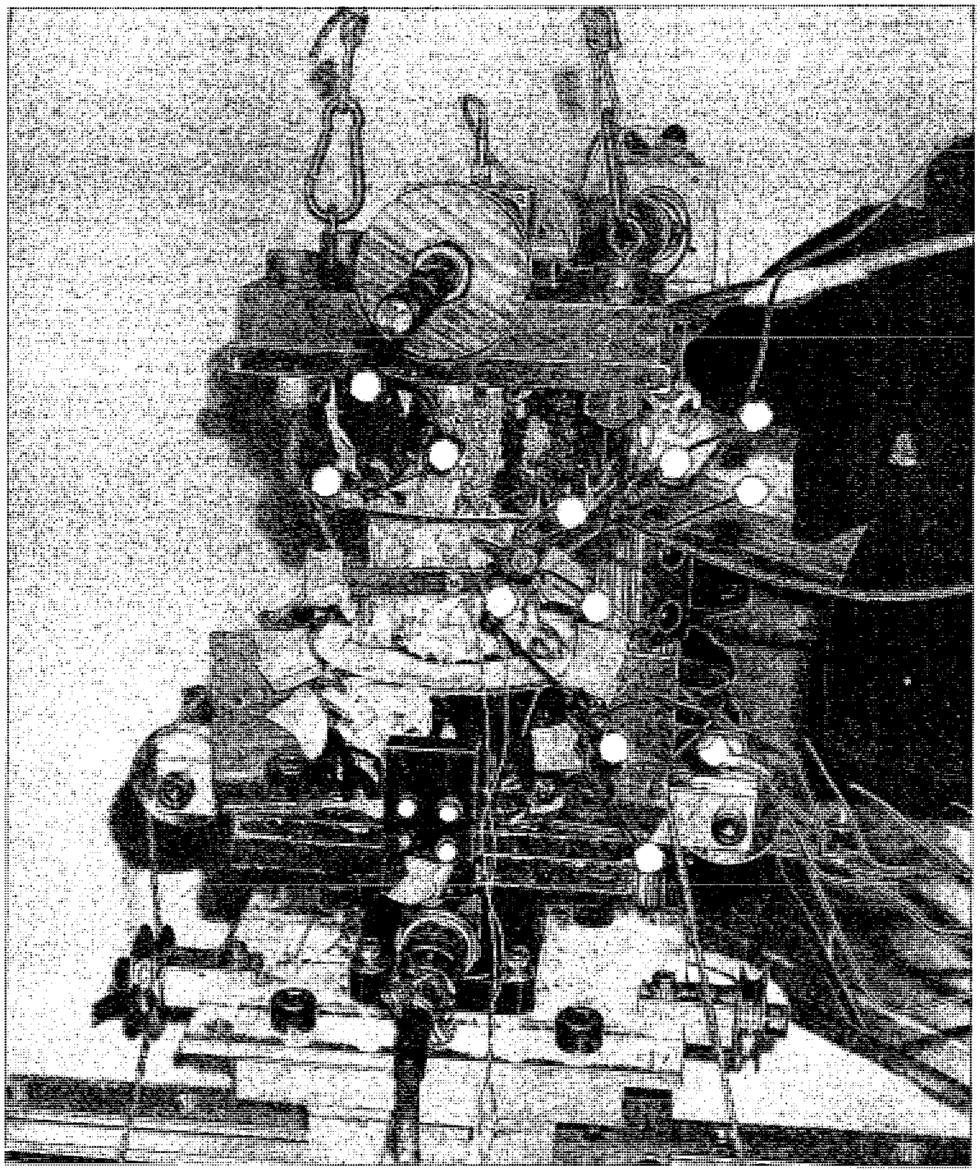

Figure 31 - Anterior view of experimental setup for lateral bending showing marker triad placement, counterweights attachment on superior pot, follower load system, and nuclear pressure transducer placement.

Tekscan sensors and pressure transducers were calibrated and equilibrated at 100 psi each day of testing using a custom-built pressure chamber. Strain gages were calibrated using a standard aluminum dog-bone specimen.

Specimens were cycled to ± 2 N-m 10 times before data collection, and data were collected on the subsequent 5 cycles. Tests were performed first without a follower load in each of the three load axes, and were then repeated with the added follower load. Data were collected during the application of then follower load as well, in order to determine the effect of the compressive load. After all 3 pairs of tests (flexion/extension, lateral bending, and axial torsion), the facet capsular ligaments at C4/C5 and C5/C6 were resected at the posterior and lateral aspects and the Tekscan sensors were inserted. All tests were then repeated with Tekscan sensors in place. In this manner the effect of facet capsule resection on overall kinematics could be investigated (Figure 32).

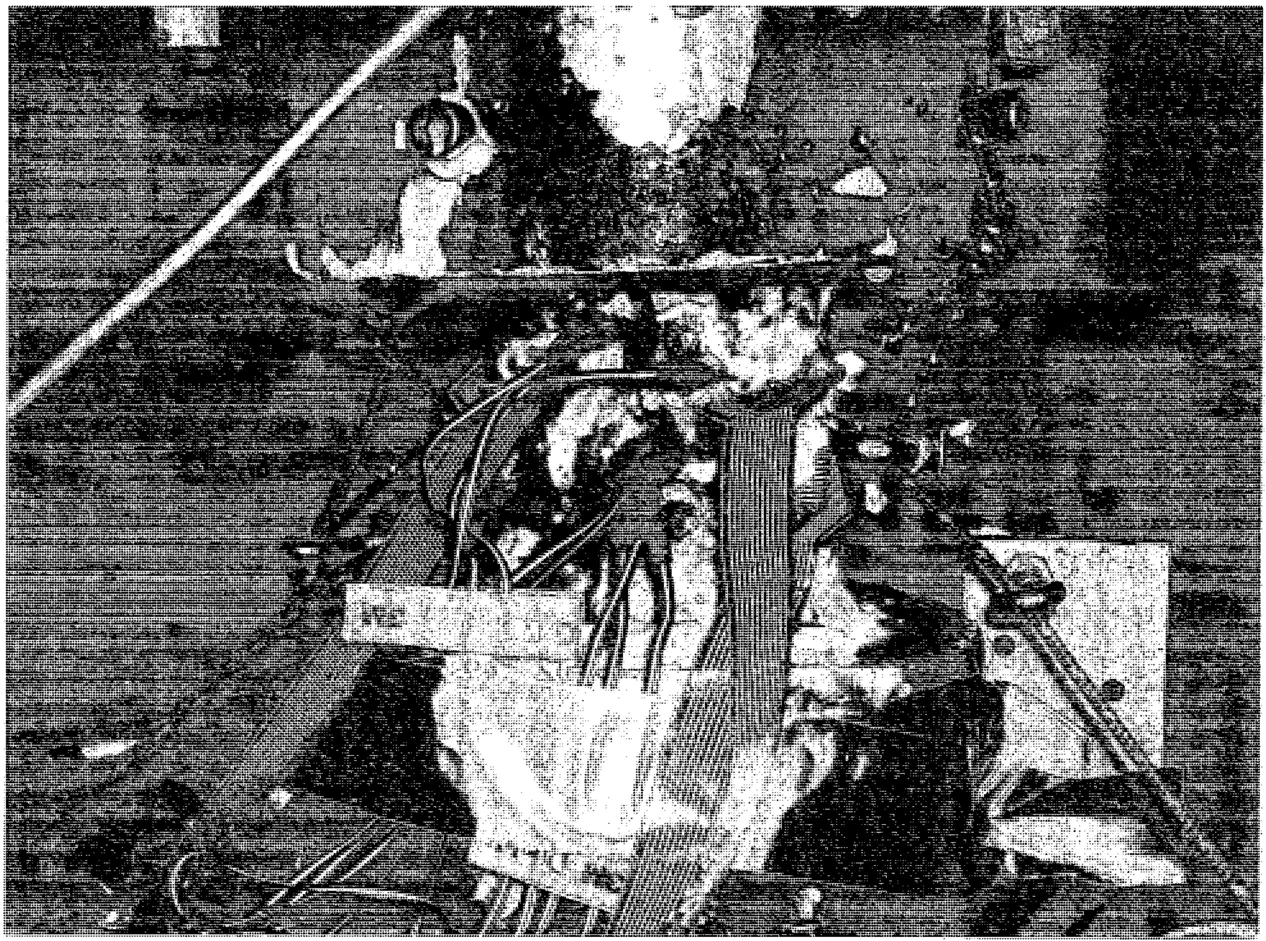

Figure 32 - Posterior view of experimental setup showing detail of Tekscan and strain gage rosette placement and follower load.

Validation Results

Validation of finite element models of the cervical spine is generally performed solely on the basis of total range of motion in the directions of the principal loads [10, 11, 38, 43, 89, 121]. Coupled ROM in secondary orientations and ROM at individual motion segments are occasionally investigated as well, and some researchers have performed more extensive validation [112]. Urbina has noted that validation can be defined as the process "of determining the degree to which a computer model is an accurate representation of the real world from the perspective of the intended model applications" [129]. With this in mind, it should be noted that a model cannot be said to be globally 'validated' in a broad sense; at best, the predictive accuracy of the model with respect to particular measures can be bounded with respect to an accepted value, e.g. "Total range of motion in the direction of loading is within 5% of experimental means for all load cases." Extrapolation of model validity to other measures must be explicitly justified. For example, if total range of motion in the principal direction is used to validate predictions of secondary coupled motions, further justification must be provided.

Table 3 presents total range of motion results for the model. Values from published experimental results are presented as percentages of the model values for comparison. Substantial inter-observer variation is notably large relative to the intra-observer variability, indicating that differences in experimental protocol result in significantly differing results. In fact, variation in range of motion during stiffness testing has been explicitly demonstrated [90]. Model predictions are within the range of published values for all ROM orientations (Table 3).

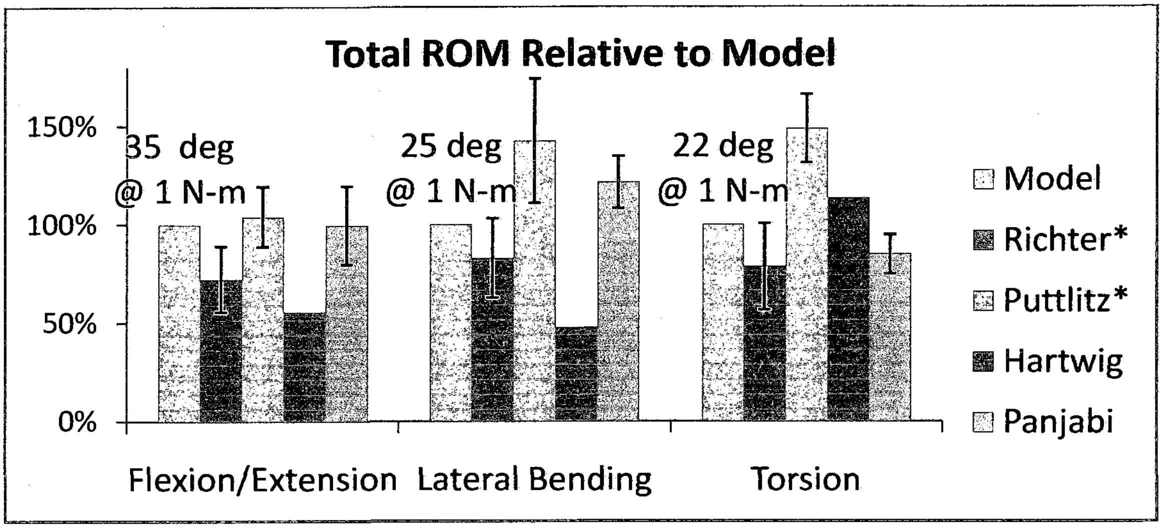

Table 3 – Comparison of model predictions of total range of motion to published experimental values. Standard deviations are shown where available. Values are presented as percentages of the model predicted values. Substantial inter-observer variability is evident. *Values from Richter and Puttlitz are extrapolated from single functional spinal unit results [47, 97, 106, 109].

Table 4 presents results for predictions of secondary coupled rotations.

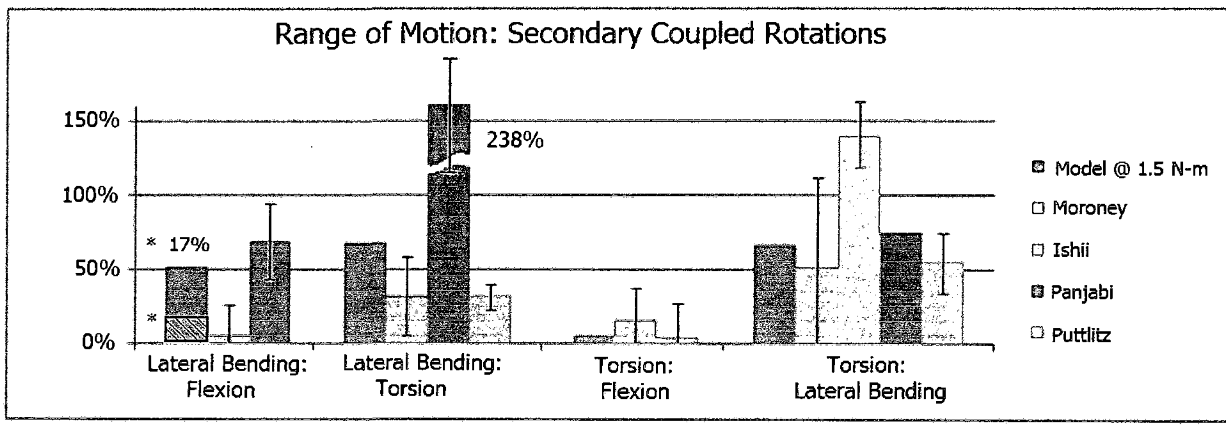

Table 4 – Comparison of coupled rotation predictions from the model to published experimental results. Rotation values are expressed as a percentage of the rotation in the primary load axis. Left to right: couple flexion and torsion under lateral bending moments, coupled flexion and lateral bending under torsion moments. * The use of a pure lateral bending moment did not change the coupled torsion but reduced the coupled extension 65% (left, shaded box) [58, 77, 94, 97, 106].

Inter-observer variability in coupled rotations is more severe than inter-observer variation in primary ROM values. This result is understood as a result of the widely varying experimental protocols used, which significantly affect the coupled rotations observed. Model predictions are within the published ranges for all coupled motions. The bending moments and follower load in the model were applied as 'follower'-type loads, so that the orientation of the load moves as the body displaces and deforms. While this had little effect under flexion and extension, the use of a follower technique in conjunction with the significant couple rotations observed in lateral bending resulted in an increased coupled flexion. By altering the definition of the applied lateral bending load such that it remained parallel to the original axis, the coupled extension under lateral bending was reduced from 51% to 17% , while the coupled torsion remained unchanged. This is a further indication of the sensitivity of coupled rotation predictions to experimental protocol.

Total facet contact forces measured by Tekscan were investigated as parameters of primary interest in this research programme (Figure 33, next page). It was noted that experimental measurements were less than model predictions under extension and lateral bending. However, further investigation revealed that under these conditions, the contact area extended beyond the region of pressure measurement on the Tekscan sensors. Under lateral bending, the percentage of cells around the Tekscan sensor perimeter being loaded ranged as high as 28% (Figure 34). For a bilaterally symmetric pressure distribution centered on the sensor perimeter, 25% perimeter recruitment could indicate that fully half of the contact force would not be indicated by the sensor. This unavoidable circumstance is due to the geometry of the cervical facet joint and the articular pillars, which prevent the sensile area of the sensor from being inserted fully into the contact region.

In an attempt to account for contact force underrepresentation, a measure of projected facet contact force was developed. Axial symmetry of the contact pressure distribution about the measured center of pressure was assumed. The contact pressure distribution in the region external to the sensor area was estimated using the average contact pressure for equivalent

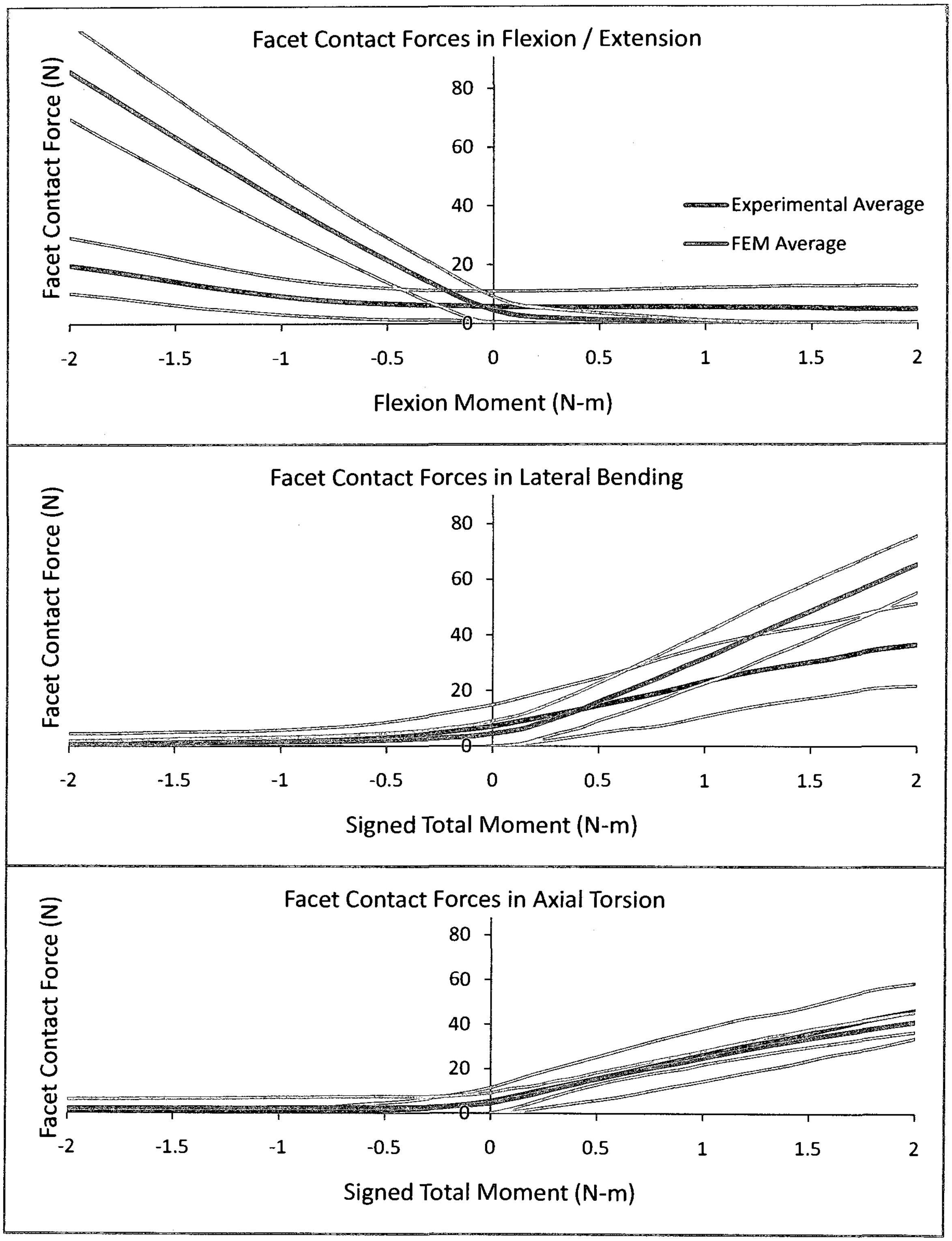

Figure 33 - Experimental facet contact forces from Tekscan for C4/C5 and C5/C6 articulations compared with FEM predictions. Means ± 1 standard deviation. For lateral bending and axial torsion, Signed Total Moment is the total bending moment in the direction of peak force, such that left- and right-side facets may be taken together.

positions within the sensor area. The contact pressure distribution in the region external to the sensor area was estimated using the average contact pressure for equivalent positions within the sensor area.

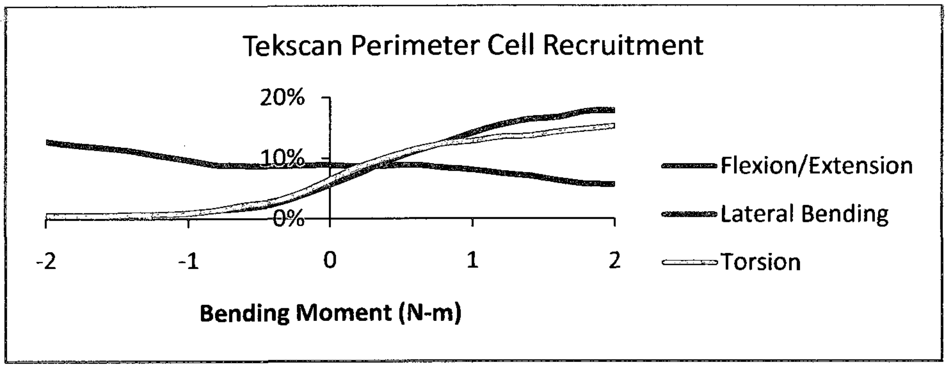

Figure 34 - Tekscan perimeter cell recruitment, expressed as the percentage of cells on the perimeter of the sensor that are being loaded. Higher values indicate greater underrepresentation of contact force. For lateral bending and axial torsion, signed moment values are presented so that left and right facets may be taken together.

This method underestimates forces somewhat because symmetry was assumed about the measured center of pressure, which is shifted centrally relative to the actual center of pressure. However, better agreement is observed between model and experimental results using this method (Figure 35). While this method should not be considered predictive, it is a useful tool for estimating the fraction of true contact force in an interaction that is not represented by the Tekscan due to geometric constraint in the confined space of the cervical facet joint.

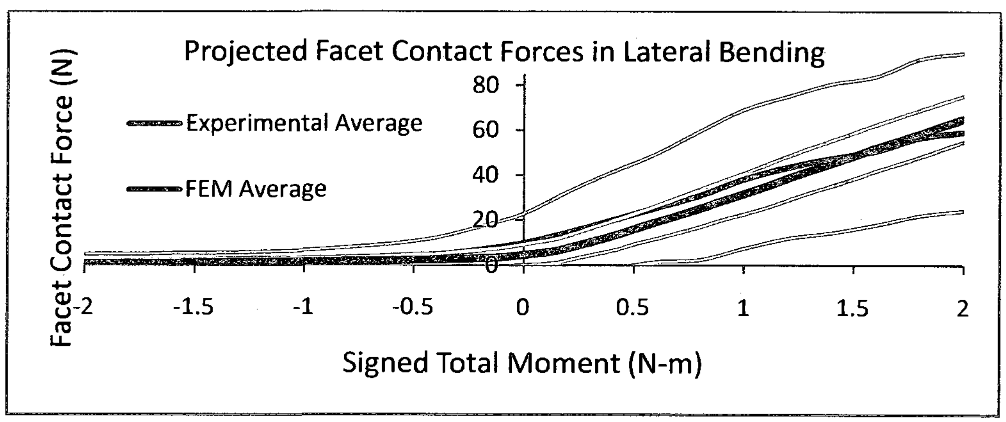

Figure 35 – Projected facet contact forces in lateral bending are in good agreement with model predictions. Signed moments are presented so that left and right facets may be taken together. Mean ± 1 standard deviation.

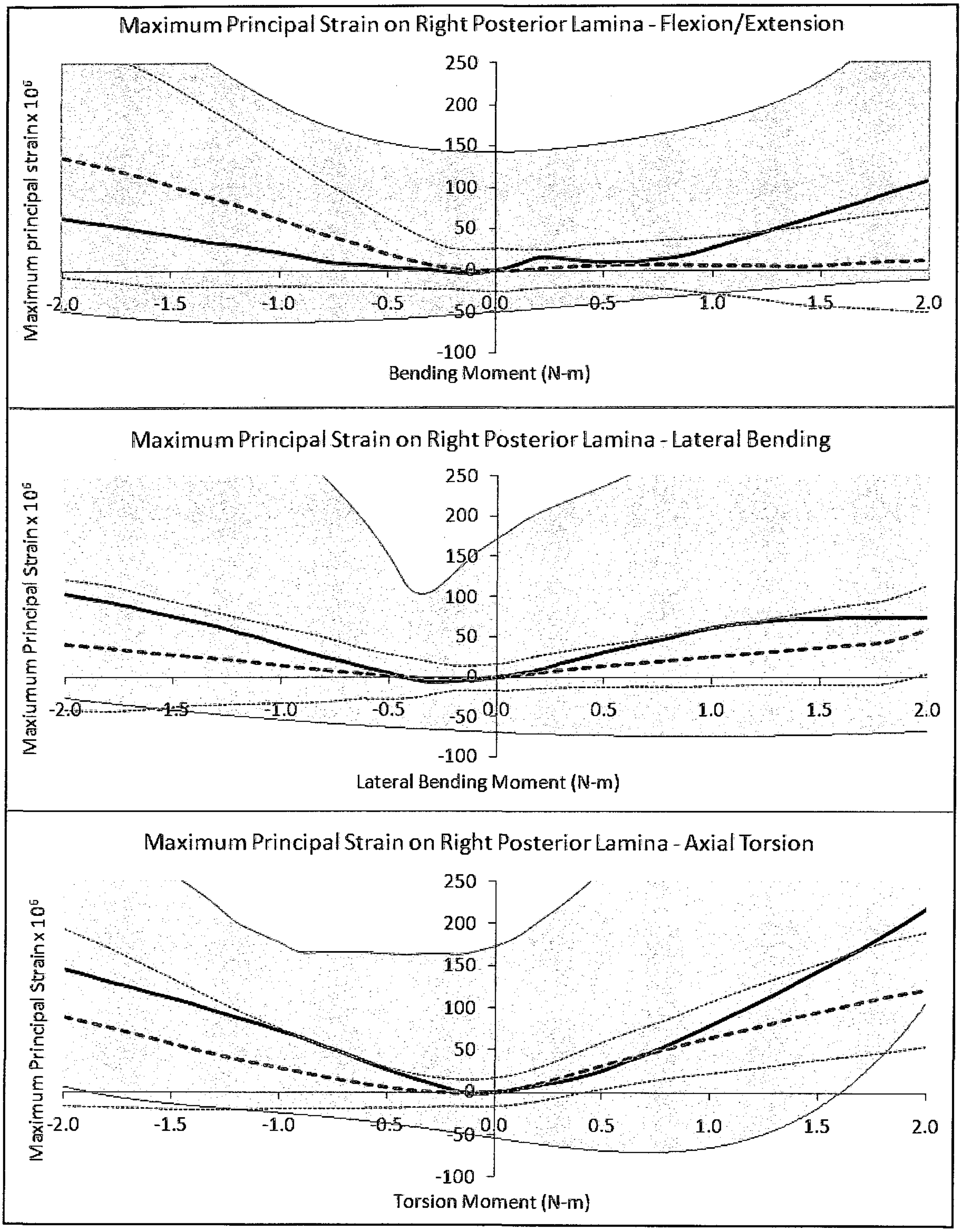

Figure 36 - Maximum principal strain on the right posterior laminae of C4-C6 from the model (—) are in agreement with experimental results (---, mean ± σ). Range data from the model for the region of interest (shaded) indicate high strain gradients in the sample region.

Range of motion, coupled motion, and facet contact force predictions based on the finite element model are in good agreement with experimental and published results.

The maximum principal strain measurements obtained experimentally agree with the model predictions (Figure 36, previous page). However, the range of strains in the sample region from the model indicates the presence of a high strain gradient over the sample region. The range is slightly higher under lateral bending and torsional loads, which may be an indication of beam bending loading of the posterior lamina, which would be expected to produce such a strain gradient in the sample region.

The increase in nuclear pressure under axial compression and lateral bending predicted by the model was borne out experimentally (Figures 37 and 38). However, the range of nuclear pressures observed experimentally was high, and substantial variation in nuclear hydration and stiffness was observable.

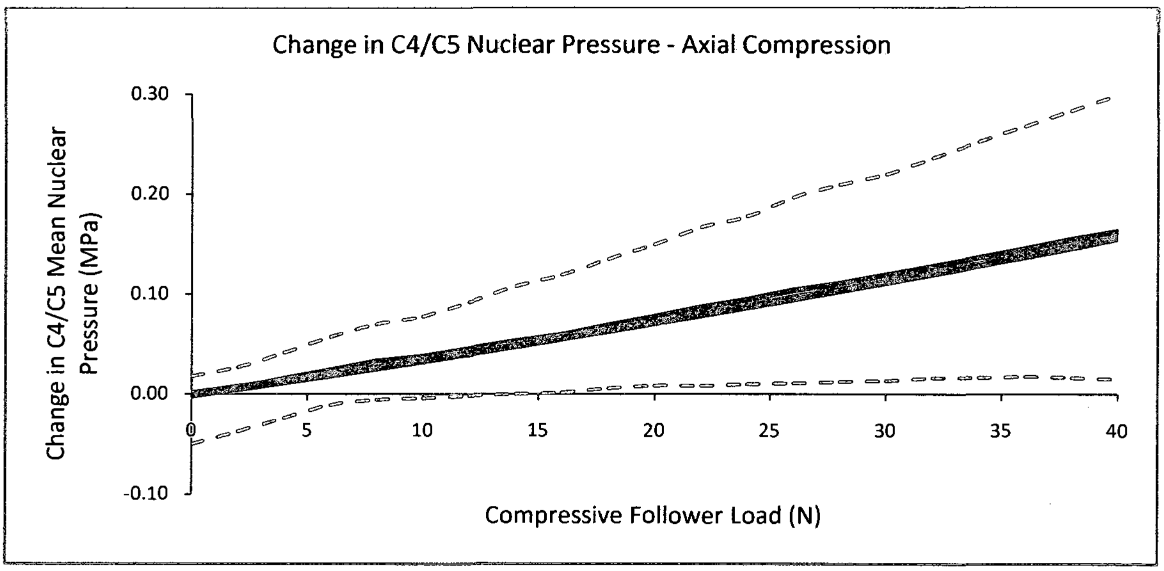

Figure 37 - The increase in mean nuclear pressure at the C4/C5 level under axial compression of 40 N predicted by the model (—) is in good agreement with experimental observations (—, ± 1 standard deviation).

Consistent pressure measurements were difficult to obtain for the more degenerate nuclei, where pressure in the nucleus was more spatially variable and good contact between the transducer and the nucleus pulposus was in question. If the nucleus pulposus behaved as a hydrostatic fluid, any asymmetry in the nuclear pressure under lateral bending and axial torsion would be due to geometric asymmetry. Model predictions indicate that that this effect should be small (Figure 38). However, significant asymmetry and variability were in fact observed experimentally, and pressure measurements were strongly affected by transducer placement. Additionally, nuclear exudation following transducer extraction was only observed in one specimen. These observations indicate that the nucleus pulposus, for the specimens tested, did not generally behave as a simple hydrostatic fluid. Additionally, the sensitivity of pressure measurements to pressure transducer placement was most pronounced on specimens exhibiting degenerative features such as osteophytes. This observation also indicates that the spatial variability was likely due to normal age-related changes in the constitution of the nucleus pulposus.

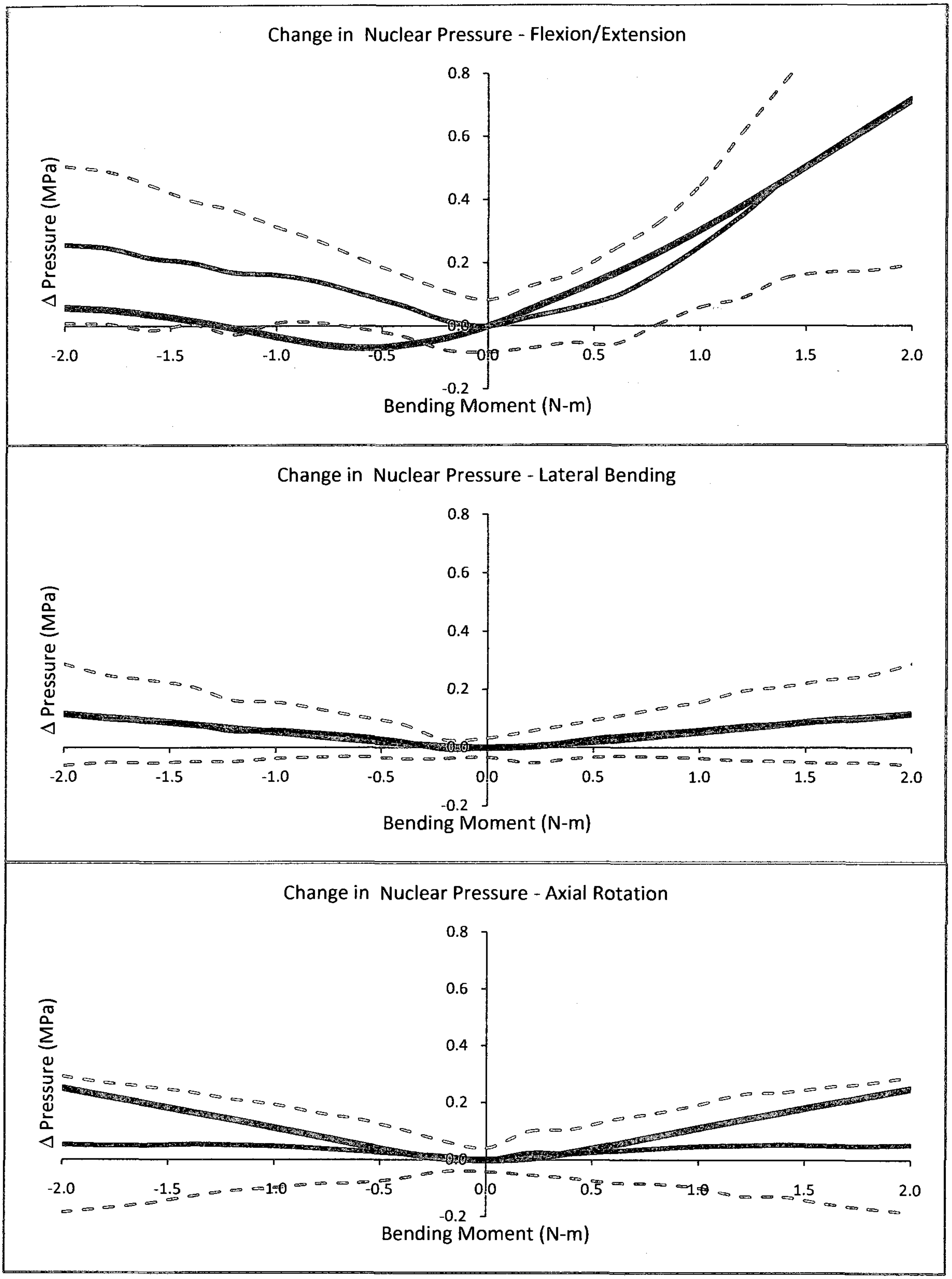

Figure 38 - Model predictions (—) of increase in nuclear pressure under flexion/extension, lateral bending and axial torsion compare favorably with experimental results (—, ± 1 standard deviation). Lateral bending and axial torsion data are symmetrized for clarity.

Anterior bulge of the intervertebral discs was measured photographically at 2 N-m under flexion and extension for visible levels at a consistent scale and orientation using a tripod. The anterior profiles were traced, and the traces were registered by rotation and translation. Experimental disc bulge was then recorded by measuring the maximum relative anterior displacement under flexion relative to extension. Scale was provided by the 3 mm cord used for application of the follower load (Figure 39).

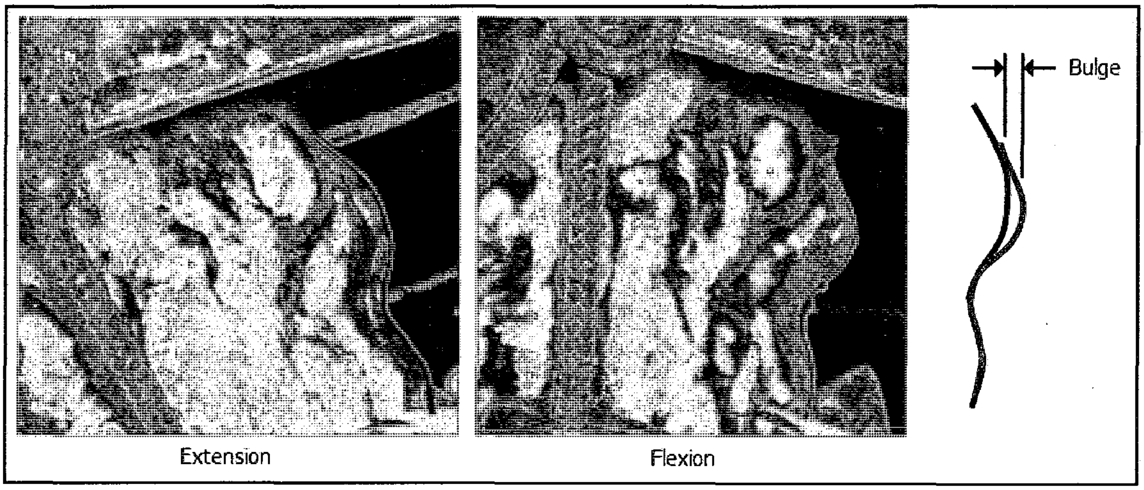

Figure 39 - Disc bulge measurement. Anterior profiles were traced under flexion and extension at 2 N-m. Traces were rotated and correlated, and bulge was measured. Scale is provided by the 3 mm cord.

The disc bulge predictions of the model were calculated by subtracting half the displacement of the anterior caudal limit of the C6 anterior body from the displacement of the central anterior aspect of the C6/C7 annulus (Figure 40). The relative bulge was defined as the total range or disc bulge under flexion/extension. The total bulge at C6/C7 predicted by the model, 1.4 mm, compares favorably to the experimentally observed distribution of 1.3 $\pm$ 0.6 mm.

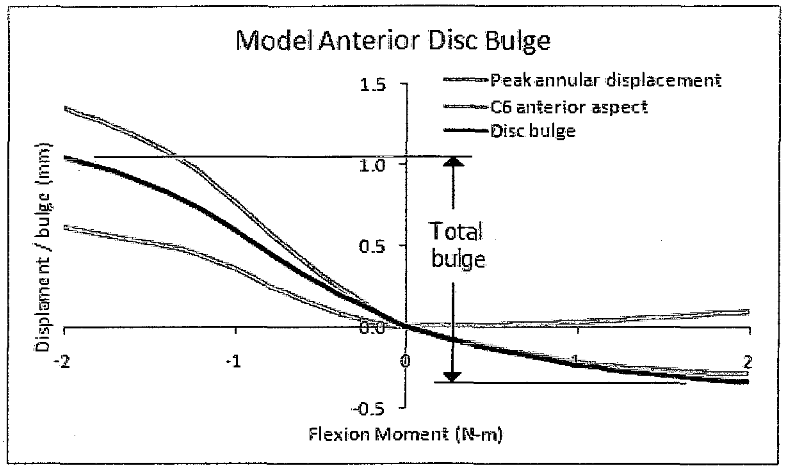

Figure 40 - Model disc bulge measurement for the C6/C7 annulus.

Appropriate validative metrics have been provided where possible for the finite element model predictions of cortical strain, range of motion, facet contact forces, intradiscal pressure, disc bulge, and annular mechanics. Model predictions of the effect of facet cartilage thickness and disc replacement follow.

5 Effects of Cartilage Thickness Models on Contact Parameter Predictions

It has been proposed that changes in segmental mobility and antero-posterior load sharing in the cervical spine may lead to subsequent degeneration [62]. Many finite element modeling efforts have investigated these parameters, particularly as they are affected by disc degeneration, ACDF, and disc replacement procedures. However, while high fidelity to facet cartilage parameters such as cartilage thickness distribution, articular and osteochondral surface geometry, and joint conformance has generally not been maintained in such efforts, the impact of oversimplification of these parameters has not been established. It is clear, for example, that peak contact pressures increase as joint congruence is diminished. It is desirable, therefore, to establish the sensitivity of finite element predictions of clinically relevant parameters such as contact pressure distribution, kinematics, and total contact forces and load sharing to variation in model representation of the articular cartilage.

Methods

Pursuant to this aim, the thickness of the articular cartilage layer of the lateral facets was measured experimentally. A novel mathematical model of the thickness distribution was developed and validated (See Appendix) [136]. To examine the effects of different cartilage thickness models on kinematics, contact forces and pressures, and antero-posterior load distribution, three additional sets of models were generated (Figure 41). Each of these modified cartilage distribution models was based on the intact (baseline) model, and varied only with respect to the different cartilage distributions modeled.

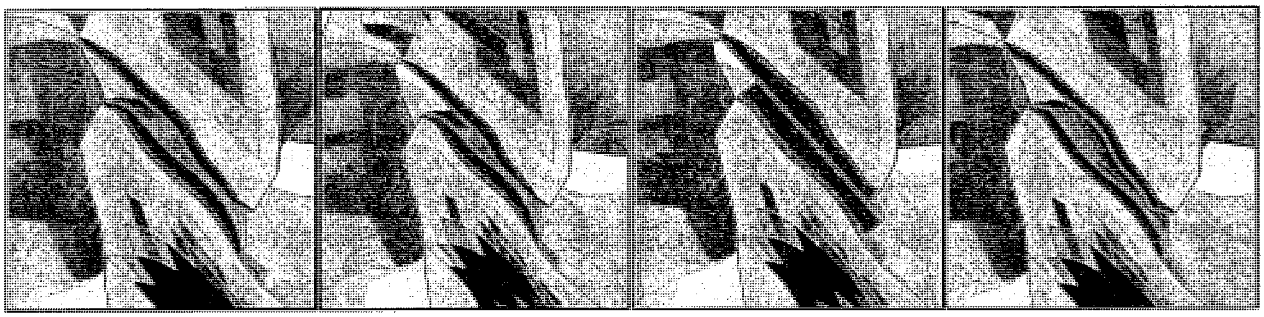

Figure 41 - Cartilage thickness models, unloaded. Cutaways at C6/C7 (intact, left side). Baseline, k=0.75, flat, and constant thickness (left to right). Three distinct cartilage layers (green) are apparent.

A constant thickness model was developed, with thickness specified at the published mean cartilage thickness on the lower cervical spine of 0.48 mm [86, 141]. The same thickness was used for all facets, and differences between vertebral levels and between inferior and superior facets were neglected. This model was intended to reflect a commonly reported modeling approach. The first ring of nodes around the perimeter was given a thickness of 0.05 mm. The reduced thickness at the edge was introduced to resolve convergence difficulties associated with edge-to-edge contact that otherwise occurred.

A second model was developed having a spatially-varying thickness distribution per Womack at al [86, 136, 141], using a more aggressive thickness fitting parameter k of 0.75. This represents an upper limit to the distribution of k values observed experimentally, and is two standard deviations above the mean. Peak cartilage thickness was specified at published values, and was identical to the baseline model, varying by level and inferior/superior position, but not left to right [141].

A flat cartilage model was developed with spatially-varying thickness and planar articular surface geometries [86]. Initial parallelism of articulating surface pairs was enforced, and an initial gap of 0.05 mm was prescribed for all facet joints. Cartilage thickness was governed by the prescribed gap.

The various cartilage distribution models were compared with respect to predictions of overall kinematics and range of motion and facet joint contact forces, areas, mean and peak pressures, and center of pressure tracks.

For the constant-thickness model it was anticipated that facet contact would tend to be established around the perimeter, and that contact areas would be underestimated. It was anticipated that average and peak contact pressures would be overestimated, and that center of pressure tracks would be less linear than observed tracks. For the planar facet surface model, it was anticipated that peak and mean contact pressures would be underestimated under axial compression, and overestimated under flexion/extension and lateral bending. It was anticipated that contact area would be overestimated under axial compression and underestimated under bending loads. For the modified spatially-varying thickness model, it was anticipated that peak contact pressures would be reduced from the baseline model predictions, and that contact areas would increase. It was anticipated that centers of pressure would be shifted away from the facet perimeters, and that joint congruence, as measured by contact gap variation, would be reduced. The effects of cartilage representation on joint congruence at rest and under lateral bending are given in Figure 41 and Figure 42, respectively.

Figure 42 – Joint congruence under load was strongly affected by cartilage representation. C6/C7 (left) cutaway under left lateral bending at 2 N-m. Baseline, k=0.75, flat, and constant thickness (left to right). Poor congruence of the constant thickness model results in a two-point contact pattern.

Results and Discussion

Range of motion under lateral bending and axial torsion was unaffected by the representation of cartilage used. Range of motion under flexion was unaffected, but the ROM under extension for the flat cartilage thickness representation was reduced in the mid-range (-0.5 to -1.8 N-m), and was more linear overall (Figure 44). This is likely due to the reduced initial clearance of the flat model. Notably, all the models would have been accepted for validation regarding ROM.

Cartilage representation had little impact on the predicted total contact forces (Figure 45). The flat cartilage model did exhibit higher contact forces under forward flexion, where contact was maintained by the reduced contact gap, and at the extrema of lateral bending and axial torsion.

The augmented Lagrangian and hard contact formulations were both found to result in difficulty obtaining model convergence. This effect was largely due to the combined effects of mesh density, high curvature in the region of contact, the compliance of the cartilage in contact, and the presence of edge contact. A tabular semi-exponential contact formulation was used to overcome these limitations, with the effect that most nodes reported some finite contact pressure even while the contact opening distance was finite and positive. For this reason, contact area could not be directly queried. Contact areas for the models were calculated as contact force divided by mean contact pressure. Mean contact pressure was calculated by examining the mean pressure of the nodes for which contact pressure exceeded 0.01 MPa (Figure 46). This threshold was found to result in contact area predictions that corresponded to predictions obtained using "hard" contact formulations. Figure 47 presents the effects of cartilage thickness models on contact area predictions. Contact area from Tekscan used a threshold pressure of 0.0 MPa, which is responsible for some of the difference between the Tekscan and model values.

Because the contact forces are similar between the models, lower contact pressures and larger contact areas represent measures of greater correspondence between the contact surfaces. The flat cartilage model predicts substantially higher contact areas generally. It is particularly notable that the mean contact area for the flat model under flexion/extension is greatly exaggerated in the neutral position, but is significantly reduced at the extrema. This result corroborates the hypothesis that flat cartilage representations will alternatively over- and under-estimate the contact area as the pair moves from edge contact at the anterior, to nearly complete contact, to edge contact at the posterior(Figure 43).

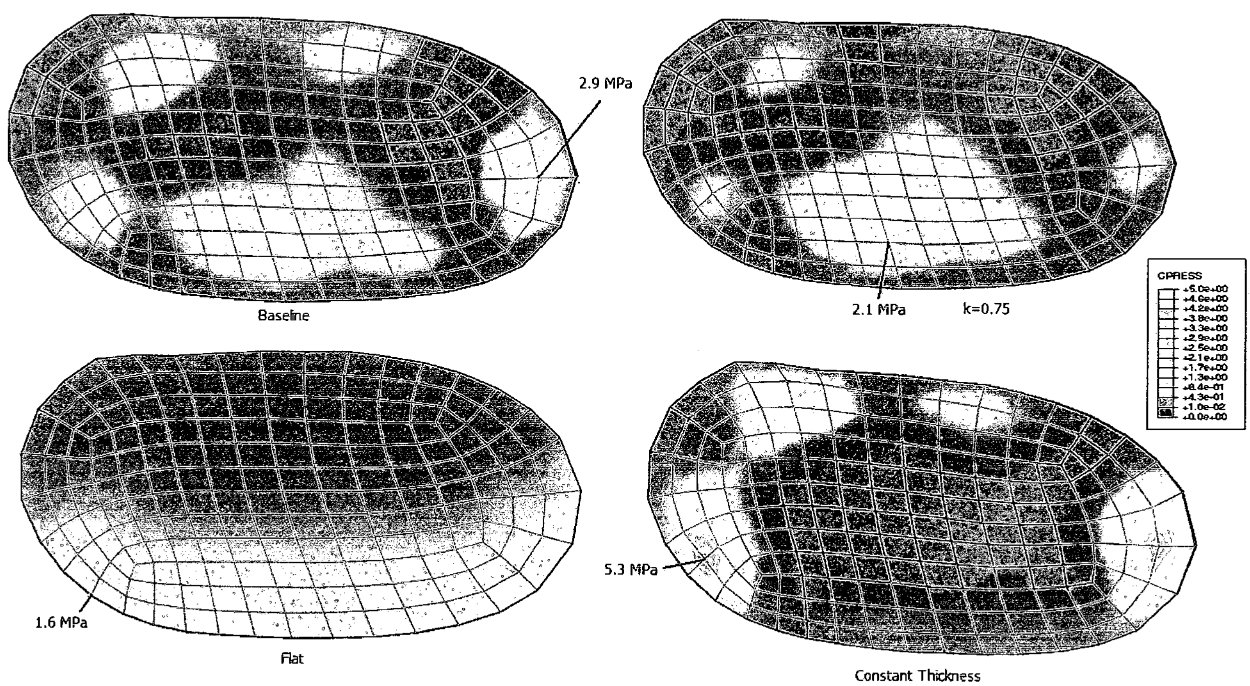

Figure 43 - Contact pressure distribution at C6/C7 (left) under lateral bending at 2 N-m. Peak pressures and contact areas are exaggerated and underrepresented, alternately, for the flat and constant thickness models.

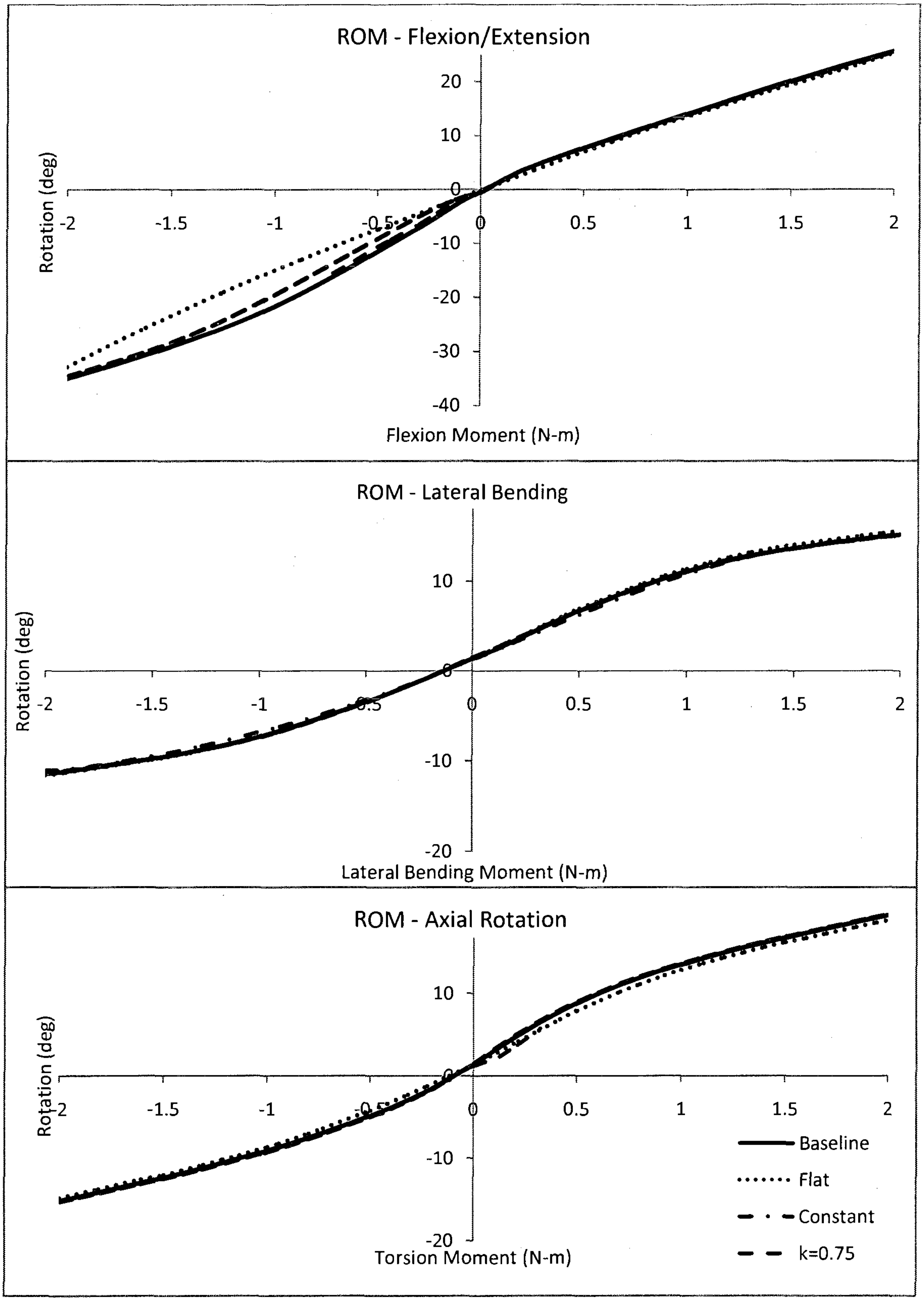

Figure 44 - Range of Motion - Cartilage thickness has little effect.

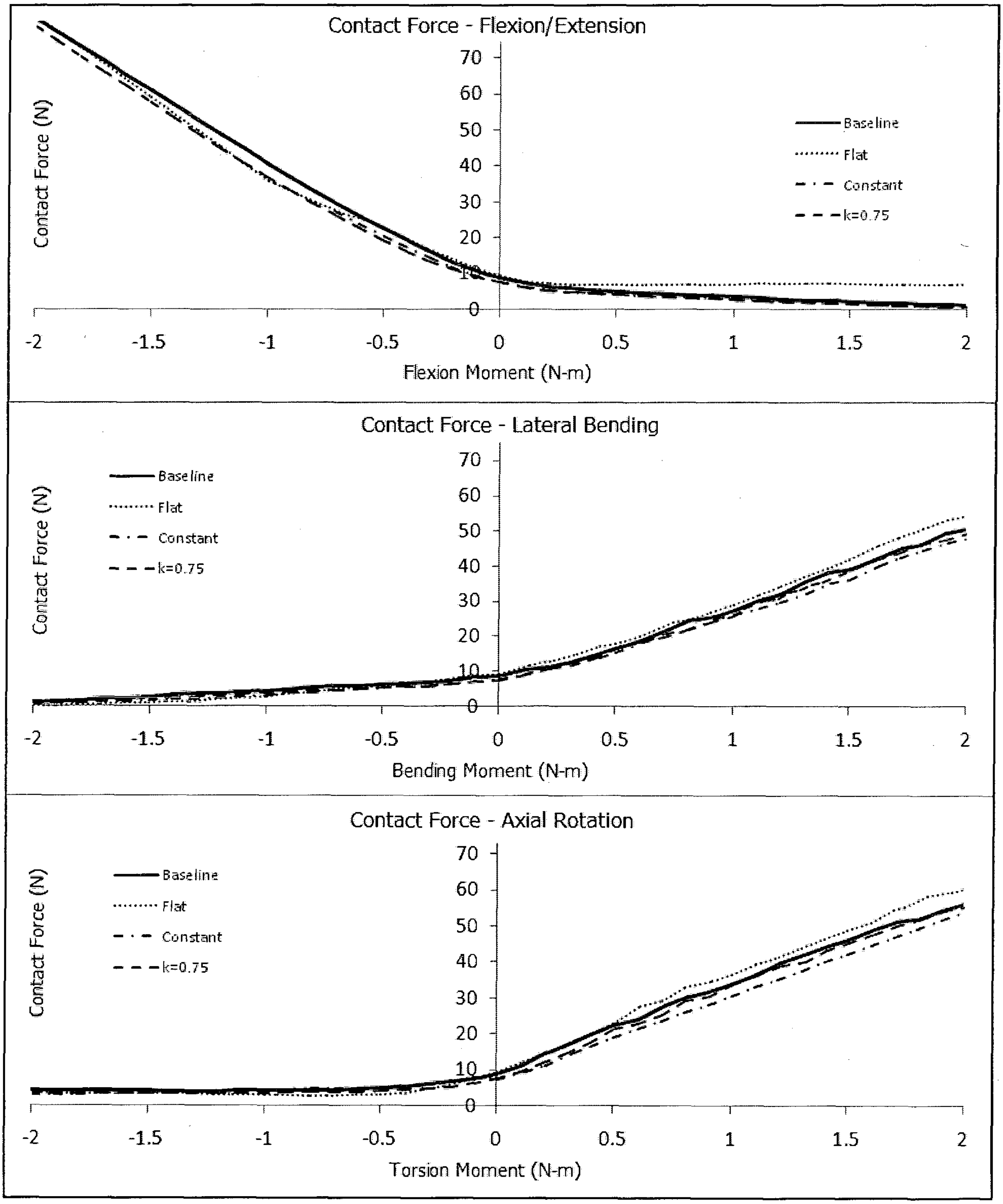

Figure 45 - Contact force was little affected by cartilage representation. Reduced gap for the flat model results in slightly higher forces.

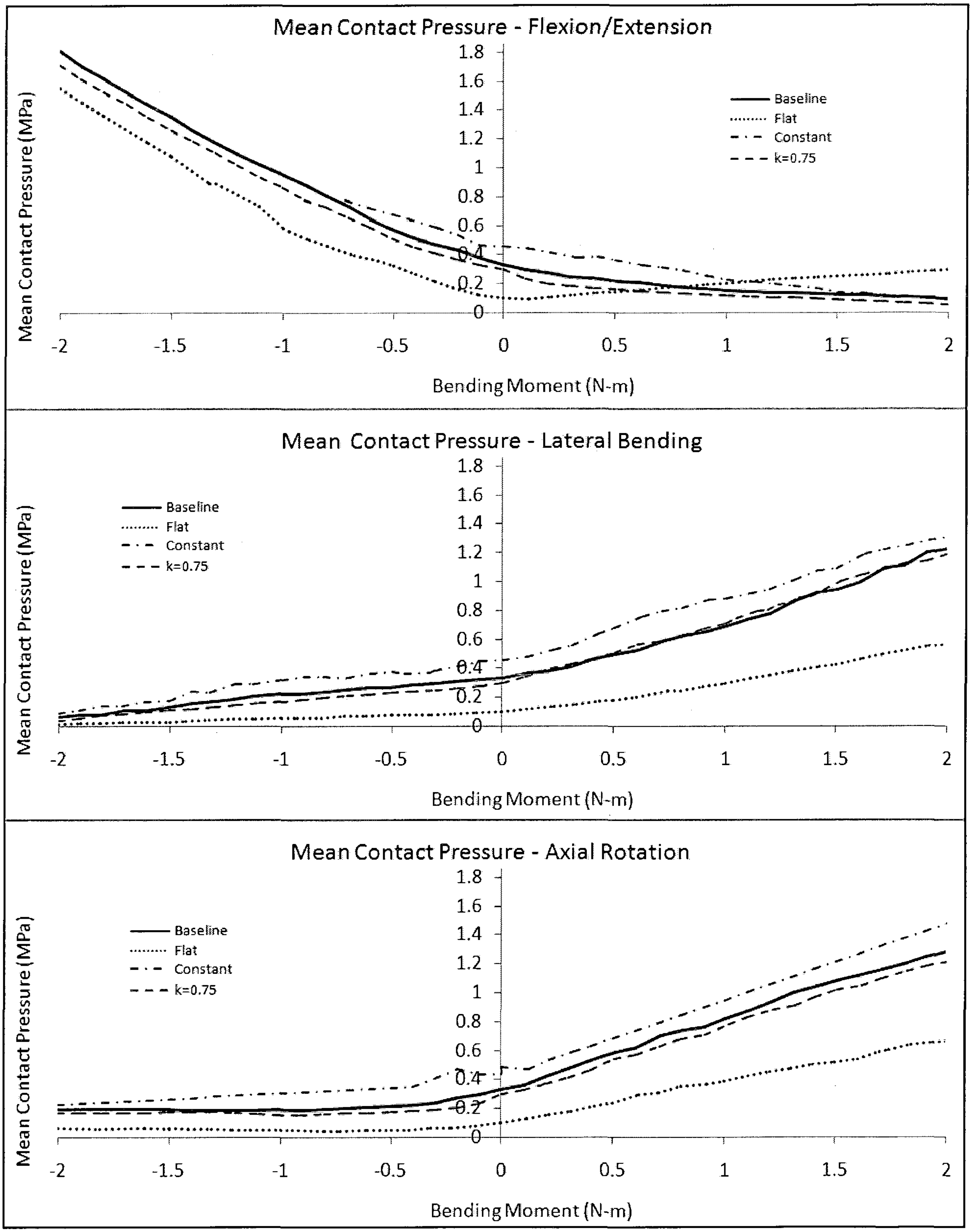

Figure 46 - Mean contact pressure for the facet contact regions. Contact pressure is generally higher for the constant thickness model, and lower for the flat model.

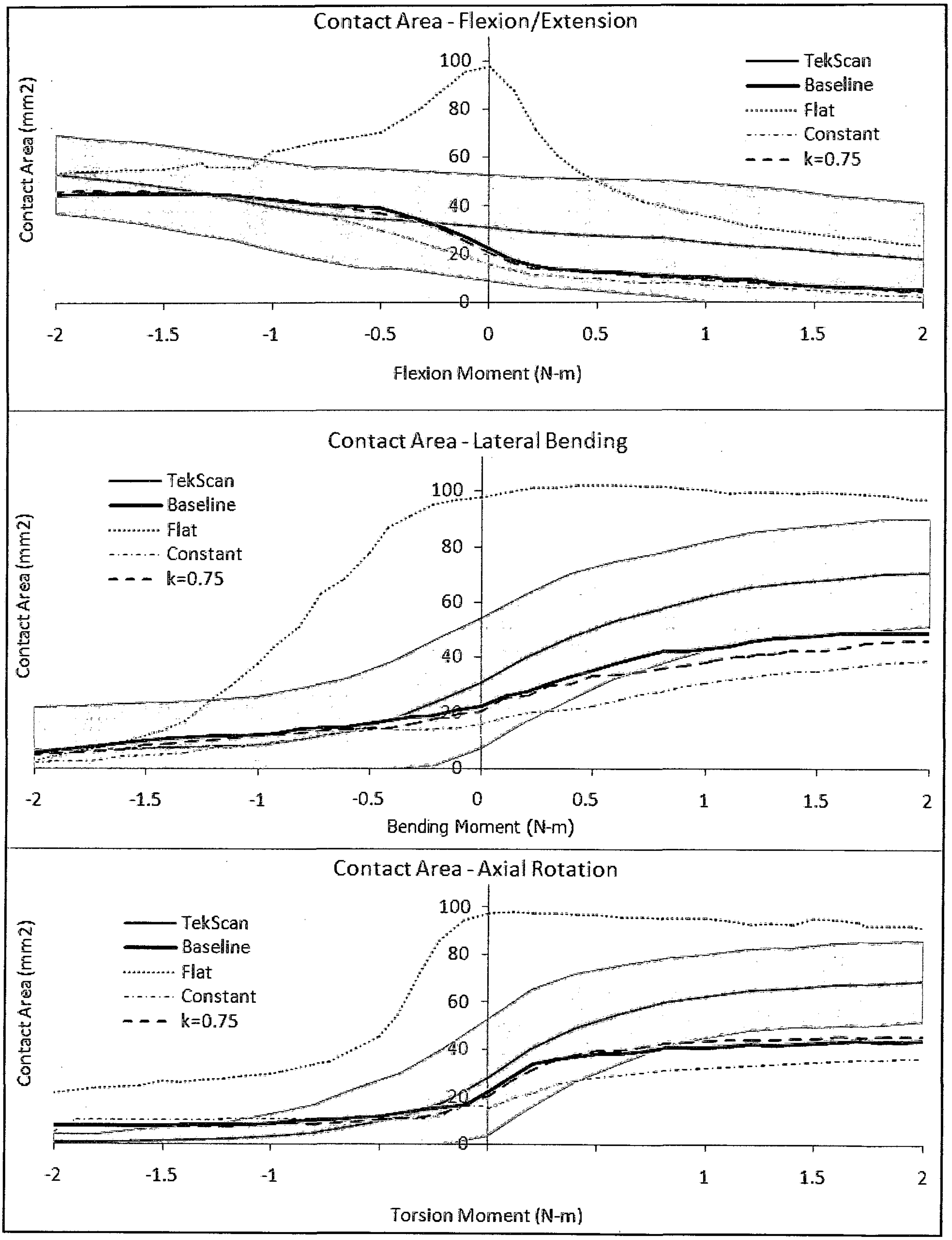

Figure 47 - Contact area – experimental mean ± 1 standard deviation (shaded)

The constant thickness model resulted in reduced contact areas and increased mean contact pressures relative to the variable thickness models, as anticipated (Figures 46 and 47). The differences, however, were lower than expected. Further inquiry reveals that the contact area reductions predicted using a constant thickness model increase with mesh density. This effect is due to the surface-to-surface contact formulation employed by ABAQUS which has an intrinsic smoothing effect, causing highly curved faceted surfaces to be treated as smoother surfaces. The effect is related to the degree of curvature between adjacent facets, resulting in the mesh-size dependency, and is not relevant for the flat cartilage representation. Paradoxically, the result of this effect is to *improve* the predictions of contact pressure and contact area as mesh density *decreases*, but only for models whose geometry should result in very small contact areas in regions of high curvature, such as the constant thickness cartilage model. This effect can be observed as apparent gross over-penetration at nodes that report low or no contact pressures.

Peak pressure is reported in Figure 48. Peak pressure was calculated as the third quartile pressure value (per contact surface) for nodes considered to be in contact – i.e., with pressure exceeding 0.01 MPa. This representation was considered to be more representative of peak pressure than a simple maximum pressure value, which is much more sensitive to the geometry of the contact surfaces. Peak pressure trends and inter-model relationships duplicate those observed in mean pressures. Both the baseline and k=0.75 variable thickness models provide very good fits to the Tekscan data. All models predict higher peak pressures than the Tekscan under extension, but the Tekscan perimeter cell recruitment was fairly high under extension. These results indicate that the third-quartile or 'peak' pressure is a good indicator of peak physiologic pressure for the baseline model.

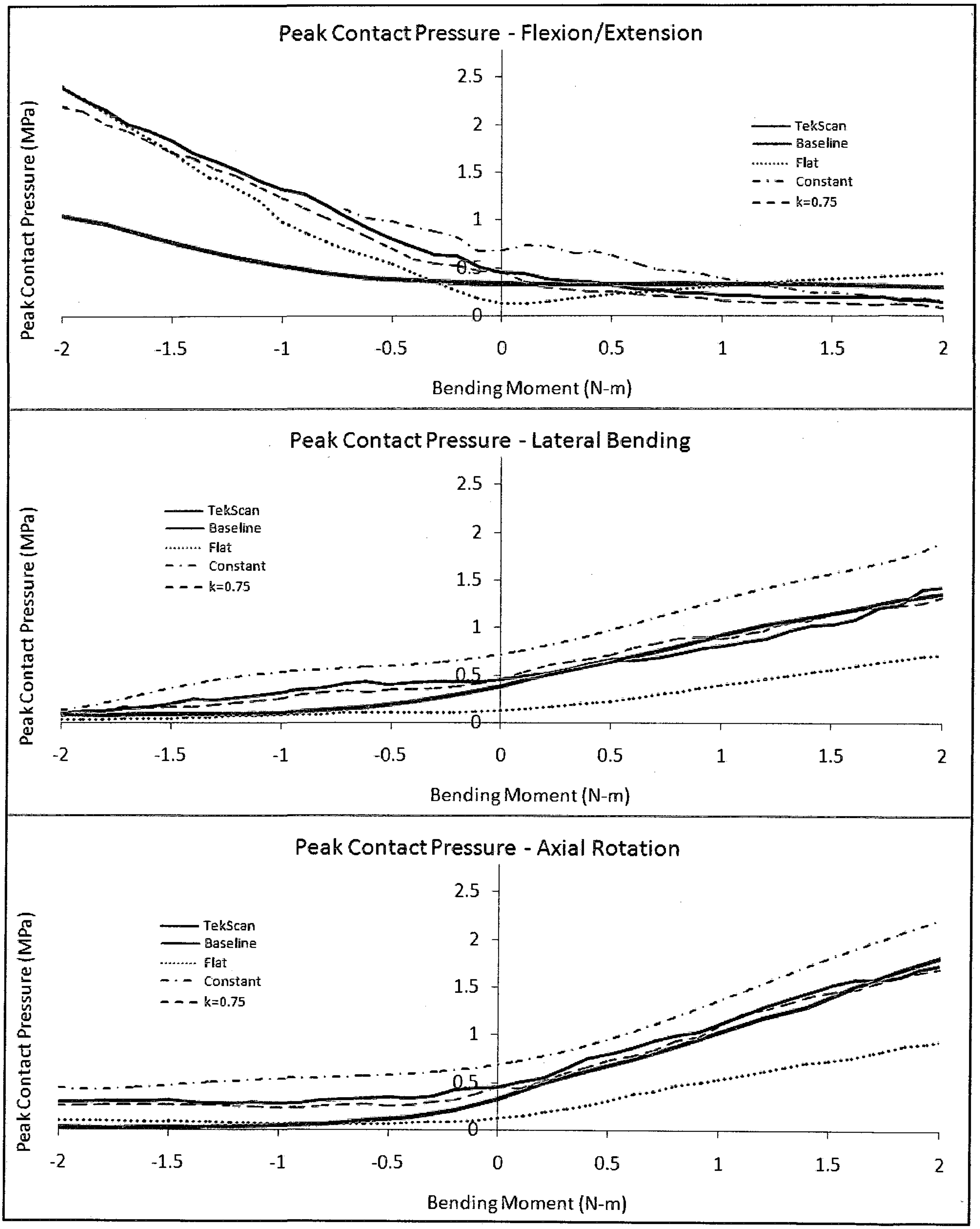

Figure 48 - Peak contact pressure represents the third quartile pressure for nodes exceeding 0.01 MPa.

Facet contact center of pressure tracks are presented in Figures 49-51 (following pages). Center of pressure data were analyzed by transforming the (x,y,z) coordinates of the center of pressure for each contact pair according to a moving coordinate system attached to the caudal vertebra in the contact pair, which was reconstructed according to the displacements of three nodes on the anterior surface of each vertebra. The relative center of pressure for each contact pair was then normalized to the center of pressure of the contact pair in the baseline case in the neutral position. This is responsible for the correspondence of the "Start" coordinates for the baseline cases. Finally, the coordinates were transformed into the coordinate system of the plane parallel to the facet surface, and offset by an arbitrary (±5,0) mm displacement in order to facilitate distinction of the left and right interactions.

Center of pressure tracks for the k=0.75 model are trivially different from the baseline model for all load cases, with less than 0.5 mm offsets in the neutral position for all interactions. The baseline model exhibits an AP range of only ±2 mm for all load cases. This range is less than the relative displacements of the interacting surfaces under flexion/extension. The flat model exhibits a much greater AP range of 12 mm in flexion/extension with peak contact forces at *both* limits, which is again representative of contact that varies from edge contact at the anterior and posterior extrema to whole-surface contact in the neutral position. The neutral position centers of pressure for the flat model are shifted 1.8 mm anteriorly and 2 mm laterally on average, relative to the baseline case. Differences between the baseline case and the flat model are greatest under flexion/extension (Figure 49). The neutral position centers of pressure for the constant thickness model are shifted 1 mm laterally on average, relative to the baseline case.

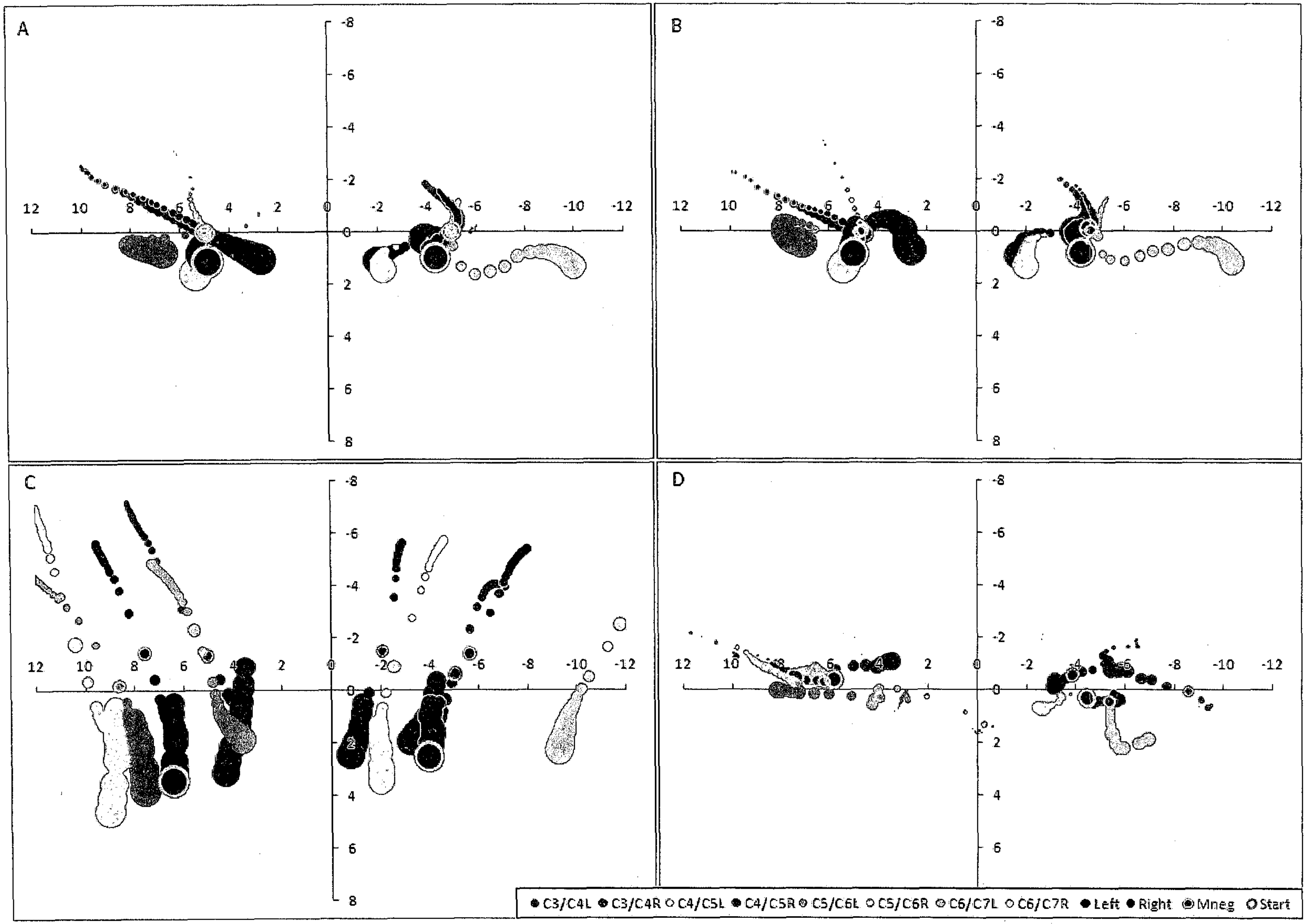

Figure 49 – Center of pressure tracks - Flexion/Extension. A) Baseline, B) k=0.75, C) Flat, D) Constant thickness. Range for constant thickness is -0.8 to +2 N-m. Bubble size represents contact force. Coordinates are normalized to (±5,0) at the neutral position in the baseline model with respect to the caudal vertebrae. Averages for left and right are given, with the extension limit marked (grey circles). Neutral position centers of pressure are marked (grey circles).

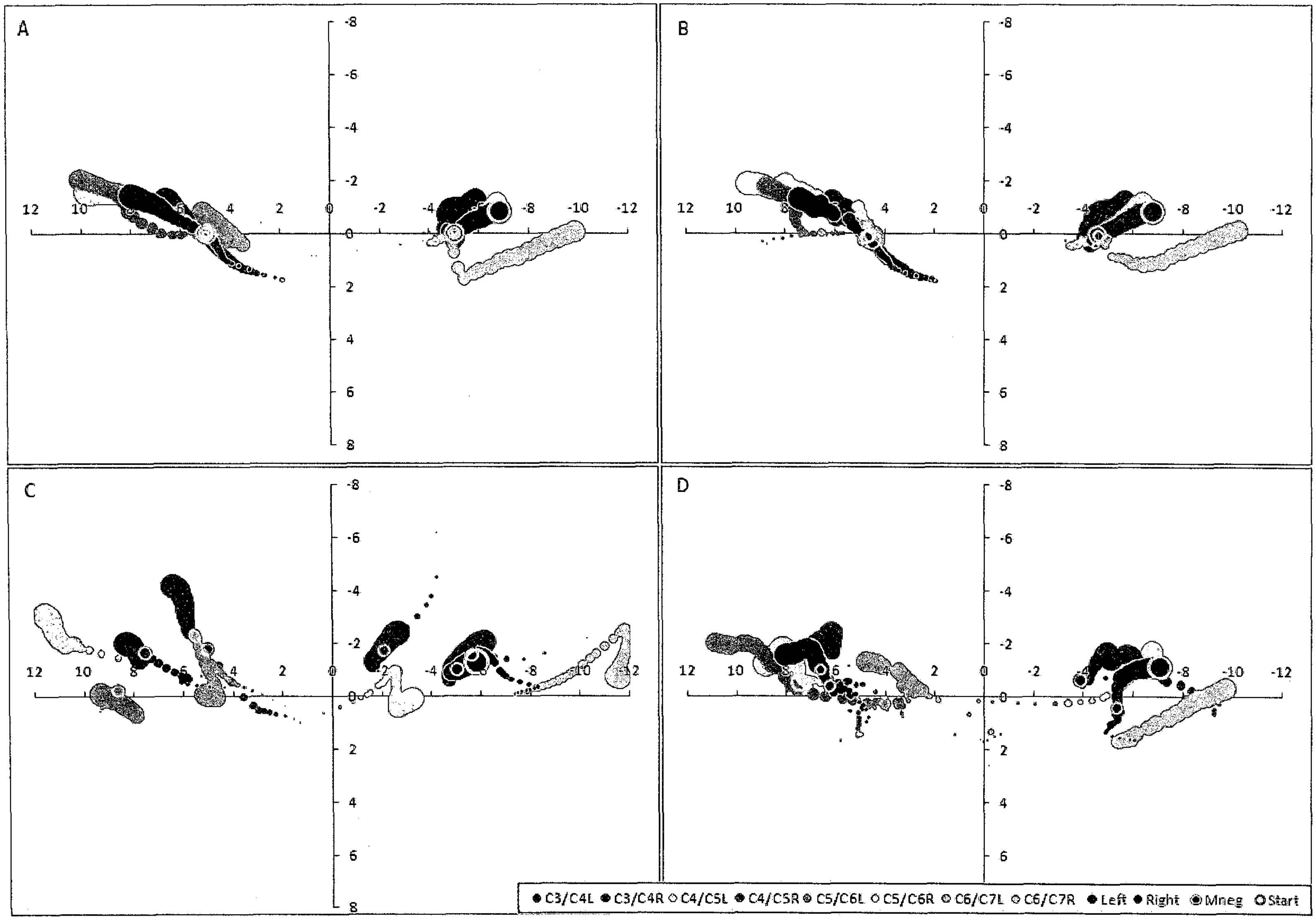

Figure 50 - Center of pressure tracks – Lateral Bending. A) Baseline, B) k=0.75, C) Flat, D) Constant thickness. Bubble size represents contact force. Coordinates are normalized to (±5,0) at the neutral position in the baseline model with respect to the caudal vertebrae. Averages for left and right are given with the right lateral bending limit marked (grey circles). Neutral position centers of pressure are marked (grey circles)

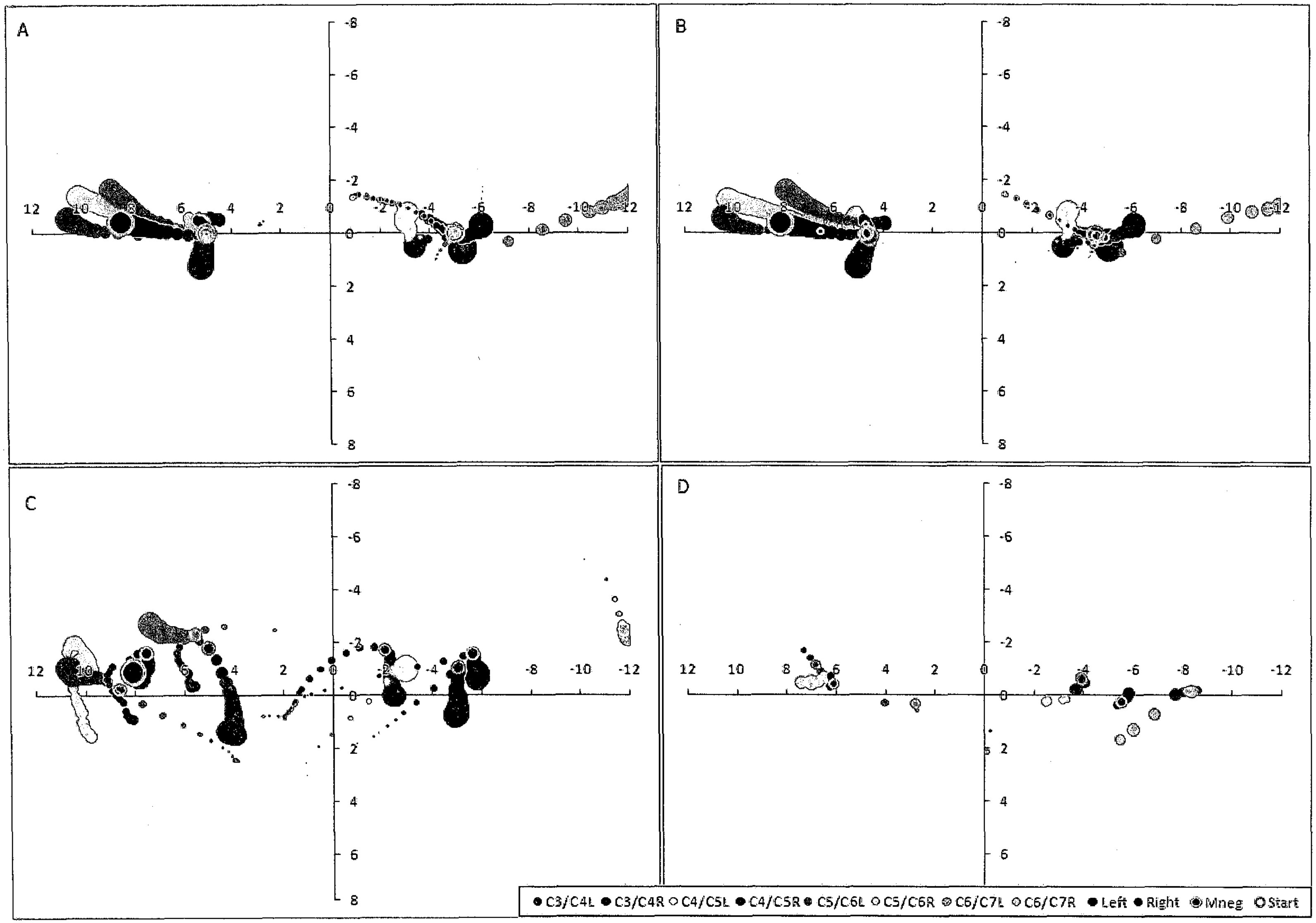

Figure 51 - Center of pressure tracks – Axial Torsion. A) Baseline, B) k=0.75, C) Flat, D) Constant thickness. Bubble size represents contact force. Coordinates are normalized to (±5, 0) at the neutral position in the baseline model with respect to the caudal vertebrae. Averages for left and right are given with the right axial torsion limit marked (grey circles). Neutral position centers of pressure are marked (grey circles). Constant thickness data are for 0 to +0.3 N-m.

The centers of pressure under lateral bending progress antero-laterally on the loaded side and postero-medially on the unloaded side, in a very consistent pattern for the baseline and k=0.75 models. Similar effects are seen for the flat and constant thickness models, but more variability is observed (Figure 50). Under axial rotation, a lateral-to-medial motion pattern is observed, with antero-posterior motion that is more variable and lower in magnitude (Figure 51).

Both the constant thickness and flat models exhibit motion patterns that are more variable between interactions and more tortuous than the baseline model, which is indicative of contact patterns that are shifting between multiple distinct regions, a pattern generally not observed experimentally. Figures 43 and 52 demonstrate this behavior graphically. The relationship between joint congruence and contact pressure and compressive strain distributions is apparent.

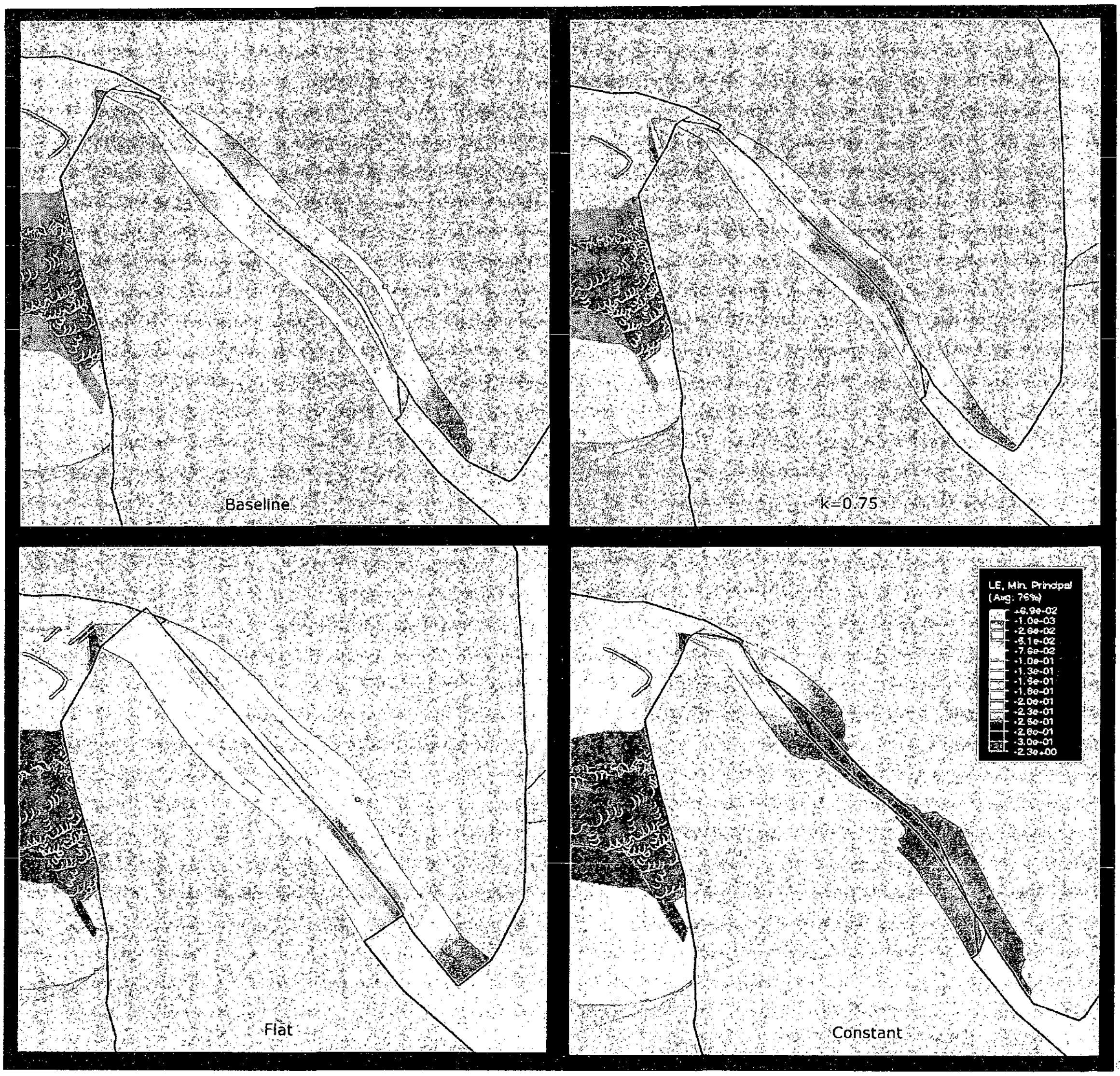

Figure 52 - Minimum principal strain at the C6/C7 left articulation reveals the effects of cartilage representation on joint congruence and contact pressures. Lateral bending at 2 N-m.

Conclusions

The only discernable difference in range of motion between the different cartilage thickness distribution models is the increased linearity and decreased compliance of the flat cartilage model under extension. All models would have met the validation requirements for range of motion, indicating that: (1) range of motion is not a good predictor of contact parameter prediction validity and (2) that range of motion predictions are insensitive to the representation of the articular surfaces (Figure 44).

Contact force predictions were insensitive to the cartilage thickness. The only notable exception is the slightly higher forces at the extrema of the flat model (Figure 45). These results indicate that contact force is more sensitive to the contact gap than the surface congruence. This is likely due to the combined effects of the tension in the facet capsular ligaments, which results in sensitivity to contact gap, and the compliance of the spine as a whole.

Both the mean contact pressure and contact area results are indicative of the underestimated joint conformity of the constant thickness model, which results in higher mean and peak pressures and reduced contact area predictions. Solution convergence was difficult to obtain for the constant thickness models, and could not be achieved for the full range of all load cases. The overestimation of contact pressures in the constant thickness model was less than expected, which would indicate that such models could be used with impunity. However, it must be noted that the pressure predictions of the low-conformance constant thickness model are much more sensitive to the contact formulation used than the more conforming models. This results in contact pressure and area predictions that, for constant thickness cartilage models, are highly sensitive to mesh refinement and the contact model and pressure-overclosure relationship. Paradoxically, while increased mesh refinement generally results in *lower* maximum pressures for conforming articulations, it may result in *higher* maximum pressures for poorly conforming articulations. Unfortunately, reduced mesh refinement for such a highly curved geometry may result in degraded model convergence behavior.

The contact area of the flat surface model was generally overestimated as anticipated, and was maximized in the neutral position. This is not surprising, as initial parallelism was prescribed in the initial geometry. Cylindrical conforming surfaces (with medial-lateral axes) would likely result in more consistent contact area under flexion-extension, but edge-to-edge contact patterns under lateral and axial moments. Advantages to the flat cartilage representation include improved model convergence behavior, and relative insensitivity to mesh resolution due to the joint conformity.

All model results indicate that the differences between the baseline (k=0.5) and k=0.75 models are trivial. This result is a positive indication for the use of variable thickness cartilage representation, particularly because k=0.75 represents a value two standard deviations above the experimental mean. This indicates that the use of a single value of k does not result in a noticeable deleterious effect. Peak contact pressures for both variable thickness models are in good agreement with experimental means. Additionally, the sensitivity of constant thickness model predictions and convergence behavior to mesh refinement and contact formulations provide motive for the use of physiologically accurate spatially-varying cartilage thickness representations.

Summary

In short, the four cartilage thickness models investigated indicate that:

- Cartilage thickness representation does not have a substantial impact on range of motion or global facet contact force predictions.
- Facet contact pressure, area, center of pressure and joint congruence predictions are sensitive to cartilage thickness representation.
- Accurate representation of the articular geometry and physiologic variation in cartilage thickness is important for accurate prediction of facet cartilage degeneration.

6 Disc Replacement and Load Transfer

The preservation of range of motion after disc replacement has been established experimentally [106]. While the segmental rotations can be preserved after disc replacement, preservation of antero-posterior load sharing and center of rotation at the treated and adjacent levels has not been established. If facet joint forces at the treated level change significantly after treatment, it is anticipated that facet degeneration may be accelerated despite the maintenance of segmental mobility. Therefore, it is of interest to determine the effects of disc replacement on antero-posterior load sharing, total facet joint forces, and average and peak facet contact pressures at the treated and adjacent levels.

Methods

Model Parameters

Pursuant to this aim, a set of five additional finite element models has been developed, with disc replacement prostheses placed at the C4/C5 level (Figure 53). All models were based on the "Baseline" (k=0.5) model previously described, which will be referred to in this section as the "Intact" case. The material properties, bony geometry, and disc geometry and structure at the untreated levels were unchanged. The immediate post-operative case was represented using an appropriately sized implant (hereafter, Size 2). Two further models, Size 1 and Size 3, represent the immediate post-operative case with oversized and undersized implants, respectively. These models were developed to investigate the effect of improper implant selection. The long-term response of the off-sized implant models was modeled as well (Size 1 long-term, Size 3 long-term).

For all implant models, the entire C4/C5 disc was resected, and 50% of the anterior longitudinal ligament was removed over the treated level. The ProDisc-C implant endplates are coated with porous titanium to promote bony ongrowth, and successful osteo-integration was modeled with tie constraints at the implant-vertebral body interfaces. The vertebral endplate geometry was altered for congruence with the implant, and keel slot geometry was added. The cobalt-chromium-molybdenum endplates were defined as linearly elastic materials with an elastic modulus of 250 GPa and a Poisson's ratio of 0.29, and the ultra-high molecular weight polyethylene (UHMWPE) puck was represented with an elastic modulus of 1.4 GPa and a Poisson's ratio of 0.3.

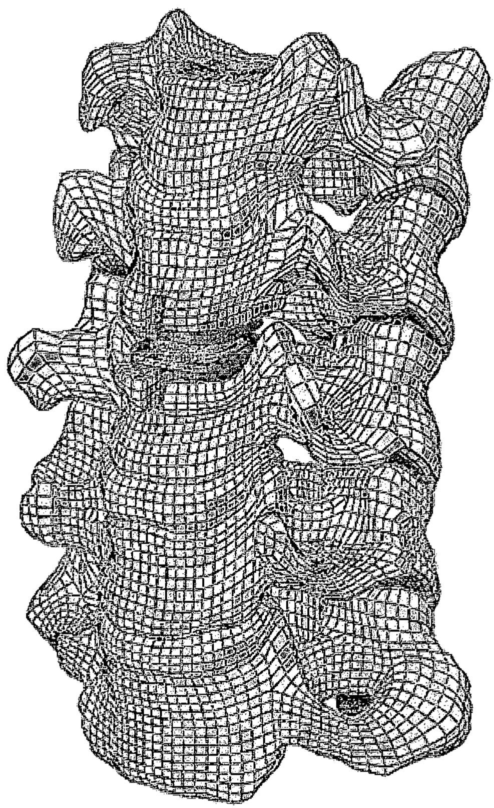

Figure 53 – Size 2 implant model. C4 and C5 endplate geometries were adjusted for implant congruence and keel slots.

Differences between the models were compared with respect to overall kinematics and range of motion, total facet joint contact forces, facet contact areas, mean and peak contact pressures, antero-posterior load sharing and ligament tension.

Implant Size

A set of three models of the ProDisc-C cervical disc replacement implant was developed (Figure 54). The ProDisc-C implant is available in three widths, two depths per width, and three heights. The Size 2 model was based on the most appropriate standard design ProDisc-C implant size for the model geometry, with medium size endplates (15 mm wide x 12 mm deep), and a height of 6 mm. Size 1 and Size 3 also use the same metallic endplates, with off-sized pucks resulting in overall implant heights of 5 and 7 mm, respectively. The implant geometry dictates that the center of rotation is the same for all three sizes, taken with respect to the superior component.

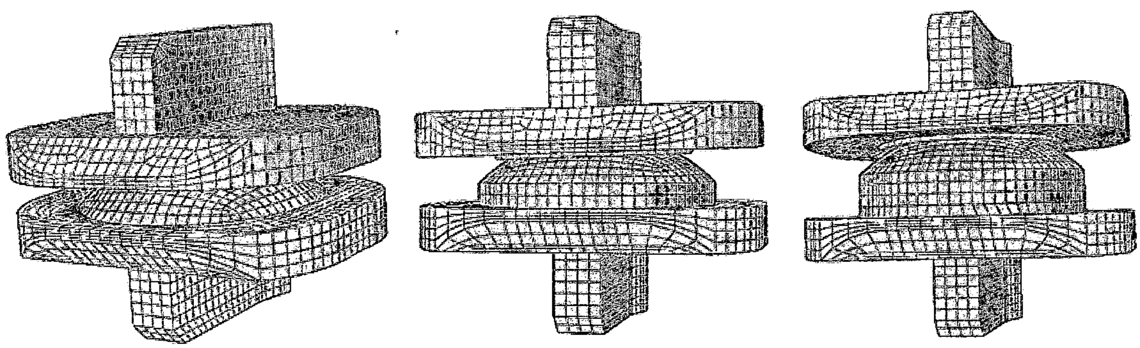

Figure 54 - Size 1, Size 2, and Size 3 ProDisc-C implant models (left to right)

A frictionless finite sliding formulation was used for the implant articulation, and a tie constraint was prescribed between the polyethylene puck and the inferior metallic component. The mesh resolution of the implant models (12,400-14,400 additional nodes, 8,500-10,000 additional elements) exceeds the resolution of the highest-resolution C4/C5 disc model.

The superior and inferior metallic endplates were initially located in the same place for all implant models, and the puck was constrained appropriately to the lower component. This approach resulted in an initial gap in the implant articulation for the undersized models per the height deficiency of the implant, and an initial overclosure in the implant articulation for the oversized implant models per the height excess of the implant. For all three sizes, the immediate post-operative condition was represented by allowing contact to be established as ligament pretensions were enforced.

Long-term Models

The use of an oversized implant results in increased ligament strains in the neutral position for the ALL, PLL, and FCL at the treated level, for which neutral-position tensions were predicted to increase 273%, 109%, and 106% respectively, relative to the Size 2 model (Figure 55). It is possible that in the long-term, biological remodeling processes will reduce the excessive stresses to levels similar to the intact physiological case. In order to investigate the effects of such long-term ligament remodeling, two further models were developed having identical geometry to the Size 1 and Size 3 models.

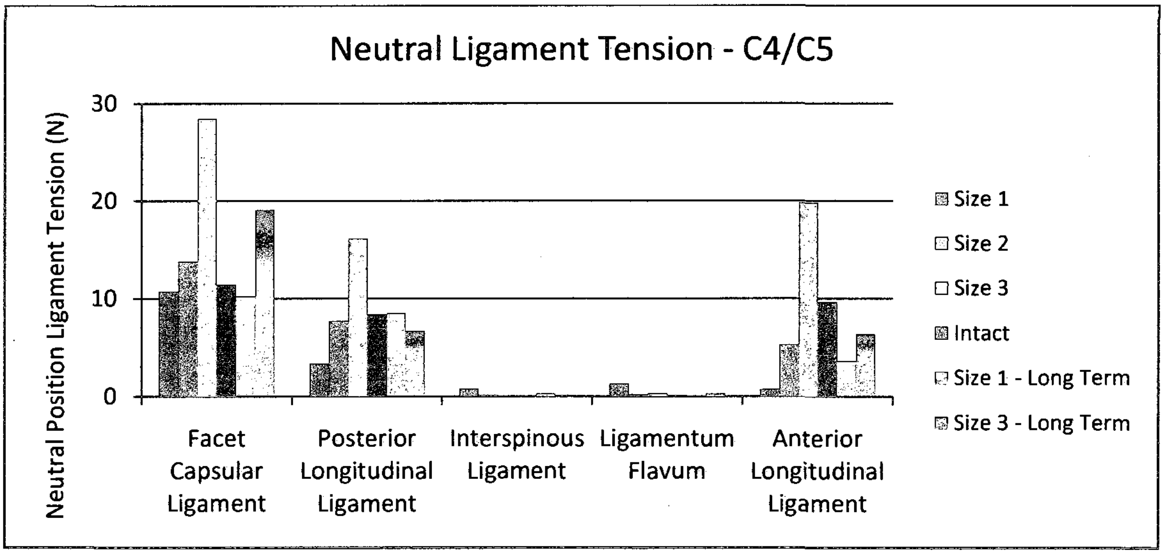

Figure 55 - Long-term model generation. Ligament tension in the neutral position for the long-term models is substantially closer to the intact and Size 2 cases. Intact tension in the ALL is approximately double the Size 2 and long-term cases, as half the ligament was resected.

The ligament elongations and tensions at the treated level in the equilibrium state were measured for the Intact and post-operative implant models. The differences in neutral position ligament elongation between the off-sized and Size 2 models were defined as the excess stretch if positive, or initial laxity if negative. The long-term Size 1 and Size 3 models were then defined by adding the initial stretch or laxity to the tabular displacement values defining the ligaments at the treated level only, effectively altering the intact lengths of the ligaments, as a representation of long-term remodeling.

Results and Discussion

Range of Motion

Disc replacement had little effect on mobility under axial torsion and lateral bending (Figures 56 and 57), where modest increases in compliance were observed. Compliance increased with decreasing implant size at 1 N-m, but increases were minimal, from 2%-11% under lateral bending and 10%-15% under axial torsion.

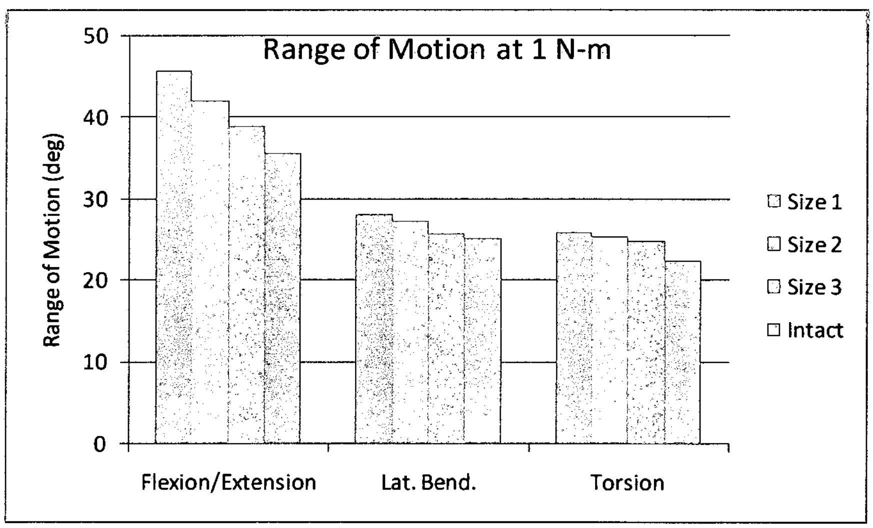

Figure 56 – Post-operative range of motion at 1 N-m. Increased compliance correlates (>0.98) with decreased implant size at 1 N-m.

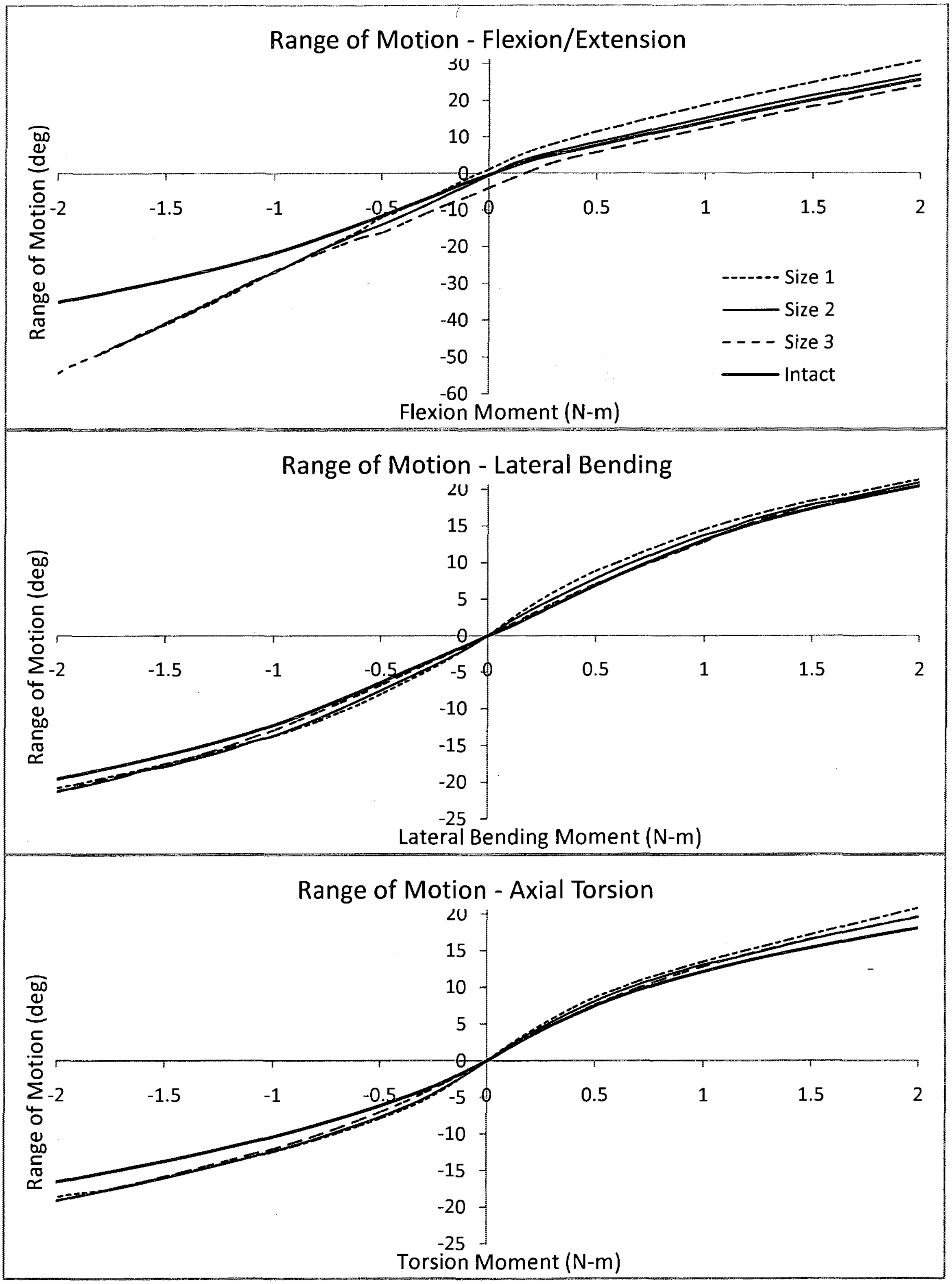

Figure 57 - Implant effects on range of motion. Modest increases in compliance were observed in lateral bending and axial torsion. Implant size had the greatest effect on neutral position lordosis.

Lateral bending and axial torsion range of motion response indicate the effect of shear stiffness of the intervertebral disc, which resists intervertebral axial rotations, whereas the implant does not. This is indicated by the fact that while the *size* of the implant has as strong of an effect on range of motion as its *presence* under lateral bending, the same is not true under axial torsion. The effect is greater at a higher moment (±2 N-m), where the effect of implant size on range of motion under axial torsion (±0.5°) is much less than the effect of implant *presence* : an increase of 4.5°(Figure 57). Under forward flexion, the Size 2 implant was negligibly different from the intact case.

Implant size had the greatest effect under flexion/extension, where the neutral lordosis was increased 4° and decreased 1° by the Size 3 and Size 1 implants, respectively. Under extension, all implant models exhibited substantial increases in compliance. All implant models are identical under extension after implant disarticulation, which occurs at 0.5, 0.8, and 1.1 N-m extension moments for the Size 1, Size 2, and Size 3 implants, respectively(Figure 58).

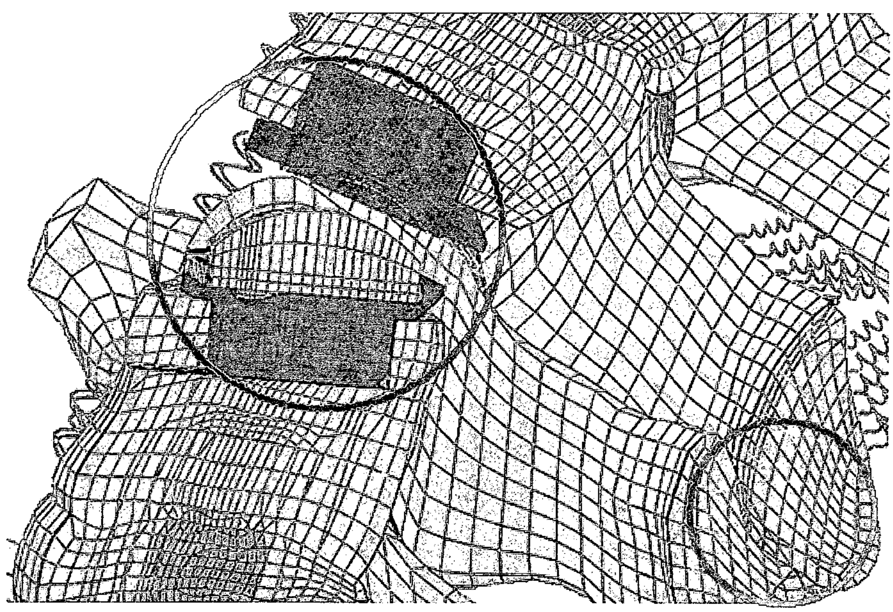

Figure 58 - Implant disarticulation and impingement of the spinous processes in extension.

The slope discontinuity corresponding to implant disarticulation in each case is indicative of the axial tension stiffness of the annulus fibrosus, which is not represented by the implant models. Correspondence with implant disarticulation and facet joint separation is aparrent (Figure 59).

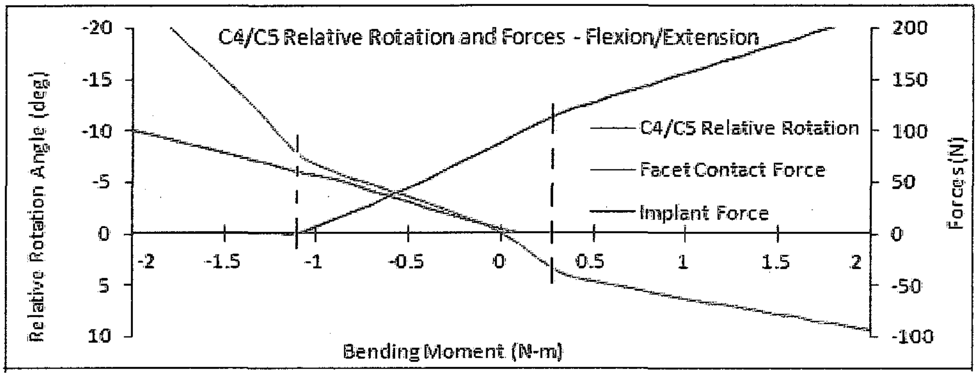

Figure 59 – Discontinuities in compliance at the C4/C5 level with the Size 3 implant correspond with implant disarticulation and facet joint disarticulation (dashed lines). Similar behavior is observed with the Size 1 and Size 2 implant models.

Additionally, interactions between the posterior spinous processes, which would limit extension rotation were not represented in the models, and such interactions are predicted to occur under physiologic loads (Figure 58). As this substantial increase in compliance and massive disarticulation is not observed clinically, it is likely that the lateral aspects of the interverteral disc in the uncinate region are not fully resected clinically. The single-element representation of the facet capsular ligaments may also play a role, as unrealistic shear translations in the zygophageal joints at the treated level is observed secondary to implant disarticulation, a deformation mode that is insufficiently resisted by the single-element representation of the facet capsular ligament.

Coupled rotations following disc replacement followed the primary rotations, with modest increases in range of motion, and marginal effects on coupled rotation fractions (not shown).

Facet Joint Forces

Figures 60-62 present facet joint contact force predictions at each level. Left and right sides are averaged for flexion/extension data. Results for lateral bending and axial torsion are symmetrized for clarity; i.e., force at 1 N-m is the average of the force on the left facet at 1 N-m to the left and the force on the right facet at 1 N-m to the right (Equation 3).

$$F_{symm}(x) = \frac{1}{2}\left(F_{Left}(x) + F_{Right}(-x)\right)$$
$$where\ x = Signed\ Bending\ Moment$$

Equation 3 – Symmetric averaging for facet contact parameters.

Facet contact forces superior to the treated level were not significantly affected by the size or presence of the implant (Figure 60). The maximum change from the intact case at peak load was 3%, occurring under lateral bending where the bilateral deviation (the difference between left and right facets) was 12%. Facet force transmission inferior to the treated level exhibited more sensitivity to implant presence (Figure 62). While differences with repsect to implant size were again negligible, marginal increases with decreasing implant size were observed in all cases. The only relvant differences were observed under flexion, where decreases in force transmission up to 30% were observed. Substantial deviation from the intact case was only observed secondary to implant disarticulation, and is correlated with reduced intervertebral relative rotations inferior to the implant. It is likely that such differences are exagerrated, per the model limitations discussed previously.

Facet contact forces at the treated level were substantially more sensitive to implant size (Figure 61). Under all load cases, with the exception of extension secondary to implant disarticulation, facet contact forces at the treated level correlated inversely with implant size. Under all low-side moments (i.e., positive flexion and negative signed lateral bending and axial torsion momens), force increases of approximately 15-20 N were observed with the Size 1 implant. The correctly sized implant is within the bilateral range of the intact case for all but axial torsion.

The 25% increase in force transmission under axial torsion with the Size 2 implant is commensurate with a 15% increase in relative rotation at the implanted level (Figures 61 and 71). Differences between post-operative and long-term conditions on facet contact forces were negligible, indicating that geometry, rather than ligament tension, are chiefly responsible for the facet contact forces.

The maximum increase in facet contact force with the Size 2 implant over the intact case was 13 N under axial torsion, from 49 N to 62 N. However, the increased force remains within 9% of the peak intact force under lateral bending (57 N) and is well within the range of intact forces under extension, which are as high as 90 N. These results indicate that the changes in contact forces with the Size 2 implant are unlikely to contribute significantly to subsequent degeneration of the facet cartilage. Results for the Size 3 implant are even more positive, as Size 3 facet forces are less than Size 2 forces. For the smaller Size 1 implant, the results are more mixed. While the greatest increases are observed at the C4/C5 level under lateral bending (21 N, or 37%), this is still within the range of forces under intact extension. This would indicate that the increased forces with the Size 1 implant are also unlikely to induce degeneration. However, this interpretation should be tempered by the observation that consistently higher forces are observed with the undersized implant under all load cases, and neutral position forces are increased 190%. The consistently increased loads, particularly in the neutral position, may be more likely to contribute to degeneration.

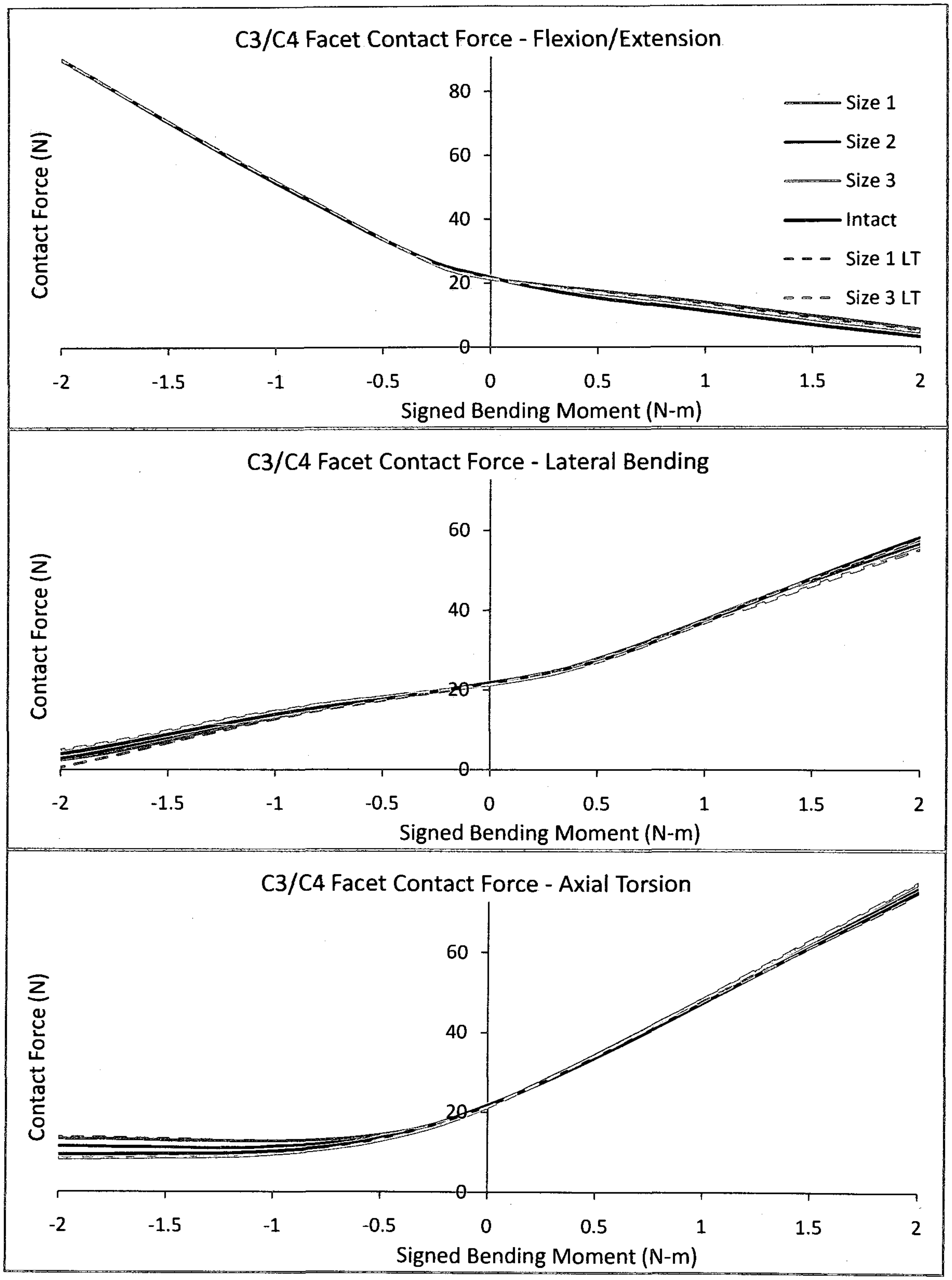

Figure 60 - Facet contact forces superior to treated level exhibit negligible change post-operatively.

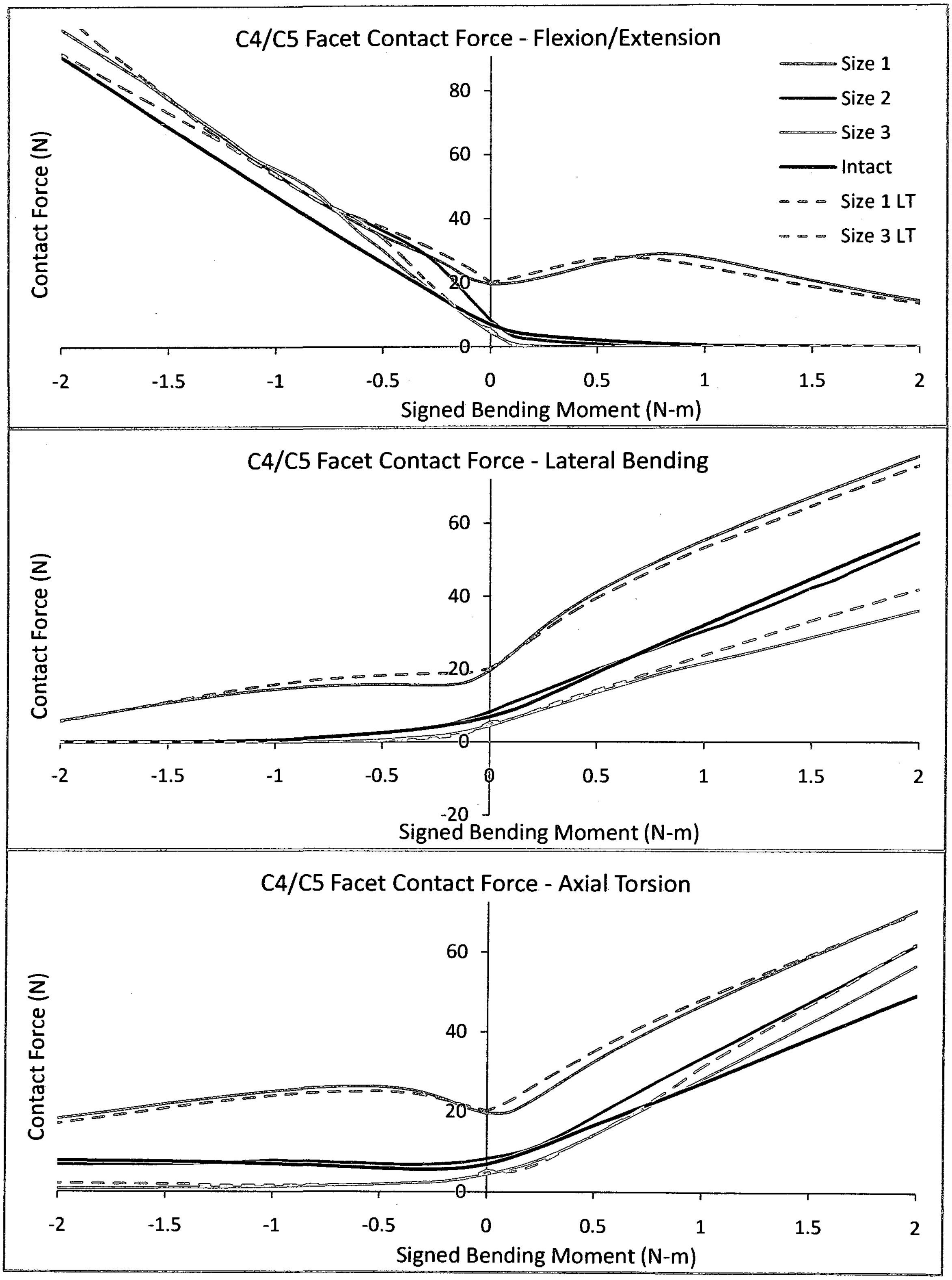

Figure 61 - Facet contact forces at the treated level are affected by implant size and to not return to intact levels long-term.

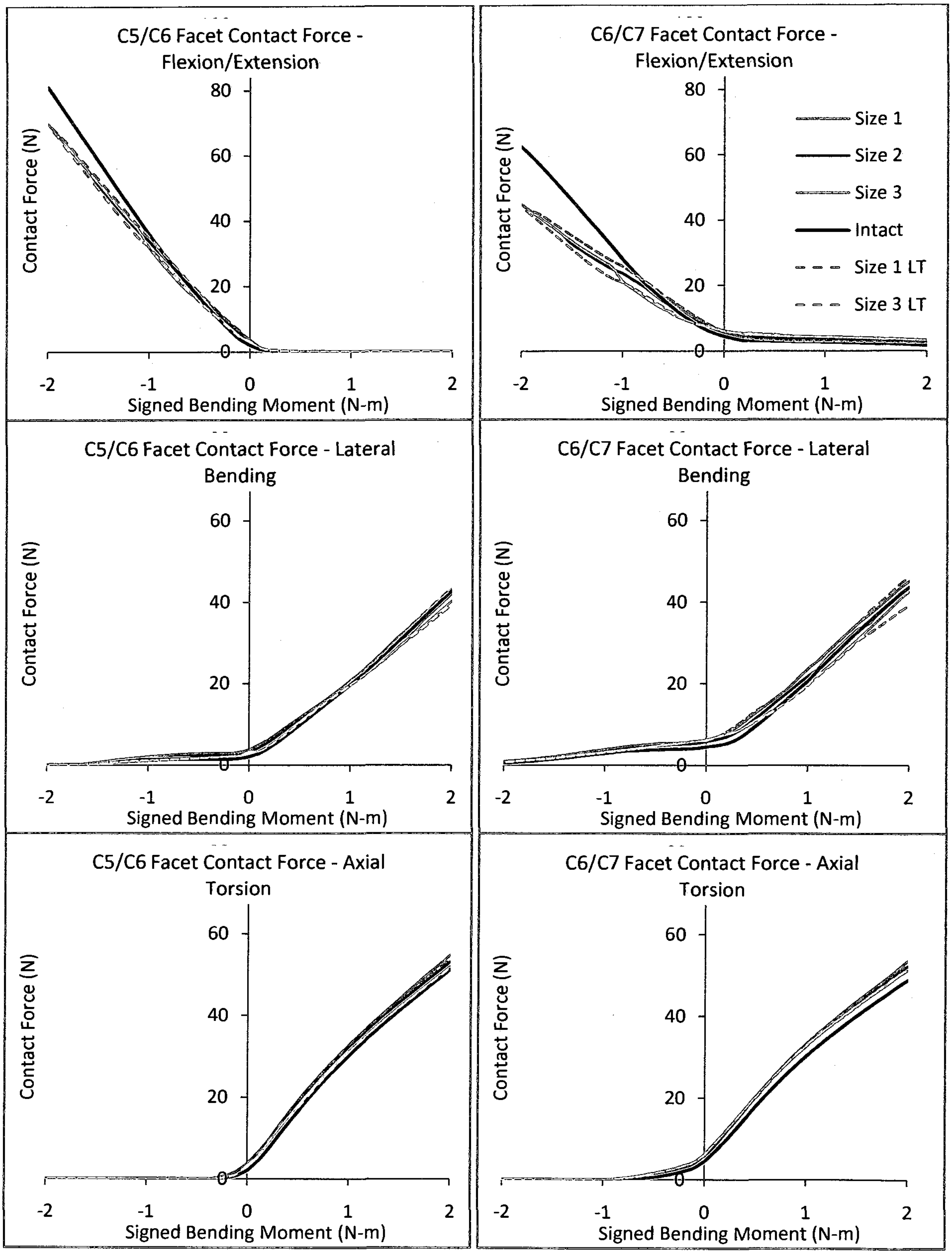

Figure 62 - Facet contact forces inferior to the treated level.

Implant Load Transmission

Forces transmitted through the implant were strongly affected by implant size in the short-term, increasing 75% and decreasing 50% in the neutral position relative to the Size 2 implant, when the Size 3 and Size 1 implants were examined, respectively (Figure 63). In the long-term, however, differences in force transmission between Size 3 and Size 2 implants were reduced 60%-90% by relaxation of the ligaments. Post-operative implant force transmission with the Size 1 implant, which was as much as 75% lower than the Size 2, did increase in the long term, but differences were only reduced 25%-50%. This difference in long-term behavior between the large and small implant sizes is attributable to the load carriage in the facet joints with the smaller implant (Figure 61).

Nuclear Pressure

Adjacent-level nuclear pressures were negligibly affected by the presence or size of the implant (Figure 64). Mean pressure at the inferior adjacent level was reduced 10% under peak extension for all implant models, commensurate with the reduced relative rotation at that FSU. However, the reduced values are still well within the predicted and experimentally observed distributions.

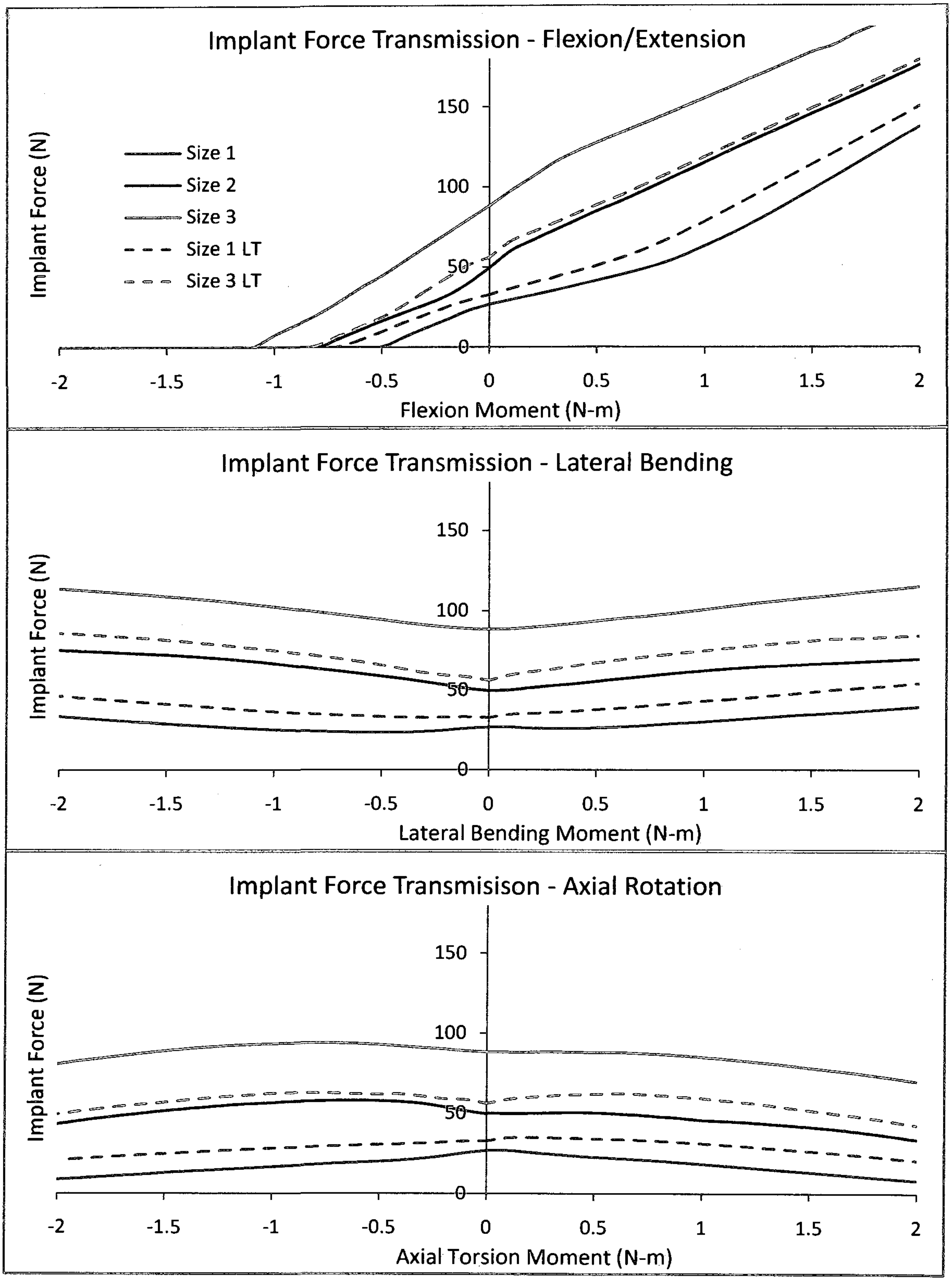

Figure 63 - Implant load transmission. Effect of implant size is apparent.

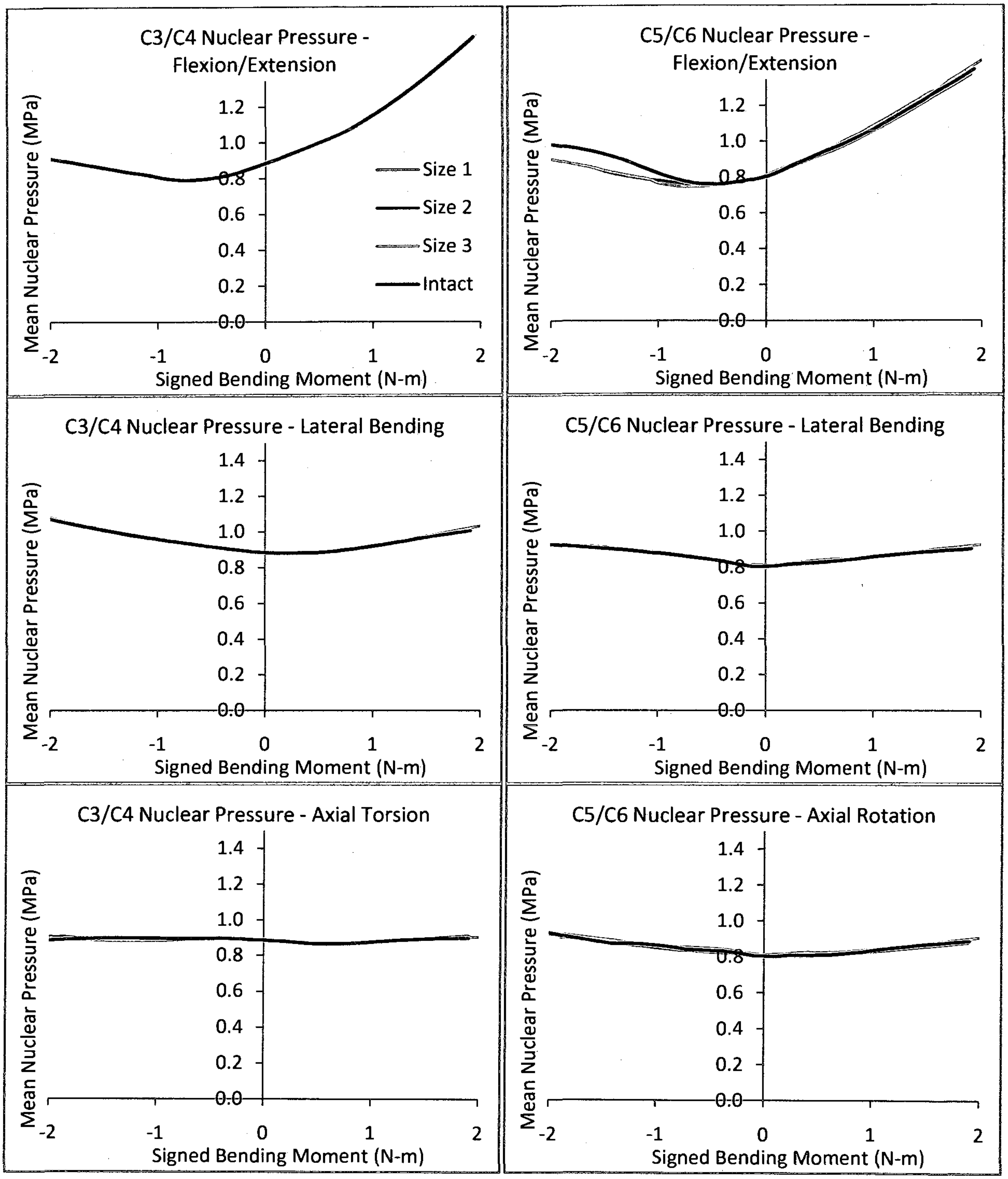

Figure 64 – Adjacent-level nuclear pressures were mainly unaffected by the implant. Reduced pressure at the inferior disc under extension is commensurate with reduced relative rotation.

Ligament Tension

Figure 55 presents model predictions of tension in each ligament at the treated level in the neutral position. Post-operative tensions in the ALL, PLL and FCL are increased 273%, 109%, and 106% respectively, relative to the Size 2 levels with the oversized implant, and tension in the ISL is lost entirely. These excess tensions are reduced 92%, 88%, and 64% respectively in the long-term, and the neutral tension in the ISL is restored to 83% of the intact value. With the Size 1 implant, increases in neutral tension in the ISL and LF of 323% and 433% are observed post-operatively, which are reduced by 76% and 83% respectively, in the long-term. The ALL and PLL exhibit laxity with the undersized implant resulting in 86% and 57% reductions in neutral tension respectively, but these losses are restored in the long term.

For the ALL, long-term and Size 2 *elongations* are near the intact, but *tensions* remain at approximately half the intact value. This is due to the representation of the post-operative ALL using 50% resection.

Figures 65-69 present ligament tension results at the C4/C5 level. For the anterior longitudinal ligament, the additional dashed black line represents half the tension in the intact case so that the implant models may be more meaningfully compared, as 50% of the ligament was resected in all implant models (Figure 65). Under flexion, and under extension preceding implant disarticulation, the Size 2 and long-term models follow half the intact tension. In the post-operative case, the Size 3 ALL tension is maintained under flexion. Under lateral bending and axial torsion, peak ALL forces are not as high as those observed under extension, as anticipated. Both long-term models predict negligible effects of implant size on ALL tension under lateral and axial moments, and the excess initial tension in the post-operative oversized implant model is maintained.

The posterior longitudinal ligament exhibits similar long-term behavior to the ALL, with post-operative effects of implant size drastically diminished in the long-term under all load cases (Figure 66). Under extension secondary to disarticulation, changes in tension are observed. As with the ALL, the initial over- or under-distraction of the disc space results in changes in neutral position tension of ±10 N. While lateral bending and axial torsion response for the Size 2 implant approximate the intact, larger differences are observed under flexion/extension. The increased slope of the Force-Moment curves under flexion results in an increase in peak PLL tension of 13 N in the long-term, and is indicative of the drastically increased compressive stiffness of the implant relative to the intact disc. The magnitude of the increase in PLL tension under flexion would be sensitive to the antero-posterior placement of the implant, vis-à-vis changes in the center of rotation.

Tension in the interspinous ligament was negligible under all but flexion loads, as expected (Figure 67). The interspinous ligament was less sensitive to implant size, with changes in peak force of 5.7 N and -2.0 N post-operatively with the Size 1 and 3 implants, respectively.

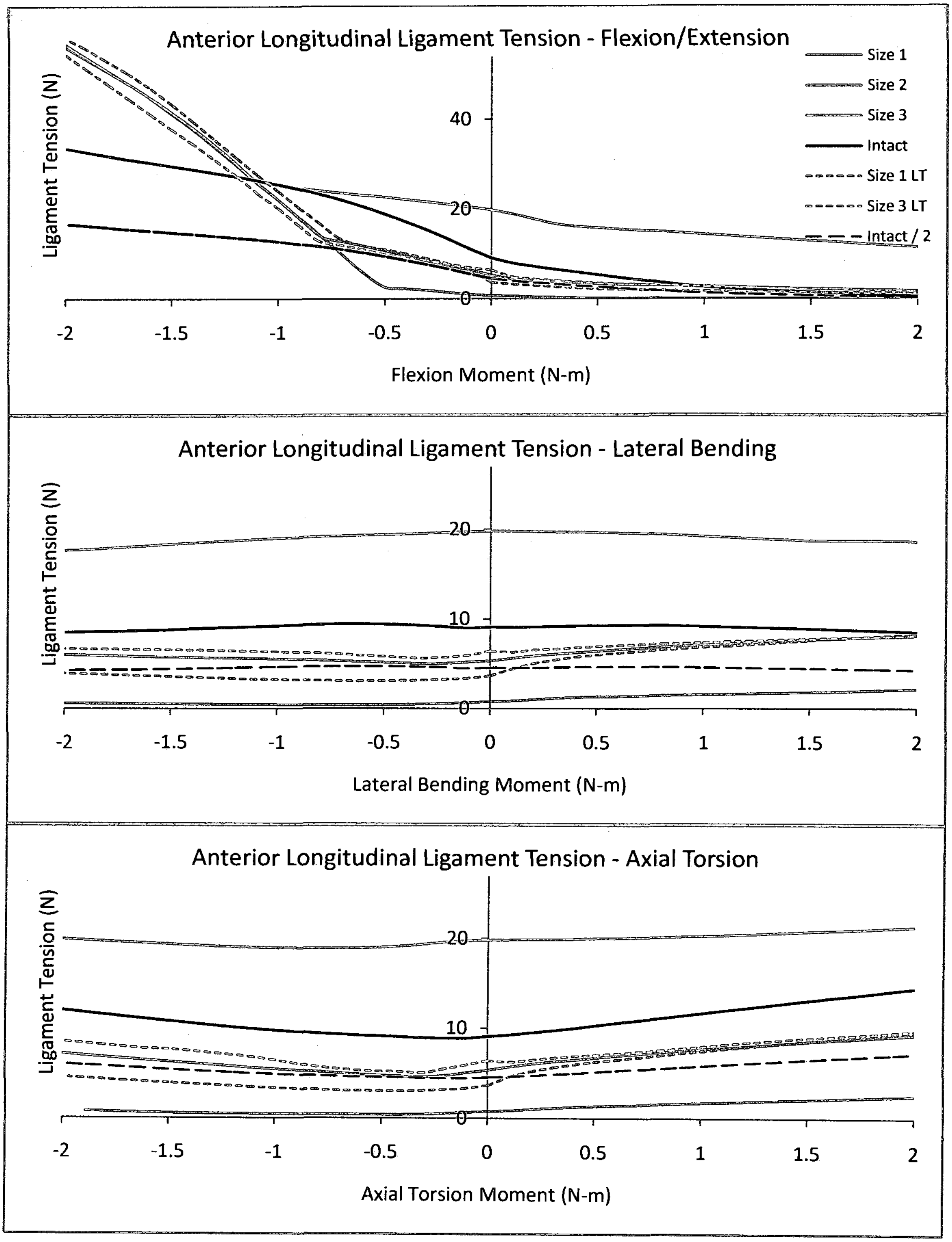

Figure 65 - Anterior Longitudinal Ligament tension.

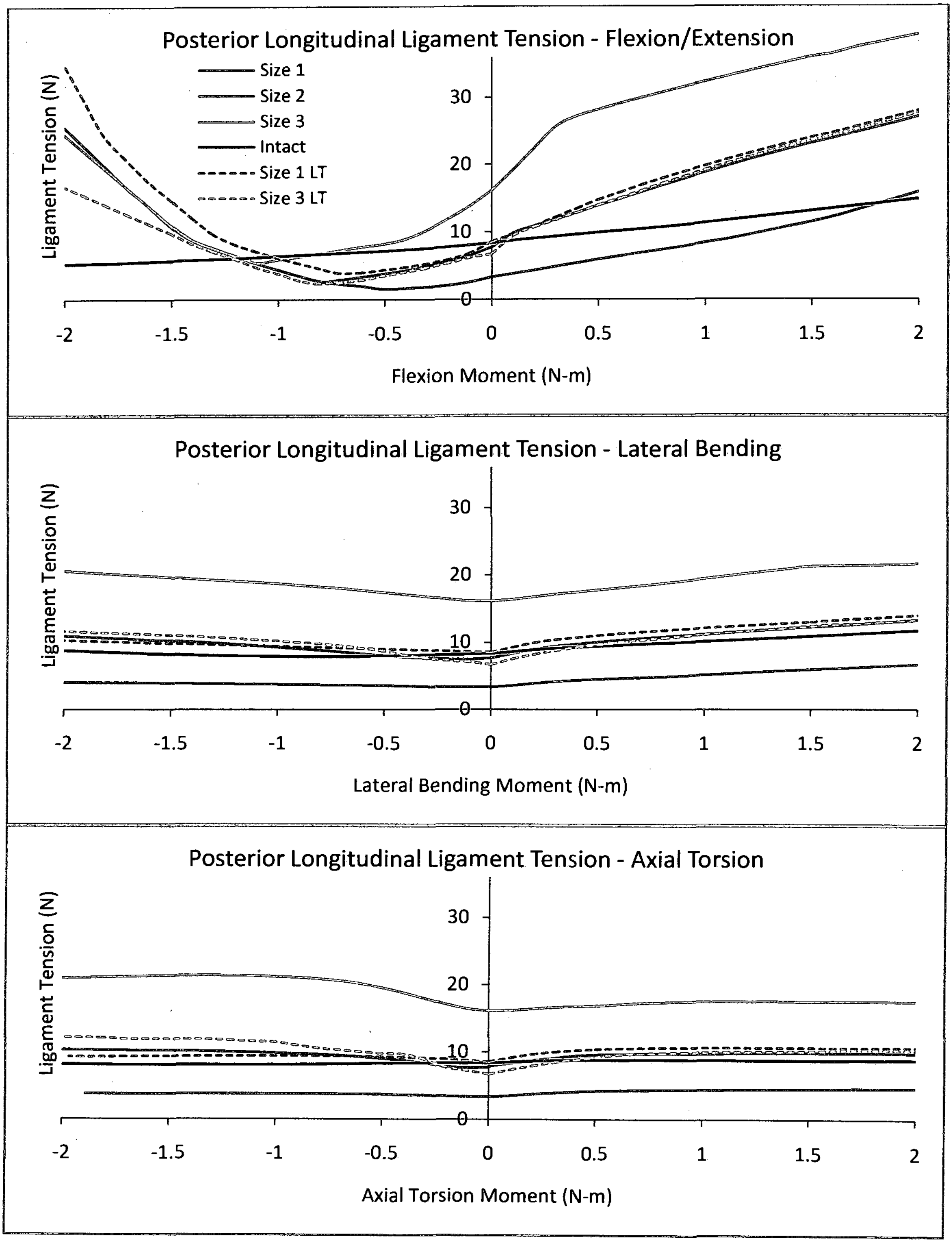

Figure 66 - Posterior Longitudinal Ligament Tension.

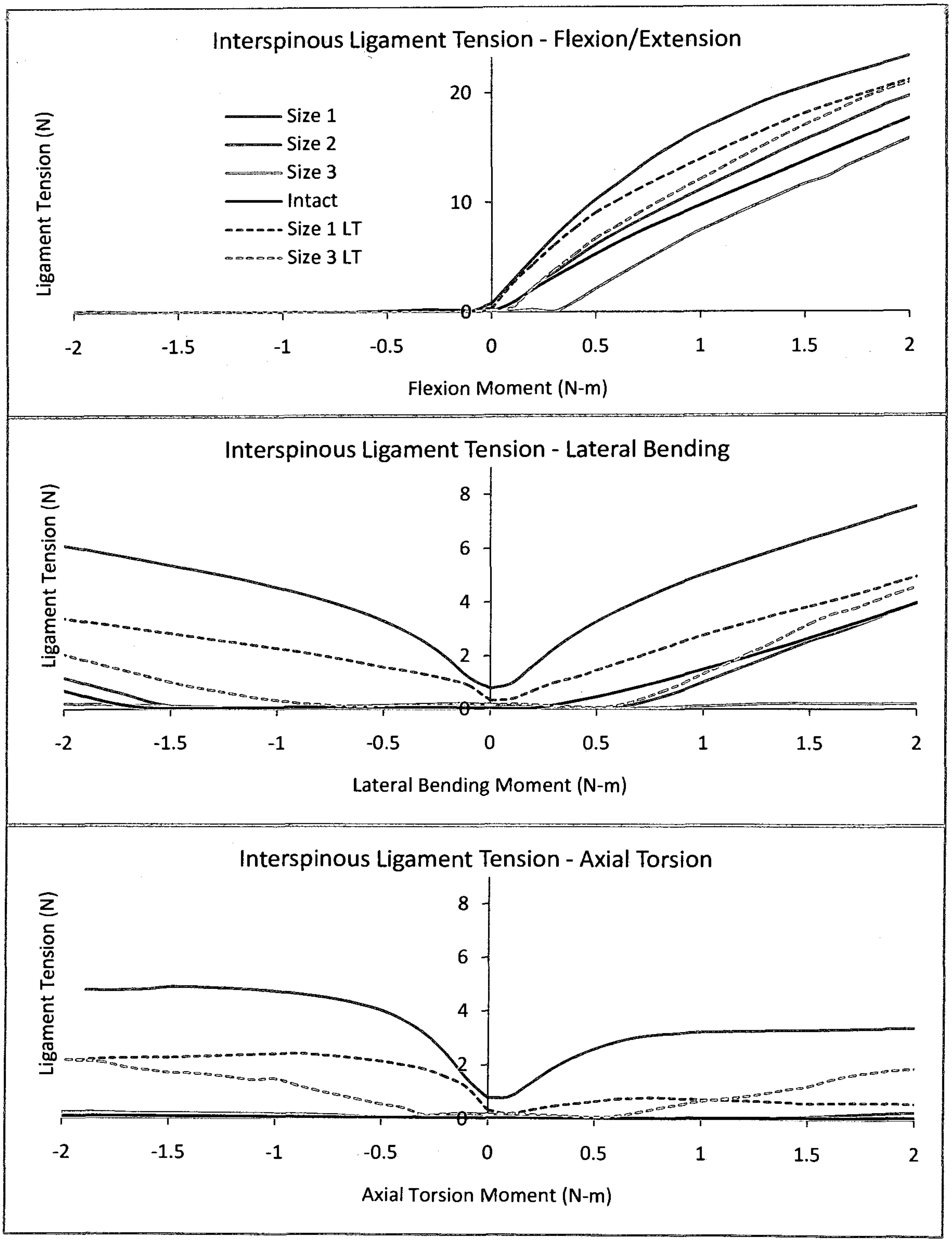

Figure 67 - Interspinous Ligament Tension.

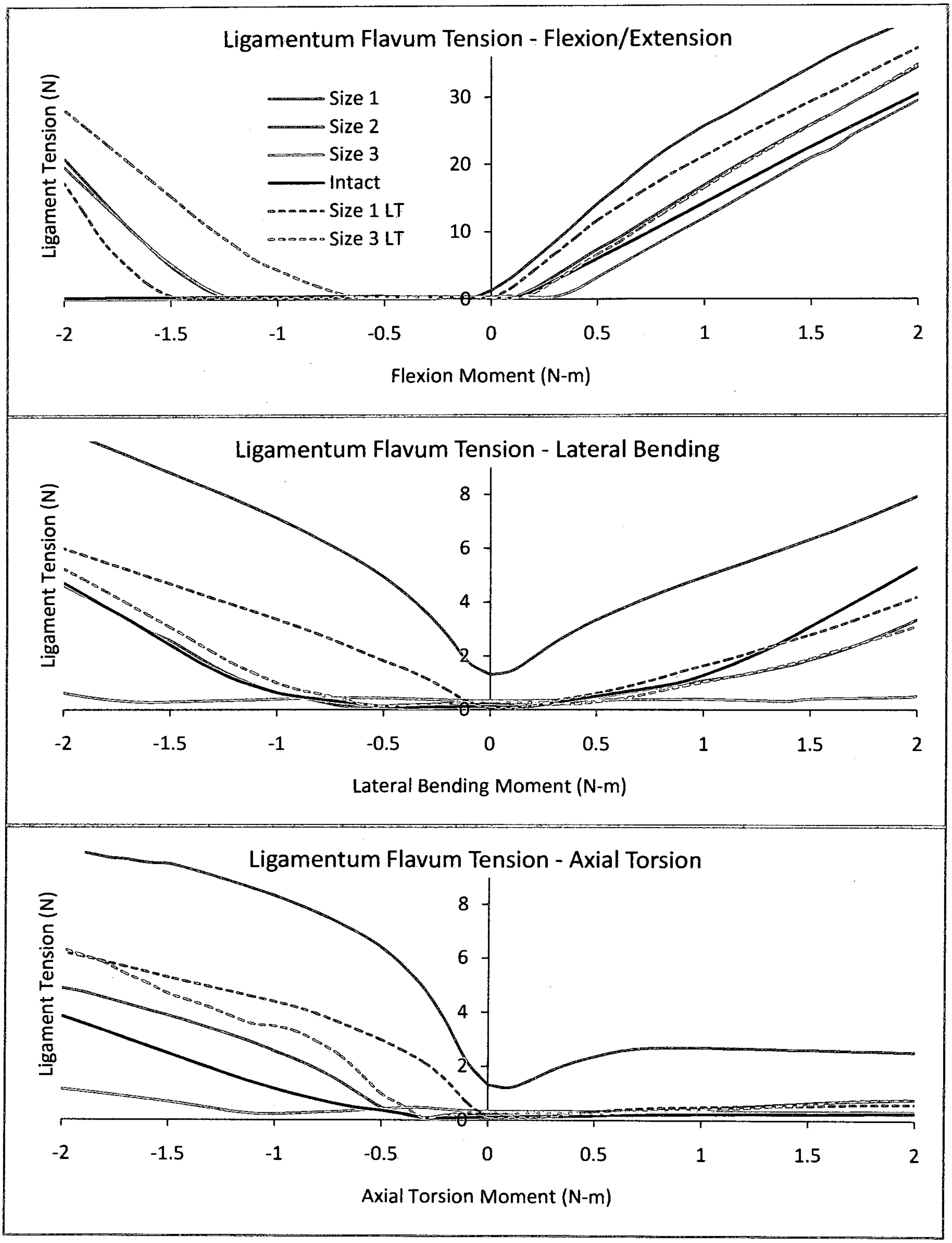

Figure 68 - Ligamentum Flavum Tension.

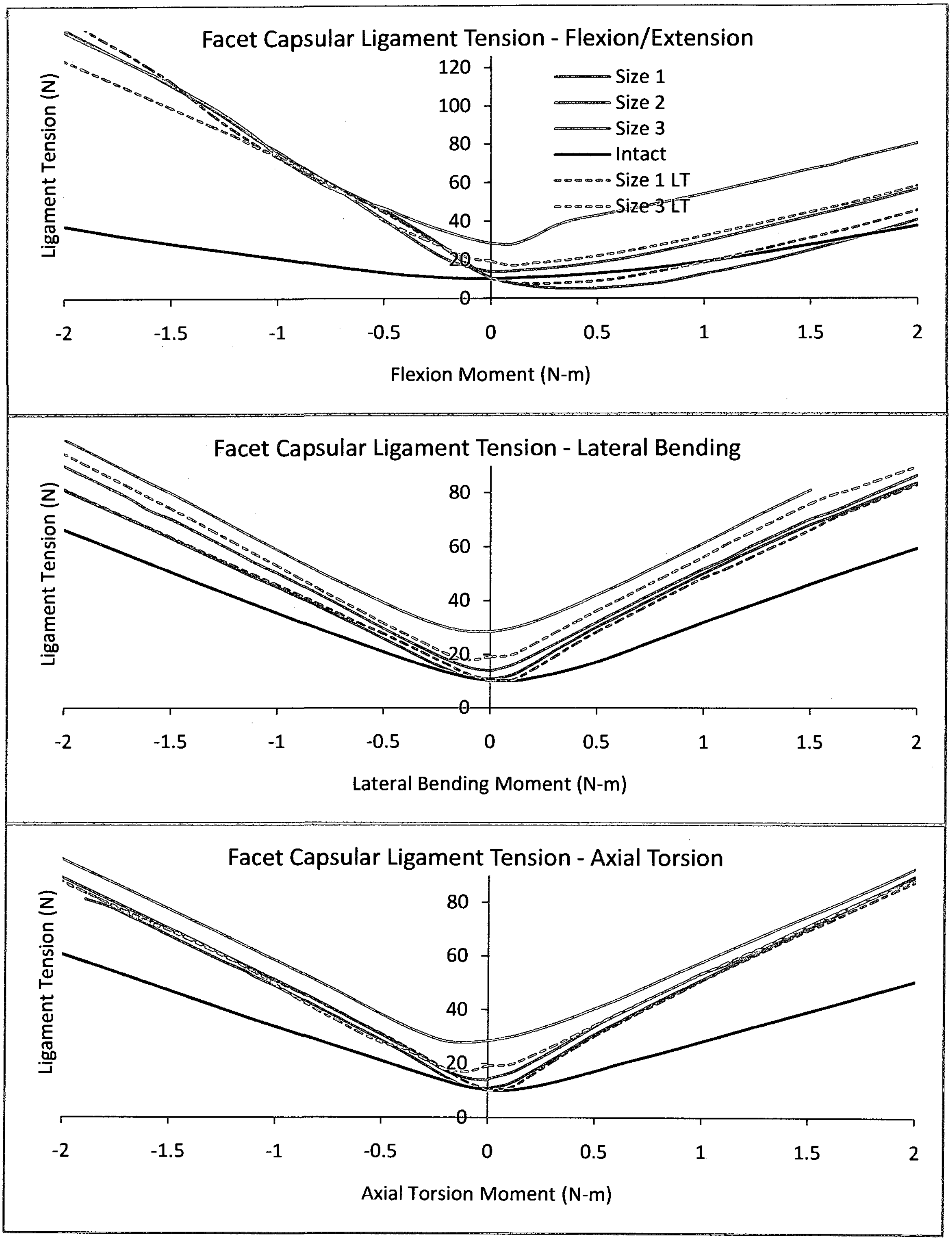

Figure 69 - Facet Capsular Ligament Tension. Left and right sides summed.

As expected, the ligamentum flavum exhibited similar response to implant size as the interspinous ligament (Figure 68). Post-operatively, peak forces in the ligamentum flavum were 37% higher than the intact case, but were within22% in the long-term.

The facet capsular ligaments play a more significant role under lateral bending and axial torsion than under flexion/extension in the intact case (Figure 69). Effects of implant size were weak under lateral and axial loads, and the differences were further reduced in the long-term. Both the Size 1 and Size 2 implants exhibited facet contact in the neutral position at the C4/C5 level, with the result that the short- and long-term Size 1 models are not substantially different. Peak facet capsular ligament forces with the Size 2 implant were increased 45% under lateral bending and 72% under axial torsion, which is likely indicative of the negligible rotational and bending stiffness of the implant. The increase in ligament tension under flexion is related to the antero-posterior implant placement, as with the PLL. Under extension, the facet capsular ligament provides a greatly increased fraction of the total restorative moment at the treated level, carrying 80% of the anterior ligamentous load fraction at 1 N-m extension.

Intervertebral Relative Rotations

Intervertebral relative rotations superior to the implant increased 74%, 47%, and 77% after implantation with the Size 2 implant under flexion/extension, lateral bending, and axial torsion, respectively (Figure 70). The effect of implant size was negligible. At the treated level, differences under lateral bending and flexion were negligible, but increased mobility was observed under extension and axial torsion (Figure 71).

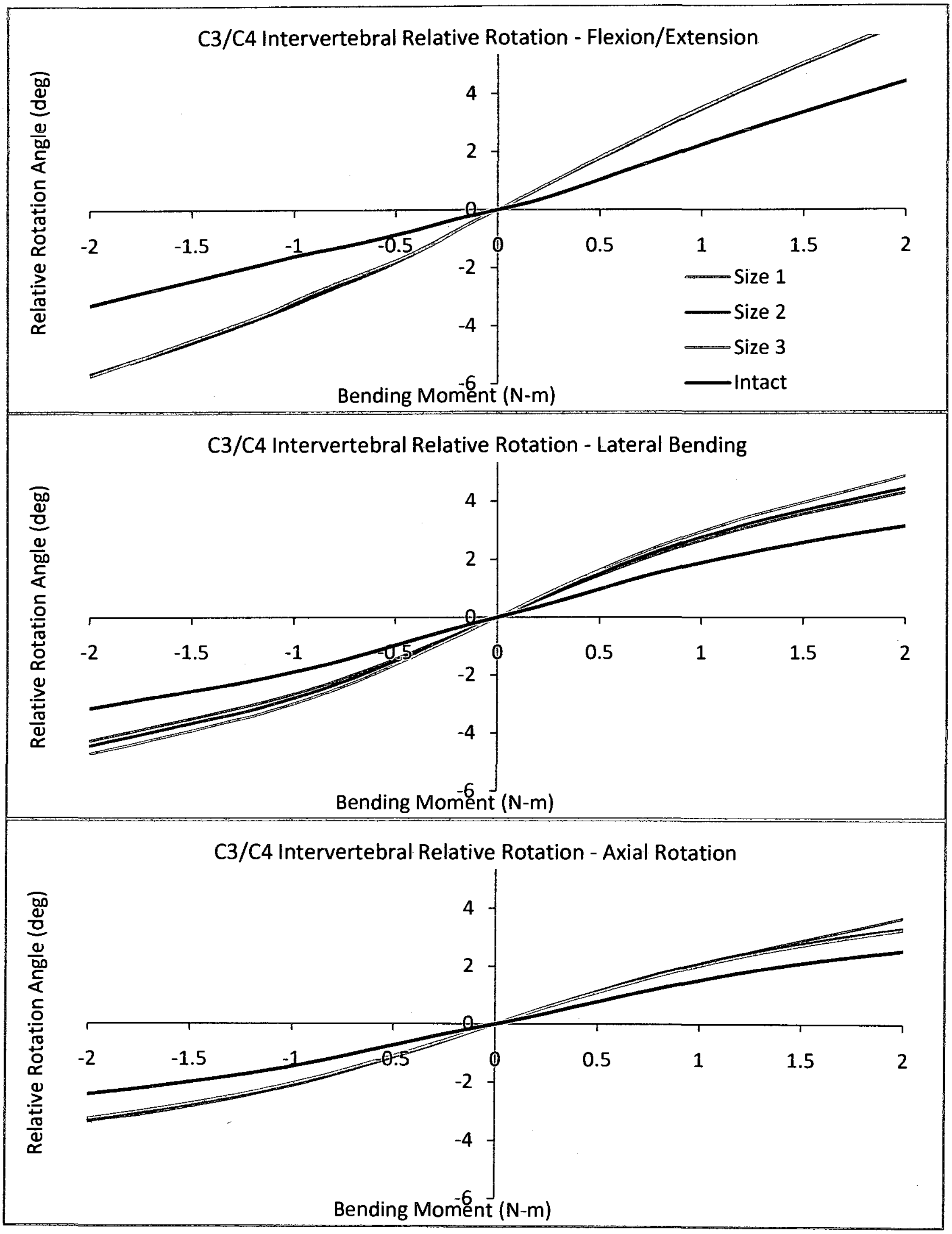

Figure 70 - Relative Rotation Angles superior to implant.

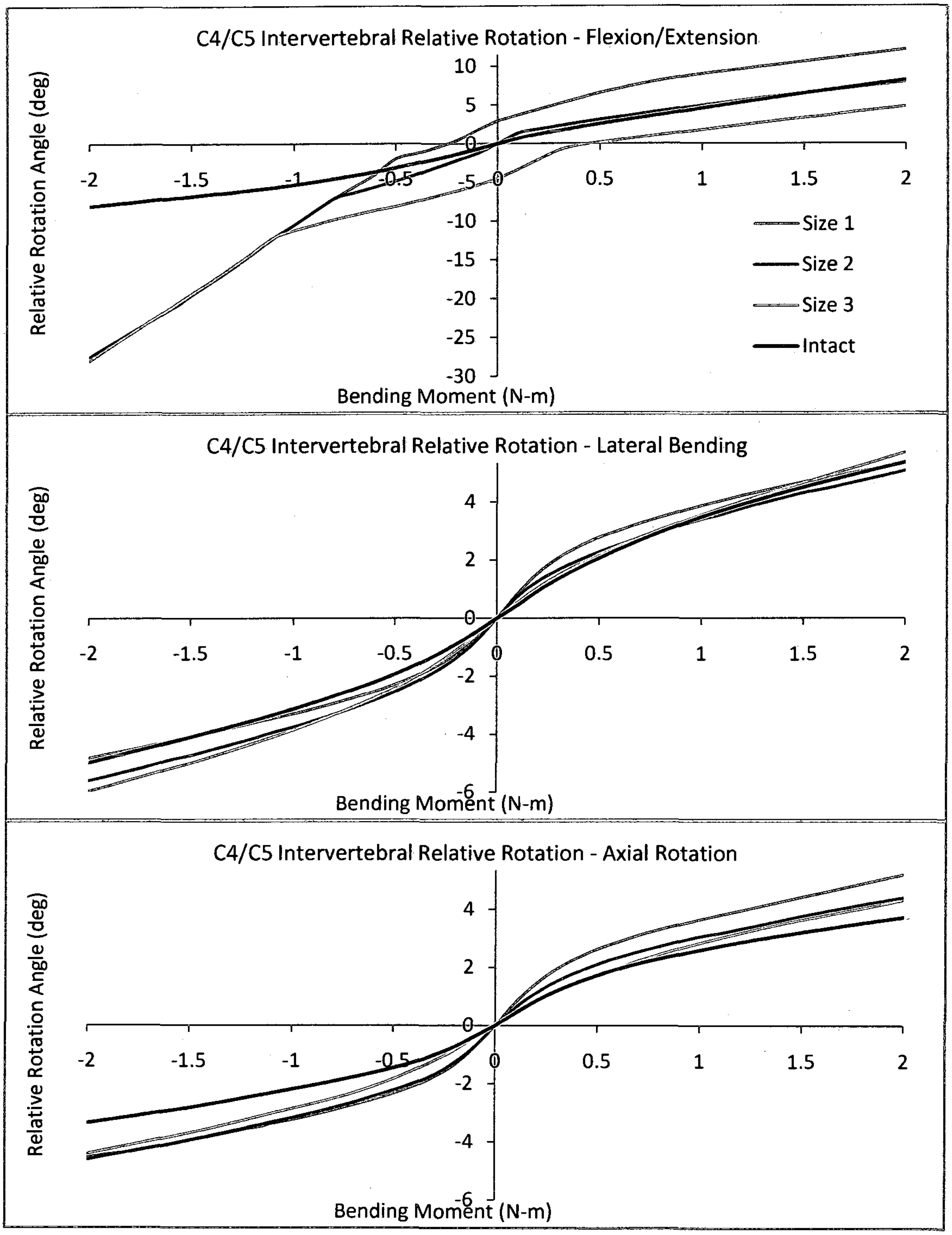

Figure 71 - Relative Rotation Angles at implant level.

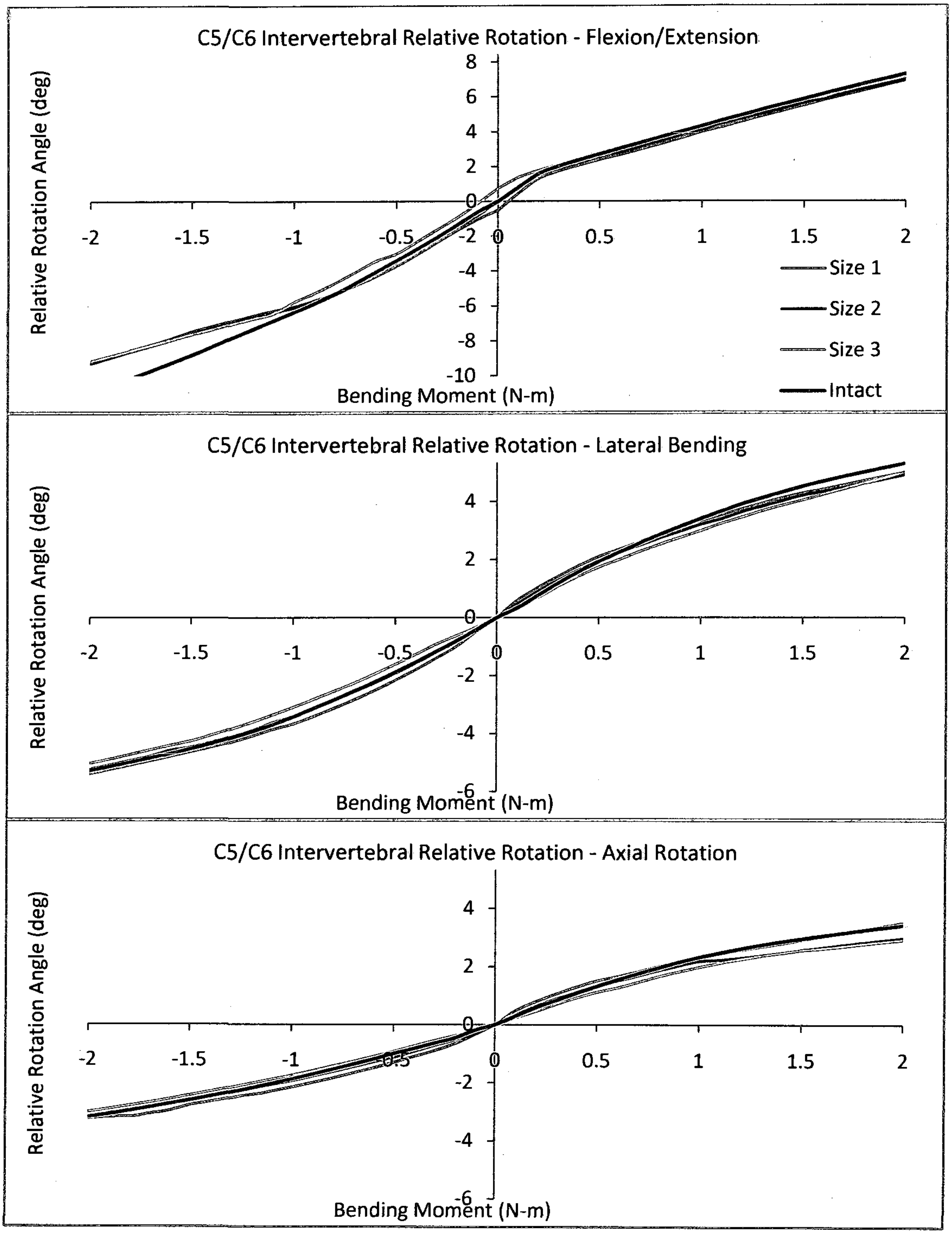

Figure 72 - Relative Rotation Angles inferior to implant level.

Under extension, compliance at the implanted level increases 100% subsequent to implant disarticulation, from 8.6 deg/N-m to 17.3 deg/N-m for the Size 2 implant. In the neutral position, 3° ventral and 4.5° dorsal relative rotations are induced at C4/C5 post-operatively with the Size 1 and Size 3 implants, respectively. These initial rotations are maintained throughout flexion.

Inferior to the treated level, modest *decreases* in range of motion were observed under all load orientations at both C5/C6 and C6/C7 (Figure 72, previous page). Under lateral bending and axial torsion, marginally greater range of motion corresponded with decreasing implant size. The neutral position sagittal-plane rotations observed at the treated level are partially offset by opposing rotations at the C5/C6 and C6/C7 levels totaling ±1.5°. Range of motion caudal to the treated level under lateral bending, axial torsion, flexion and extension previous to implant disarticulation are within 6% of the intact disc values.

Conclusions

As stated previously, changes in sagittal alignment and spinal loading after ACDF have been associated with adjacent-segment degeneration and other adverse affects, but it has been unclear as yet whether the same relationship exists when mobility is maintained [62, 99, 102]. Various clinical studies have reported changes in sagittal alignment after disc arthroplasty that were *not* correlated with loss of ROM, increased pain, or negative outcomes [25, 99, 111, 118]. Again, preliminary and long-term results following implantation of the Prestige I & II showed positive outcomes and maintenance of mobility with no evidence of adjacent-level degeneration [102, 111]. The results obtained in this study may shed some light on the mechanisms by which these results have been obtained.

Range of motion results for the C3-C7 segment support the reported clinical outcome of ROM maintenance following arthroplasty, and no deleterious effect of implant size selection was observed. Individual level relative rotations reveal no loss of mobility at the treated or superior levels, and mobility inferior to the treated level is within 95% of the intact case at 1 N-m, regardless of implant size.

Facet joint contact forces adjacent to the arthroplasty are not increased more than 10% under any load case examined, regardless of implant size, indicating that adjacent-level cartilage degeneration is not expected to be aggravated by arthroplasty. Facet joint forces at the treated level remain within the physiologic range with appropriately- and over-sized implants, a positive indication for the use of arthroplasty. Contact forces are increased substantially when an undersized implant is used however, and are not reduced in the long-term, indicating that appropriate implant size selection may be important for prevention of cartilage degeneration at the arthroplasty level subsequent to implantation. Facet joint congruence was not affected by implant size within the range examined, and contact pressures follow contact forces.

Implant forces were strongly affected by implant size, and were increased 75% in the neutral position with the larger implant model, indicating that ligament tension is a primary factor in implant loads. This hypothesis is further supported by the return to Size 2 implant loads in the long-term Size 3 model. The early onset of implant disarticulation in extension with the Size 1 implant would indicate the use of larger implants, but the long-term models predict similar disarticulation moments.

Adjacent-level nuclear pressures, like adjacent-level facet joint forces, are not predicted to be strongly affected by arthroplasty, indicating that adjacent-level disc degeneration secondary to arthroplasty is primarily due to pre-existing degenerative processes rather than the arthroplasty.

Tension predictions in the interspinous ligament and ligamentum flavum indicate that no injury to these ligaments is anticipated following arthroplasty. Loads carried by the facet capsular ligament, however, are increased substantially both post-operatively and long-term, indicating the loss of motion-segment stability provided by the annulus fibrosus. These results, in addition to implant disarticulation under extension and hyper-mobility under extension and axial torsion, indicated that full resection of the disc is not optimal. Specifically, the lateral aspects of the annulus fibrosus should be maintained surgically, as these regions provide the most mechanical stability under lateral and axial loads. Additionally, problematic disc bulge requiring resection is more likely in the central posterior region of the disc.

While post-operative loads in the ALL are increased with the Size 3 implant, long-term relaxation in the ligament predicts a return to physiologic loads, except after implant disarticulation in extension. Loads in the PLL under flexion remain higher than intact loads even in the long-term, due to the stiffer compressive behavior of the implant relative to the pliant disc. However, if these increased loads result in further relaxation, the flexion tension in the PLL would be reduced. Additionally, the peak elongations in the PLL under flexion are not sufficiently high to result in likely injury, even with the Size 3 implant.

Clinical Implications

Overall, the finite element models presented provide support for the use of cervical arthroplasty as a superior treatment option to anterior cervical discectomy and fusion. Adjacent-level disc degeneration is not predicted to be aggravated by arthroplasty, nor is adjacent-level cartilage degeneration. At the treated level, appropriate implant selection may be important, with oversized implants increasing ligament tensions post-operatively, and undersized implants increasing facet contact forces immediately and long-term. As the latter is a more clinically relevant problem, the particular avoidance of undersized implants may be indicated.

Certain surgical protocols are indicated by this research as well. Full resection of the disc and ALL results in hyper-mobility and increased cartilage pressures and ligament tensions, and possibly implant disarticulation, which carries the serious risk of dislodgement. It is therefore advisable to leave as much of the lateral aspects of the annulus fibrosus and the ALL *in situ* as possible.

Implant size selection, as represented in this work, is a function of the degree of cervical distraction applied during surgery. The Size 2 implant model was sized such that the pre-operative joint space was maintained. However, increased implant height reduces the risk of dislodgement and reduces facet contact forces, but increases the force through the anterior bodies and some ligament stresses. Further study of the relationship between distraction force, implant selection, and clinical outcome is indicated.

Summary

In short, the results of the intact and post-operative and long-term implant models indicate that:

- Facet contact force, intervertebral relative rotation and nuclear pressure predictions provide no indication for expectation of adjacent-level degeneration following disc replacement.
- Facet contact force and pressure at the treated level increase following disc replacement if the implant is too small.
- Stresses in the ALL and PLL increase post-operatively if the implant is too large, but may be reduced in the long-term by biological remodeling processes.

- Results indicate that the lateral aspects of the annulus fibrosus should be left intact during disc replacement surgery if possible, to reduce stresses on the FCL and to increase segmental stability.

Future Work

Several aspects of this research provide opportunity for further directions of investigation. The inclusion of the lateral aspects of the annulus fibrosus after arthroplasty would likely increase model stability and reduce hyper-mobility. Clinical results indicate that this is a more appropriate representation, as hyper-mobility in extension is not observed [8]. Additionally, surgical protocol for the ProDisc-C calls for retention of the uncinate processes, which is physically meaningful only if the uncinate processes are able to interact with the adjacent vertebra.

While the presence of toe region and pretension in the ligaments of the lower cervical spine are known, their magnitude and behavior are not well-understood. Mechanical testing of these factors may improve the predictive accuracy of the finite element models. Additionally, the specification of the behavior of the anterior longitudinal ligament and posterior longitudinal ligament in the models described did not account for the change in intact length of the elements due to endplate preparation.

The representation of the facet capsular ligament using a single nonlinear spring element appeared to be fairly appropriate for the deformations predicted physiologically. However, the arthroplasty models under extension secondary to implant disarticulation predict a different displacement mode, with a shift in the center of rotation from the implant puck center of curvature toward the posterior aspect of the facets. Under this deformation mode, the facet ligament representation under-predicts tension in the ligament, and more importantly, the effect of ligament tension on extension rotation is greatly reduced. It is advisable to represent the facet capsular ligament using either anisotropic two-dimensional elements, or a collection of a larger number of one-dimensional spring elements, in order to better represent the ligament behavior under extension. The other ligaments do not exhibit this problematic behavior.

Post-operative changes in disc height and sagittal alignment are directly affected by surgical techniques. Specifically, distraction distance and sagittal alignment during endplate preparation affect implant size selection and post-operative sagittal alignment and antero-posterior load sharing [31]. The surgical technique modeled in this work represented maintenance of intact endplate orientation during endplate preparation with no change in disc height using the Size 2 implant. Investigation of the effects of these additional variables would contribute to the understanding of optimal clinical techniques.

References

1. Abramowitch S D. An improved method to analyze the stress relaxation of ligaments following a finite ramp time based on the quasi-linear viscoelastic theory. J Biomech Eng. 2004;126(1):92-97.

2. Adams M. Stress Distributions Inside Intervertebral Discs: The Effects Of Age And Degeneration. Journal of Bone and Joint Surgery. British Volume 1996;78B(6):965-972.

3. Armstrong CG. Variations In The Intrinsic Mechanical Properties Of Human Articular Cartilage With Age, Degeneration, And Water Content. J Bone Joint Surg Am. 1982;64(1):88-94.

4. Ateshian G. Finite deformation biphasic material properties of bovine articular cartilage from confined compression experiments. Journal of Biomechanics 1997;30(11):1157-1164.

5. Bass E. Biaxial testing of human annulus fibrosus and its implications for a constitutive formulation. Annals of biomedical engineering 2004;32(9):1231-1242.

6. Bass C. Failure properties of cervical spinal ligaments under fast strain rate deformations. Spine 2007;32(1):E7-E13.

7. Battie M. Lumbar disc degeneration: Epidemiology and genetics. Journal of Bone and Joint Surgery. American Volume 2006;88A:3-9.

8. Bergatoni R. Early results after ProDisc-C cervical disc replacement. J Neurosurg: Spine 2005;2:403–410

9. Borden A. The Normal Cervical Lordosis. Radiology 1960;74(5):806-809

10. Bowden A E. Quality of motion considerations in numerical analysis of motion restoring implants of the spine. Clinical Biomechanics 2008;23(5):536-544.

11. Brolin K. Development of a Finite Element Model of the Upper Cervical Spine and a Parameter Study of Ligament Characteristics. Spine 2004;29(4):376.

12. Carter D. Anisotropic analysis of strain rosette information from cortical bone. Journal of Biomechanics 1978;11(4):199-202.

13. Carter D. Mechanical Properties And Composition Of Cortical Bone. Clinical orthopaedics and related research 1978;(135):192-217

14. Carter D. The Compressive Behavior of Bone As A Two-Phase Porous Structure. J Bone Joint Surg Am. 1977;59(7):954-62.

15. Cassidy J. Hierarchical structure of the intervertebral disc. Connective tissue research 1989;23(1):75-88.

16. Cassidy J. Response of the hierarchical structure of the intervertebral disc to uniaxial compression. Journal of materials science. Materials in medicine 1990;1(2):69-69.

17. Chahine N O. Anisotropic strain-dependent material properties of bovine articular cartilage in the transitional range from tension to compression. Journal of Biomechanics 2004;37(8):1251-1261.

18. Chazal, J. (1985). Biomechanical properties of spinal ligaments and a histological study of the supraspinal ligament in traction. Journal of Biomechanics, 18(3), 167-176.

19. Ciarelli M. Evaluation of orthogonal mechanical properties and density of human trabecular bone from the major metaphyseal regions with materials testing and computed tomography. Journal of orthopaedic research 1991;9(5):674-682.

20. Clausen J. Uncinate processes and Luschka joints influence the biomechanics of the cervical spine: Quantification using a finite element model of the C5-C6 segment. Journal of orthopaedic research 1997;15(3):342-347.

21. Crawford N. Unilateral cervical facet dislocation: Injury mechanism and biomechanical consequences. Spine 2002;27(17):1858-1863.

22. Cuppone M. The Longitudinal Young's Modulus Of Cortical Bone In The Midshaft Of Human Femur And Its Correlation With Ct Scanning Data. Calcified tissue international 2004;74(3):302-309.

23. Diangelo DJ. An improved biomechanical testing protocol for evaluating spinal arthroplasty and motion preservation devices in a multilevel human cadaveric cervical model. Neurosurgical focus 2004;17(3):1.

24. Diangelo DJ. In vitro biomechanics of cervical disc arthroplasty with the ProDisc-C total disc implant. Neurosurgical focus 2004;17(3):44.

25. Duggal N. Early clinical and biomechanical results following cervical arthroplasty. Neurosurgical focus 2004;17(3):62.

26. Duncan N. Experimental Validation of A Porohyperelastic Finite Element Model Of The Annulus Fibrosus In: Middleton J, Jones ML, Pande GN, eds. Computer Methods in Biomechanics and Biomedical Engineering. Amsterdam: Gordon and Breach, 1998

27. Ebara S. Tensile Properties Of Nondegenerate Human Lumbar Annulus Fibrosus. Spine 1996;21(4):452-461

28. Elliott D M. A linear material model for fiber-induced anisotropy of the anulus fibrosus. Journal of biomechanical engineering 2000;122(2):173-179.

29. Fagan M. Patient-specific spine models. Part 1: Finite element analysis of the lumbar intervertebral disc - A material sensitivity study. Proceedings of the Institution of Mechanical Engineers. Part H, Journal of engineering in medicine 2002;216(5):299-314.

30. Ferguson S J. Fluid flow and convective transport of solutes within the intervertebral disc. Journal of Biomechanics 2004;37(2):213-221.

31. Fong S. Design Limitations of a Bryan Disc Arthroplasty. Spine Journal 2006;6(3):233-241

32. Frobin W. Precision Measurement Of Disc Height, Vertebral Height And Sagittal Plane Displacement From Lateral Radiographic Views Of The Lumbar Spine. Clinical Biomechanics 1997;12:S1-S64

33. Frobin W. Vertebral height, disc height, posteroanterior displacement and dens-atlas gap in the cervical spine: precision measurement protocol and normal data. Clinical Biomechanics 2002;17(6):423-431.

34. Fujita Y. Radial tensile properties of the lumbar annulus fibrosus are site and degeneration dependent. Journal of orthopaedic research 1997;15(6):814-819.

35. Gentleman E. Mechanical characterization of collagen fibers and scaffolds for tissue engineering. Biomaterials 2003;24(21):3805-3813.

36. Gray H. Gray's Anatomy, 20th Edition. Lewis W. (Ed). Philadelphia: Lea & Febiger. 1918

37. Guan Y. Automating 3D meshing method for patient-specific modeling. Biomedical sciences instrumentation 2006;42:199-204.

38. Guan Y. Validation of a clinical finite element model of the human lumbosacral spine. Medical & biological engineering & computing 2006;44(8):633-641.

39. Guerin H A. Degeneration affects the fiber reorientation of human annulus fibrosus under tensile load. Journal of Biomechanics 2006;39(8):1410-1418.

40. Guo Z. A composites-based hyperelastic constitutive model for soft tissue with application to the human annulus fibrosus. Journal of the Mechanics and Physics of Solids 2006;54(9):1952-1971.

41. Guo Z. Large deformation response of a hyperelastic fibre reinforced composite: Theoretical model and numerical validation. Composites. Part A, Applied science and manufacturing 2007;38(8):1842-1851.

42. Guo Z. Mechanical response of neo-Hookean fiber reinforced incompressible nonlinearly elastic solids. International journal of solids and structures 2007;44(6):1949-1969

43. Ha S K. Finite element modeling of multi-level cervical spinal segments (C3-C6) and biomechanical analysis of an elastomer-type prosthetic disc. Medical engineering & physics 2006;28(6):534-541.

44. Haas M. The routine use of radiographic spinal displacement analysis: A dissent. Journal of manipulative and physiological therapeutics 1999;22(4):254-259.

45. Harrison D. Comparisons of lordotic cervical spine curvatures to a theoretical ideal model of the static sagittal cervical spine. Spine 1996;21(6):667-675.

46. Harrison D. Sitting biomechanics part I: Review of the literature. Journal of manipulative and physiological therapeutics 1999;22(9):594-609.

47. Hartwig E. In vitro low-speed side collisions cause injury to the lower cervical spine but do not damage alar ligaments. European spine journal 2004;13(7):590.

48. Heitplatz, P. A 3-dimensional large deformation FEA of a ligamentous C4–C7 spine unit. Third International Symposium on Computer Methods in Biomechanics and Biomedical Engineering, Barcelona, Spain. 1998, pp. 387–394

49. Helgason B. Mathematical relationships between bone density and mechanical properties: A literature review. Clinical Biomechanics 2008;23(2):135-146.

50. Heuer F. The relation between intervertebral disc bulging and annular fiber associated strains for simple and complex loading. Journal of Biomechanics 2008;41(5):1086-1094.

51. Hickey DS. Collagen fibril diameters and elastic fibres in the annulus fibrosus of human fetal intervertebral disc. Journal of anatomy 1981;133(Pt 3):351.

52. Hickey DS. X-ray diffraction studies of the arrangement of collagenous fibres in human fetal intervertebral disc. Journal of anatomy 1980;131(Pt 1):81.

53. Hitchcock R. In vitro study of shear force on interbody implants. Journal of spinal disorders & techniques 2006;19(1):32-36.

54. Holzapfel G. Single lamellar mechanics of the human lumbar anulus fibrosus. Biomechanics and modeling in mechanobiology 2005;3(3):125-140.

55. Horton W. Further Observations On The Elastic Mechanism Of The Intervertebral Disc. Journal of Bone and Joint Surgery. British Volume 1958;40(3):552-557.

56. Hsieh A H. Dependence of mechanical behavior of the murine tail disc on regional material properties: A parametric finite element study. Journal of biomechanical engineering 2005;127(7):1158-1167.

57. Hsu E. Diffusion tensor microscopy of the intervertebral disc anulus fibrosus. Magnetic resonance in medicine 1999;41(5):992-999.

58. Ishii T. Kinematics of the subaxial cervical spine in rotation in vivo three-dimensional analysis. Spine 2004;29(24):2826-2831.

59. Jaffar A. Morphology Of The Foramen Transversarium: A Correlation With Causative Factors. Al-Kindy Col Med J 2004;2(1):61-64

60. Joshi A. Mechanical Behavior Of The Human Lumbar Intervertebral Disc With Polymeric Hydrogel Nucleus Implant: An Experimental And Finite Element Study. Unpublished thesis (PhD). 2004. Drexel University

61. Kandziora F. Comparison between sheep and human cervical spines - An anatomic, radiographic, bone mineral density, and biomechanical study. Spine 2001;26(9):1028-1037.

62. Katsuura A. Kyphotic malalignment after anterior cervical fusion is one of the factors promoting the degenerative process in adjacent intervertebral levels. European spine journal 2001;10(4):320-324.

63. Keller TS. Influence of spine morphology on intervertebral disc loads and stresses in asymptomatic adults: implications for the ideal spine. The spine journal 2005;5(3):297.

64. Klisch S M. A bimodular theory for finite deformations: Comparison of orthotropic second-order and exponential stress constitutive equations for articular cartilage. Biomechanics and modeling in mechanobiology 2006;5(2):90-101.

65. Klisch S M. A special theory of biphasic mixtures and experimental results for human annulus fibrosus tested in confined compression. Journal of biomechanical engineering 2000;122(2):180-188.

66. Klisch S M. Application of a fiber-reinforced continuum theory to multiple deformations of the annulus fibrosus. Journal of Biomechanics 1999;32(10):1027-1036.

67. Kumaresan S. Finite element analysis of the cervical spine: A material property sensitivity study. Clinical Biomechanics 1999;14(1):41-53.

68. Kumaresan S. Finite element modeling of spinal ligaments. American Society of Mechanical Engineers, Bioengineering Division (Publication) BED 1999;42:281-282.

69. Kumaresan S. Finite element modeling of the cervical spine: Role of intervertebral disc under axial and eccentric loads. Medical engineering & physics 1999;21(10):689-700.

70. Le H. Historical review of cervical arthroplasty. Neurosurgical focus 2004;17(3):1.

71. Li H. Intervertebral disc biomechanical analysis using the finite element modeling based on medical images. Computerized medical imaging and graphics 2006;30(6):363-370.

72. Yin L. A homogenization model of the annulus fibrosus. Journal of Biomechanics 2005;38(8):1674-1684.

73. Lind B. Normal Range Of Motion Of The Cervical Spine. Archives of physical medicine and rehabilitation 1989;70(9):692-695.

74. Lotz J. Mechanobiology of the intervertebral disc. Biochemical society transactions 2002;30:853-858.

75. McNally D. An analytical model of intervertebral disc mechanics. Journal of Biomechanics 1995;28(1):53-68.

76. Mercer SR. Morphology Of The Cervical Intervertebral Disc: Implications For Mckenzie'S Model Of The Disc Derangement Syndrome. Manual therapy 1996;1(2):76.

77. Moroney S. Load-displacement properties of lower cervical spine motion segments. Journal of Biomechanics 1988;21(9):769-779.

78. Myklebust J. Tensile Strength of Spinal Ligaments. Annual International Conference of the IEEE Engineering in Medicine and Biology - Proceedings 1983;:11-11.

79. Nabhan A. Disc replacement using Pro-Disc C versus fusion: a prospective randomised and controlled radiographic and clinical study. European spine journal 2007;16(3):423-430.

80. Nachemson A. In Vivo Measurements Of Intradiscal Pressure: Discometry, A Method For The Determination Of Pressure In The Lower Lumbar Discs. Journal of Bone and Joint Surgery 1964;46:1077-1092

81. Nachemson A. Measurement of intradiscal pressure. Acta Orthop Scand 1959; 28: 269-289

82. Nachemson AL, Evans JH. Some mechanical properties of the third human lumbar interlaminar ligament (ligamentum flavum). Journal of Biomechanics 1968;1(3):211-20.

83. Nalla R. Mechanistic fracture criteria for the failure of human cortical bone. Nature materials 2003;2(3):164-168.

84. Natarajan R. Recent advances in analytical modeling of lumbar disc degeneration. Spine 2004;29(23):2733-2741.

85. Noailly J. Finite element study of a novel intervertebral disc substitute. Spine 2005;30(20):2257-2264.

86. Onan O A. Use of computed tomography image processing for mapping of human cervical facet surface geometry. Medical engineering & physics 1998;20(1):77-81.

87. Oskouian R. The Future Of Spinal Arthroplasty: A Biomaterial Perspective. Neurosurg Focus 2004;17(3):E2

88. Pal G. The orientation of the articular facets of the zygapophyseal joints at the cervical and upper thoracic region. Journal of anatomy 2001;198:431-441.

89. Pérez del Palomar A. An accurate finite element model of the cervical spine under quasi-static loading. Journal of Biomechanics 2008;41(3):523-531.

90. Panjabi M. A study of stiffness protocol as exemplified by testing of a burst fracture model in sagittal plane. Spine 2000;25(21):2748-2754.

91. Panjabi M. Articular facets of the human spine. Quantitative three-dimensional anatomy. Spine 1993; 18: 1298–310

92. Panjabi M. Cervical Human Vertebrae: Quantitative Three-Dimensional Anatomy Of The Middle And Lower Regions. Spine 1991;16:861.

93. Panjabi M M. Hybrid multidirectional test method to evaluate spinal adjacent-level effects. Clinical Biomechanics 2007;22(3):257-265.

94. Panjabi M. Mechanical properties of the human cervical spine as shown by three-dimensional load-displacement curves. Spine 2001;26(24):2692-2700.

95. Panjabi M. Physiologic Strains In The Lumbar Spinal Ligaments: An In Vitro Biomechanical Study. Spine 1982; 7(3):192-203

96. Panjabi M. The cortical shell architecture of human cervical vertebral bodies. Spine 2001;26(22):2478-2484.

97. Panjabi M. Three-dimensional load-displacement curves due to forces on the cervical spine. Journal of orthopaedic research 1986;4(2):152-161.

98. Peng X. An anisotropic hyperelastic constitutive model with fiber-matrix shear interaction for the human annulus fibrosus. Journal of applied mechanics 2006;73(5):815-824.

99. Pickett G. Effects Of A Cervical Disc Prosthesis On Segmental And Cervical Spine Alignment. Neurosurgical Focus 2004; 17(3):30-34

100. Schmitz B. Regional Variations in the Thickness of Cervical Spine Endplates as Measured by Computed Tomography. Acta radiologica 2004;45(1):53-58.

101. Pooni J. Comparison Of The Structure Of Human Intervertebral Disks In The Cervical, Thoracic And Lumbar Regions Of The Spine. Surg and rad anat 1986;8(3):175-182.

102. Porchet F. Clinical Outcomes With The Prestige II Cervical Disc: Preliminary Results From A Prospective Randomized Clinical Trial. Neurosurgical Focus 2004;17(3):E6

103. Przybylski G. Human anterior and posterior cervical longitudinal ligaments possess similar tensile properties. Journal of orthopaedic research 1996;14(6):1005-1008.

104. Puttlitz C. A finite element investigation of upper cervical instrumentation. Spine 2001;26(22):2449-2455.

105. Puttlitz C. Biomechanical rationale for the pathology of rheumatoid arthritis in the craniovertebral junction. Spine 2000;25(13):1607-1616.

106. Puttlitz C. Intervertebral disc replacement maintains cervical spine kinetics. Spine 2004;29(24):2809-2814.

107. Reilly D. The Mechanical Properties of Cortical Bone. J Bone Joint Surg Am 1974;56:1001-1022

108. Rho J. Relations of mechanical properties to density and CT numbers in human bone. Medical engineering & physics 1995;17(5):347-355.

109. Richter M. Load-displacement properties of the normal and injured lower cervical spine in vitro. European spine journal 2000;9(2):104-108.

110. Ritchie R. A fracture mechanics and mechanistic approach to the failure of cortical bone. Fatigue & fracture of engineering materials & structures 2005;28(4):345-371.

111. Robertson J. Long-Term Outcome After Implantation Of The Prestige I Disc In An End-Stage Indication: 4-Year Results From A Pilot Study. Neurosurg Focus 2004;17(3):E10

112. Rohlmann A. Analysis of the influence of disc degeneration on the mechanical behaviour of a lumbar motion segment using the finite element method. Journal of Biomechanics 2006;39(13):2484-2490.

113. Rohlmann A. Determination of trunk muscle forces for flexion and extension by using a validated finite element model of the lumbar spine and measured in vivo data. Journal of Biomechanics 2006;39(6):981-989.

114. Schinagl R. Depth-dependent confined compression modulus of full-thickness bovine articular cartilage. Journal of orthopaedic research 1997;15(4):499-506.

115. Schmidt H. Application of a new calibration method for a three-dimensional finite element model of a human lumbar annulus fibrosus. Clinical Biomechanics 2006;21(4):337-344.

116. Schmidt H. The risk of disc prolapses with complex loading in different degrees of disc degeneration - A finite element analysis. Clinical Biomechanics 2007;22(9):988-998.

117. Schmitz B. Regional Variations in the Thickness of Cervical Spine Endplates as Measured by Computed Tomography. Acta radiologica 2004;45(1):53-58.

118. Sekhon L. Cervical Arthroplasty In The Management Of Spondylotic Myelopathy: 18-Month Results. Neurosurg Focus 2004;17(3):E8

119. Sharma M. Role of Ligaments And Facets In Lumbar Spinal Stability. Spine 1995;20(8):887-900.

120. Shim V. Dynamic Tensile Testing of Ligaments from the Human Cervical Spine Proceedings of the 2005 SEM Ann Conf and Expo on Exp and App Mech. 2005. 141-148

121. Shin D S. Biomechanical study of lumbar spine with dynamic stabilization device using finite element method. Computer aided design 2007;39(7):559-567.

122. Shirazi-Adl A. Mechanical Response Of A Lumber Motion Segment In Axial Torque Alone And Combined With Compression. Spine 1986;11(9):914-927

123. Shirazi-Adl A. On the fibre composite material models of disc annulus - Comparison of predicted stresses. Journal of Biomechanics 1989;22(4):357-365.

124. Smith H. Cervical Arthroplasty: Material Properties. Neurosurg Focus 2004;17:15–21

125. Tan J. Computational Modelling Of The Intervertebral Disc Using Abaqus. In Computer Methods in Biomechanics and Biomedical Engineering 2. 1999. By J. Middleton, M. L. Jones, G. N. Pande ;8:339

126. Teo E. Evaluation of the role of ligaments, facets and disc nucleus in lower cervical spine under compression and sagittal moments using finite element method. Medical engineering & physics 2001;23(3):155-164.

127. Tkaczuk H. Tensile Properties of Human Lumbar Longitudinal Ligaments. Acta orthopaedica Scandinavica 1968;S:8.

128. Ulrich, D., Bone density and microstructure - New methods to determine bone quality and fracture risk. In: Middleton, J., Jones, M. L., Pande, G. N., (Eds.), Computer Methods in Biomechanics & Biomedical Engineering. Gordon and Breach, UK. 1997b.

129. Urbina A. Proceedings of the 2005 SEM Annual Conference and Exposition on Experimental and Applied Mechanics. 2005. 955-966 p.

130. Wagner D. Theoretical model and experimental results for the nonlinear elastic behavior of human annulus fibrosus. Journal of orthopaedic research 2004;22(4):901-909.

131. Wang Z. Computational biomechanical modelling of the lumbar spine using marching-cubes surface smoothened finite element voxel meshing. Computer methods and programs in biomedicine 2005;80(1):25-35.

132. Weinhoffer S. Intradiscal Pressure Measurements Above An Instrumented Fusion – A Cadaveric Study. Spine 1995;20(5):526-531.

133. Wheeldon J A. Experimental flexion/extension data corridors for validation of finite element models of the young, normal cervical spine. J of Biomech 2006;39(2):375-380.

134. Wilson W. A fibril-reinforced poroviscoelastic swelling model for articular cartilage. Journal of Biomechanics 2005;38(6):1195-1204.

135. Wilson W. A comparison between mechano-electrochemical and biphasic swelling theories for soft hydrated tissues. J of Biomech Eng 2005;127(1):158-165.

136. Womack W. Lower cervical spine facet cartilage thickness mapping. Osteoarthritis and Cartilage 2008;16(9):1018-1023.

137. Wright T. Tensile testing of bone over a wide range of strain rates: Effects of strain rate, microstructure and density. 1976;14(6):671-680.

138. Wu H. Mechanical behavior of the human annulus fibrosus. Journal of Biomechanics 1976;9(1):1-7.

139. Yang L. Mechanical properties of single electrospun collagen type I fibers. Biomaterials 2008;29(8):955-962.

140. Yang Q. Re-evaluating the toughness of human cortical bone. Bone 2006;38(6):878-887.

141. Yoganandan N. Anatomic study of the morphology of human cervical facet joint. Spine 2003;28(20):2317-2323.

142. Yoganandan N. Biomechanics of the cervical spine. Part 2. Cervical spine soft tissue responses and biomechanical modeling. Clinical Biomechanics 2001;16(1):1-27.

143. Yoganandan N. Finite element applications in human cervical spine modeling. Spine 1996;21(15):1824-1834.

144. Yoganandan N. Geometric and mechanical properties of human cervical spine ligaments. Journal of biomechanical engineering 2000;122(6):623-629.

145. Youdas J. Nomal Range Of Motion Of The Cervical Spine: An Initial Goniometric Study. Phys Ther 1992; 72(11):770-780

146. Youdas J. Reliability of measurements of cervical spine range of motion - comparison of three methods. Phys Ther 1991; 71: 98-106.

147. Yu S. Progressive and Regressive Changes In The Nucleus Pulposus. 2. The Adult. Radiology 1988;169(1):93-97.

148. Zander T. Influence of ligament stiffness on the mechanical behavior of a functional spinal unit. Journal of Biomechanics 2004;37(7):1107-1111.

149. Zhang S. Subtetrahedral Test For The Positive Jacobian Of Hexahedral Elements. 2005. www.math.udel.edu/~szhang

150. Zioupos P. Changes in the stiffness, strength, and toughness of human cortical bone with age. Bone 1998;22(1):57-66.

Appendix A – Facet Cartilage Thickness Mapping

Osteoarthritis and Cartilage (2008) ■■, ■■■–■■■

doi:10.1016/j.joca.2008.01.007

Osteoarthritis and Cartilage

International Cartilage Repair Society

OARSI OSTEOARTHRITIS RESEARCH SOCIETY INTERNATIONAL

Lower cervical spine facet cartilage thickness mapping

W. Womack B.S., D. Woldtvedt and C. M. Puttlitz Ph.D., Co-Director, Assistant Professor*
Orthopaedic Bioengineering Research Laboratory, Department of Mechanical Engineering, Colorado State University, Fort Collins, CO, United States

Summary

Objective: Finite element (FE) models of the cervical spine have been used with increasing geometric fidelity to predict load transfer and range of motion (ROM) for normal, injured, and treated spines. However, FE modelers frequently treat the facet cartilage as a simple slab of constant thickness, impeding the accuracy of FE analyzes of spine kinematics and kinetics. Accurate prediction of facet joint contact forces and stresses, ROM, load transfer, and the effects of facet arthrosis require accurate representation of the geometry of the articular cartilage of the posterior facets. Previous research has described the orientations of the facet surfaces, their size and aspect ratio, and mean and maximum thickness. However, the perimeter shape of the cartilaginous region and the three-dimensional distribution of cartilage thickness remain ill-defined. As such, it was the intent of this research to further quantify these parameters.

Method: Vertebrae from seven fresh-frozen unembalmed human cadavers were serially sectioned and the osteochondral interface and the articulating surface of each facet on each slice were identified. The cartilage thickness was recorded at nine equidistant points along the length of each facet. It was observed that facets tended to have elliptic or ovoid shapes, and best-fit ovoid perimeter shapes were calculated for each facet. The thickness distribution data were used to represent the entire three-dimensional cartilage distribution as a function of one variable, and a thickness distribution function was optimized to fit the thickness distribution. The antero-posterior and medial/lateral shifts of the thickness center relative to the geometric were calculated and reported.

Results: High correlation was observed between the ovoid perimeter shapes and the measured facet shapes in radial coordinates, indicating that the ovoid approximation is able to accurately represent the range of facet geometries observed. High correlation between the measured and fitted thickness distributions indicates that the fitting function used is able to accurately represent the range of cartilage thickness distributions observed.

Conclusion: Utilization of a more physiologic cartilage thickness distribution in FE models will result in improved representation of cervical spine kinematics and increased predictive power. The consistency observed in the thickness distribution function in this study indicates that such a representation can be generated relatively easily.

Key words: Cartilage, Thickness mapping, Cervical spine, Facet joints.

Introduction

Spinal degenerative disorders affect many people annually in the United States alone, and substantial research efforts have been expended with regard to the treatment of these disorders[1]. The posterior facet joints have been shown to play a major role in spinal diseases via cartilage degeneration, arthrosis, and traumatic failure[2]. Computational finite element (FE) models of the cervical spine have been used with increasing geometric fidelity to predict spinal load transfer and range of motion (ROM) in the normal, injured, and treated conditions. However, while the osseous geometry is easily reconstructed using quantitative Computed Tomography (qCT) data, the associated soft tissue reconstructions cannot be accomplished with reasonable fidelity using this radiographic approach[3]. As a result, FE modelers frequently simplify the facet cartilage as a simple homogenous block of constant thickness extruded from the underlying bone, which may be further simplified as a planar surface. Our preliminary data (unpublished) indicate that this modeling technique reduces the accuracy of FE analyses with respect to spine kinematics/kinetics and the predictions of internal mechanical parameters such as contact pressure, stress, strain, etc. Accurate predictions of facet joint contact forces and stresses, ROM, load transfer, and the effects of facet arthrosis require an accurate anatomic representation of the posterior facet articular cartilage geometry.

Previous research has described the orientations of the facet surfaces, their size and aspect ratio, and mean and maximum cartilage[4–6]. The antero-posterior (AP) width and thickness profiles of the facet cartilage on the mid-sagittal plane have been described as well[6]. However, a mathematical description of the entire perimeter shape of the cartilaginous region and a fully three-dimensional mapping of cartilage thickness across the entire facet surface has not been reported. Therefore, the purpose of this study was to obtain a sample of facet cartilage distributions, and from this data, provide a statistical description of the aforementioned parameters across the sample population.

*Address correspondence and reprint requests to: Dr Christian M. Puttlitz, Ph.D., Co-Director, Assistant Professor, Orthopaedic Bioengineering Research Laboratory, Department of Mechanical Engineering, 1374 Campus Delivery, Colorado State University, Fort Collins, CO 80523-1374, United States. Tel: 1 970 491 0956 (Engineering Office); Fax: 1 970 297 4150; E-mail: puttlitz@engr.colostate.edu
Received 5 September 2007; revision accepted 14 January 2008.

Methods

Vertebrae from seven fresh-frozen, unembalmed, human cadaver cervical (C3–C7) vertebral columns (mean age 42: 33–50 yrs) were used in this study. Soft tissues were removed and the individual vertebrae were isolated by resection of the intervertebral discs and synovial joints, with particular care taken not to disrupt the cartilaginous surfaces of the facets. Full hydration was maintained throughout the experiment with isotonic saline solution (8.5 g/L of ACS grade Sodium Chloride, VWR International, Westchester, PA). Each vertebra was serially sectioned in the sagittal plane from laterally to medially in 1.0 mm increments using a diamond-bladed band saw (Model 3031 CP/N, Exakt Technologies, Oklahoma City, OK) across the entire facet. Both the left and right superior and inferior articular facets were sectioned in this manner. A total of 25 vertebrae from the C3 to C7 levels were used. Levels that were observed to be damaged or degenerated were excluded.

Each slice was immediately dyed with a 1% Toluidine Blue solution (Fisher Scientific, Fair Lawn, NJ) to delineate the osteochondral boundaries of the articular cartilage. Individual slices were digitally photographed at 42 micron pixel resolution (5 Megapixel digital camera, Canon USA, Lake Success, NY) along with an accompanying scale and appropriate labels were incorporated in the images representing the source (specimen and level) and medial/lateral (ML) position of the slice so that three-dimensional reconstructions of facet geometry could be performed (Fig. 1). Consistent orientation was maintained between slices.

A custom-written image analysis algorithm, coded in Visual Basic (Microsoft Corp., Redmond, WA) traced the osteochondral interface and the articulating surface of each facet parametrically (Fig. 2). The anterior and posterior endpoints of each cartilage section were manually delineated, and the cartilage thickness was calculated and recorded at nine equidistant points along the length. The positions of the osteochondral interface and the articulating surface relative to a perpendicular bisecting line connecting the endpoints were recorded in order to describe the AP curvatures of both surfaces. This procedure was performed for each image of each facet (a total of 887 images).

The AP widths of the cartilage in each slice were registered and aligned to map the shape of the perimeter of each facet. It was observed that facets tended to have elliptic or ovoid shapes. Therefore, best-fit ovoid perimeter shapes were calculated for each facet consisting of two hemi-ellipses with identical AP widths. The ML and AP widths of each facet were recorded, as well as the ML shift (δ_L) of the ovoid centerline (defined as the ML position that corresponded to the maximum AP width) relative to the geometric center (mid-span) (Fig. 3). The medial and lateral endpoints could not be precisely identified because the facets were sectioned sagittally, resulting in a 1.0 mm resolution for detecting the ML boundaries. The best-fit boundaries were approximated by extrapolating the perimeter profile and mean thickness profile.

The best-fit perimeter for each facet provided the basis for a modified cylindrical coordinate system, located at approximately the location of maximum thickness. The thickness data were mapped from the three-dimensional point cloud (x,y,t, where t is thickness) to cylindrical coordinates (r,θ,t). A transformed radius function (r_{ratio}) was then utilized:

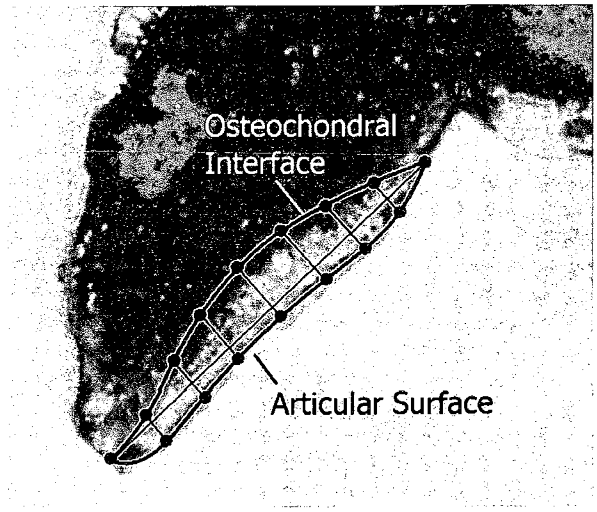

Fig. 2. Mapping of osteochondral interface and facet surface.

$$r_{ratio}(r,\theta) = \frac{r}{r_{perim}(\theta)} \tag{1}$$

where r_{perim} is the radius of the facet perimeter at orientation θ, such that $r_{ratio} = 0$ at the coordinate reference position (where thickness is maximized), and $r_{ratio} = 1$ along the perimeter. Using this technique it was possible to represent the entire three-dimensional cartilage distribution as a function of one variable (r_{ratio}). A thickness distribution function, $t_{fit}(r_{ratio})$, was optimized to fit the thickness distribution data:

$$t_{fit}(r_{ratio}) = t_{max}\left[\cos\left(\frac{\pi r_{ratio}}{2}\right)\right]^k \tag{2}$$

The parameters t_{max} and k, the maximum thickness and shape parameter respectively, were found independently for each facet. Cartilage thickness distributions and shape parameters for each facet were found by iteratively minimizing the difference between the measured and idealized thickness distributions by simultaneously varying t_{max}, k, and the AP and ML positions of the modified cylindrical coordinate reference frame (defined as the location of maximum thickness of the idealized thickness distribution). This

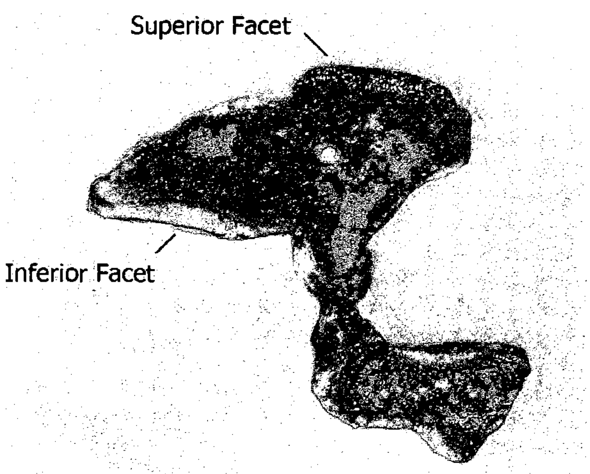

Fig. 1. Facets were serially sectioned, dyed with 1% Toluidine Blue solution, and digitally photographed.

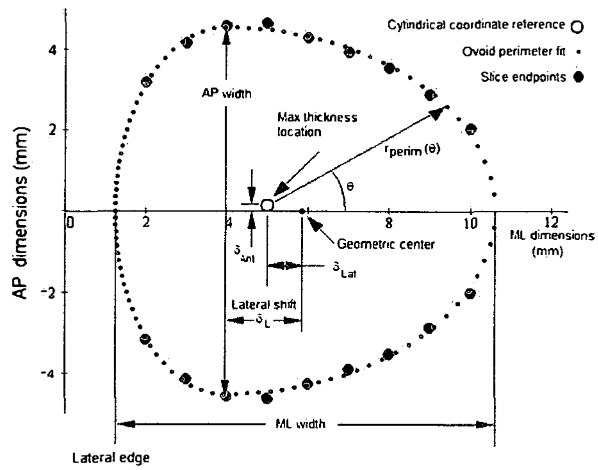

Fig. 3. Ovoid perimeter fit for a representative facet. Geometric center, ovoid centerline, and location of maximum thickness (cylindrical coordinate reference) noted.

Please cite this article in press as: Womack W et al., Lower cervical spine facet cartilage thickness mapping, Osteoarthritis Cartilage (2008), doi:10.1016/j.joca.2008.01.007

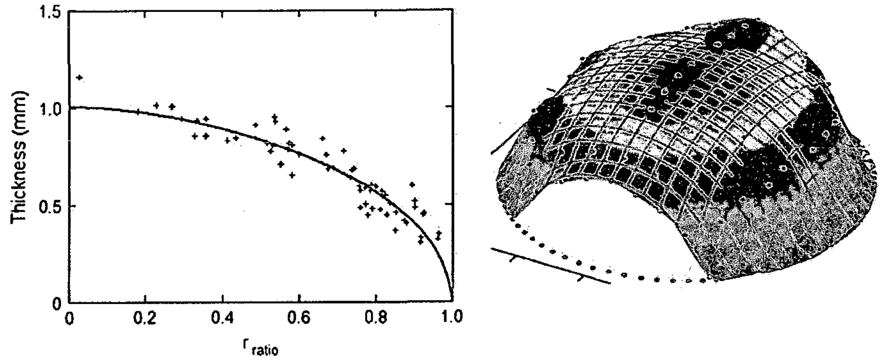

Fig. 4. Cartilage thickness distribution and fit for a representative facet, where $t_{max} = 1.00$ mm and $k = 0.48$, as a function of r_{ratio} (left) and mapped in three dimensions (right, thickness scale magnified). Color surface and dots represent measured data and the black grid represents the analytical thickness fitting function.

computational approach provided for a robust fitting function of relatively few parameters that capably represented a wide variety of perimeter shapes and thickness distributions (Fig. 4). The AP and ML shifts of the thickness center relative to the geometric center and ovoid centerline were calculated and reported (Fig. 3). Statistical significance in the aforementioned parameters was determined using paired t-tests between inferior and superior facets and unpaired t-tests between levels, where P-values less than 0.05 were considered statistically significant. Differences between inferior and superior facets as well as differences by vertebral level were examined. Pearson's correlation coefficients were calculated between measured and ovoid fit perimeter shapes in radial coordinates, as well as between fitted and measured thickness distributions.

Results

High correlation (mean $r^2 = 0.96$) was observed between the ovoid perimeter shapes and the measured facet shapes in radial coordinates (indicating that the ovoid approximation accurately represents the range of facet perimeter geometries observed) (Fig. 3). No significant differences in ML facet width were found between the inferior and superior facets, but the inferior facets were found to be slightly wider in the AP direction than their superior counterparts

Table I

Summary of collected data (means with standard deviation)

Level		Facet boundary shape				Thickness distribution			Thickness shift			
		AP width (mm)	ML width (mm)	Lateral shift δ_L (mm)	Lateral shift δ_L (%)	t_{max} (mm)	t_{mean} (mm)	k	δ_{Lat} (%)	δ_{Lat} (mm)	δ_{Ant} (%)	δ_{Ant} (mm)
Superior	C3	9.13 (1.61)	10.74 (2.26)	0.75 (1.65)	6.2 (15.3)	1.14 (0.42)	0.61 (0.22)	0.48 (0.12)	3.7 (13.8)	0.38 (1.38)	0.8 (4.5)	0.04 (0.56)
	C4	8.64 (0.84)	11.54 (2.88)	0.57 (1.51)	5.9 (14.8)	1.13 (0.24)	0.57 (0.12)	0.58 (0.10)	3.5 (17.4)	0.62 (1.71)	0.4 (3.0)	0.03 (0.32)
	C5	8.94 (0.73)	12.67 (2.40)	1.03 (1.18)	8.6 (10.0)	1.04 (0.20)	0.55 (0.10)	0.53 (0.12)	4.9 (18.1)	0.78 (2.30)	−0.8 (5.0)	−0.09 (0.57)
	C6	8.95 (0.76)	12.15 (1.43)	1.60 (0.88)	13.3 (7.6)	0.97 (0.16)	0.52 (0.08)	0.44 (0.10)	−10.8 (9.9)	−1.30 (1.30)	1.4 (6.5)	0.18 (0.74)
	C7	8.35 (0.41)	12.44 (2.63)	−0.30 (3.04)	−1.2 (22.5)	1.14 (0.17)	0.61 (0.06)	0.49 (0.15)	−2.8 (17.0)	−0.20 (2.24)	0.5 (1.1)	0.08 (0.17)
	Mean	8.87 (1.02)	11.81 (2.37)	0.86 (1.55)	7.5 (13.4)	1.08 (0.27)	0.57 (0.14)	0.51 (0.12)	0.5 (16.0)	0.15 (1.87)	0.4 (4.5)	0.04 (0.53)
Inferior	C3	9.62 (1.47)	11.84 (1.86)	0.86 (1.31)	6.6 (9.6)	0.99 (0.21)	0.49 (0.10)	0.57 (0.13)	6.7 (13.8)	0.77 (1.84)	−0.9 (5.2)	−0.10 (0.62)
	C4	9.67 (0.89)	11.60 (2.10)	0.47 (1.21)	3.9 (9.8)	1.05 (0.25)	0.55 (0.13)	0.50 (0.07)	−1.0 (11.5)	−0.07 (1.50)	0.3 (9.8)	0.04 (1.01)
	C5	9.42 (1.02)	12.28 (1.79)	1.27 (2.05)	8.5 (19.3)	1.14 (0.24)	0.58 (0.10)	0.55 (0.13)	−9.0 (23.0)	−1.22 (2.41)	−1.7 (2.3)	−0.22 (0.30)
	C6	9.24 (1.00)	12.33 (1.32)	0.67 (1.41)	5.2 (12.2)	0.94 (0.23)	0.50 (0.10)	0.47 (0.11)	−3.1 (24.2)	−0.58 (2.89)	−1.9 (5.1)	−0.26 (0.61)
	C7	9.77 (1.01)	11.55 (1.69)	−1.29 (2.71)	−11.1 (21.2)	0.89 (0.09)	0.50 (0.05)	0.36 (0.10)	−6.8 (29.9)	−0.52 (3.10)	7.5 (10.9)	0.75 (1.01)
	Mean	9.52 (1.08)	11.96 (1.76)	0.65 (1.70)	4.7 (14.3)	1.02 (0.23)	0.53 (0.11)	0.51 (0.12)	−2.0 (19.7)	−0.28 (2.28)	−0.3 (6.8)	−0.06 (0.73)
P-value		*0.011	0.489	0.135	0.070	0.116	0.081	0.379	0.278	0.236	0.467	0.488

P-values compare inferior and superior facets.

Please cite this article in press as: Womack W et al., Lower cervical spine facet cartilage thickness mapping, Osteoarthritis Cartilage (2008), doi:10.1016/j.joca.2008.01.007

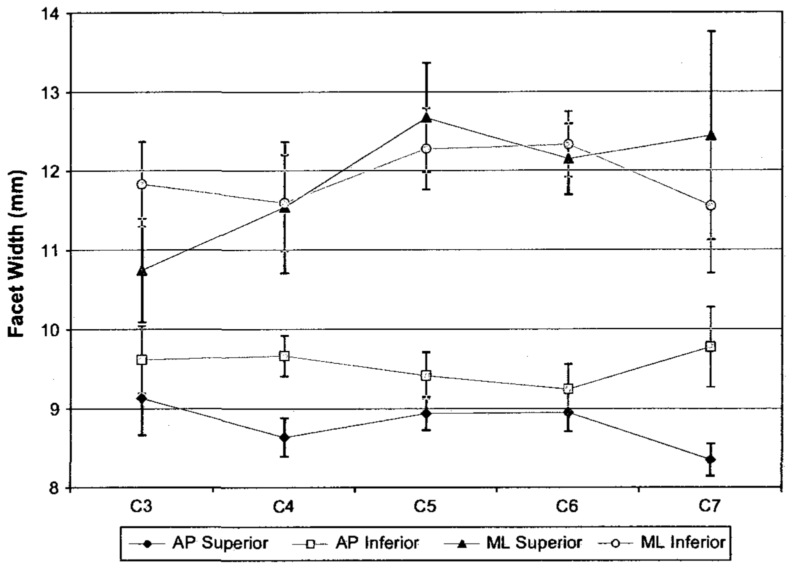

Fig. 5. Facet widths by level (mean ± standard error).

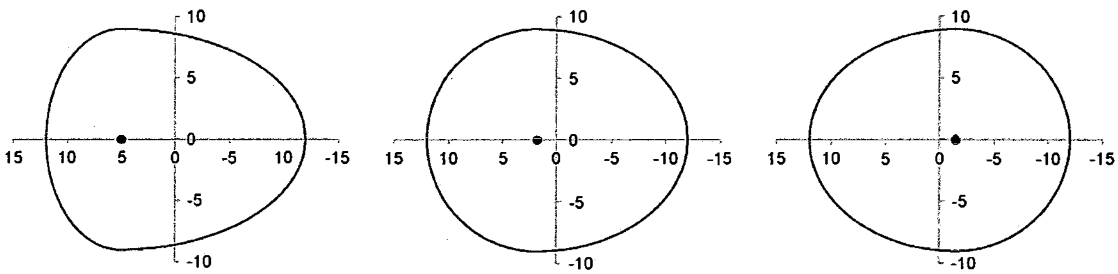

Fig. 6. Perimeter shapes for facets with ML (abscissa) and AP (ordinate) widths of 12 mm and 9 mm, respectively, showing the range of lateral shifts δ_L for the superior facets (mean ± 1 standard deviation). Lateral shifts of 21%, 8% (average shape), and −6% are depicted (left to right). Lateral edge is on the left.

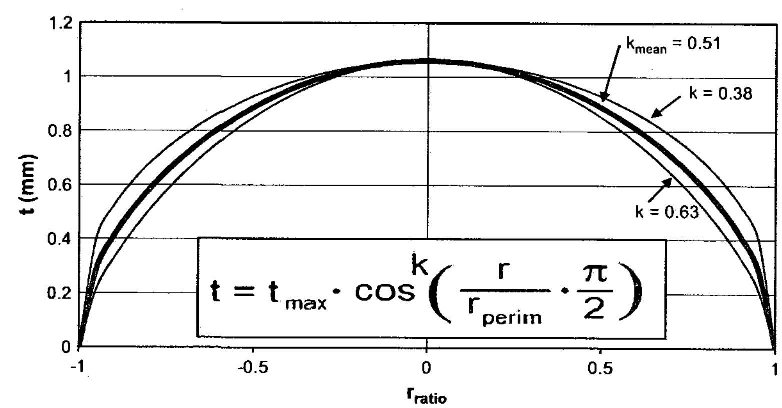

Fig. 7. Range of thickness distributions due to variation in the value of k (mean ± 1 standard deviation), when $t_{max} = 1.06$ mm. Reduced values for k represent flatter thickness distributions.

Please cite this article in press as: Womack W et al., Lower cervical spine facet cartilage thickness mapping, Osteoarthritis Cartilage (2008), doi:10.1016/j.joca.2008.01.007

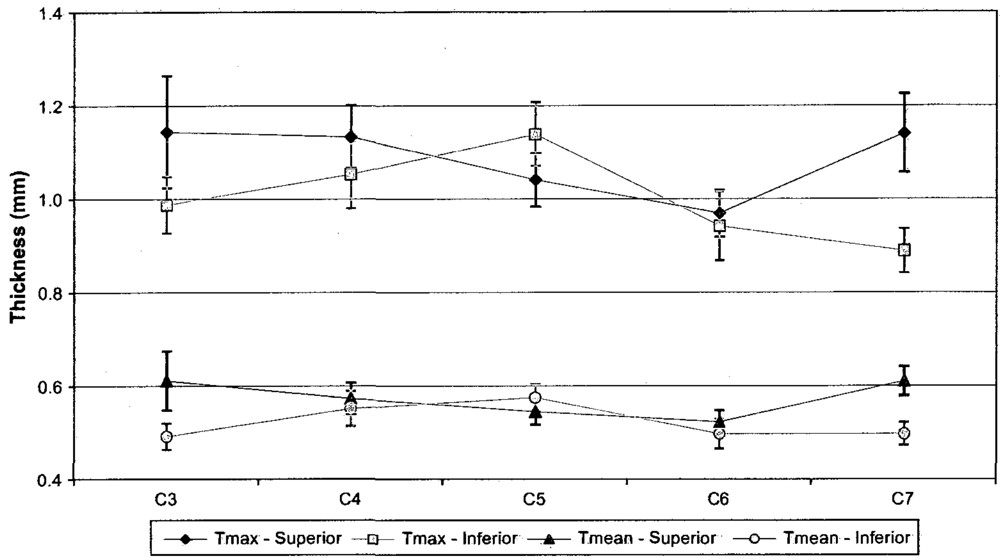

Fig. 8. Mean and peak facet cartilage thicknesses by level, with standard error.

($P=0.012$) (Table I, Fig. 5). At the C3–C6 levels, the location of maximum AP width (δ_L) was shifted somewhat laterally, whereas medial shifts were observed at C7 (Table I, Fig. 6).

The range of thickness distribution shapes represented by the observed values of k is shown in Fig. 7. No significant differences in maximum or mean thickness were observed between the superior and inferior facets overall, and the only individual level exhibiting significant differences was C7 ($P=0.03$ on maximum thickness) (Fig. 8). No significant differences in fit parameter k were observed overall (Fig. 9), and the modest decreasing trend as one moves caudally represents a slight flattening of the thickness profiles. High correlation (mean $r^2=0.97$) was also observed between the measured and fitted thickness distributions (indicating that the thickness fitting function used is able to accurately represent the range of cartilage thickness distributions observed).

No significant trends were observed in the ML and AP shifts of the location of maximum thickness relative to the geometric centers of the facets (Table I), and significant variability was observed in the location of maximum

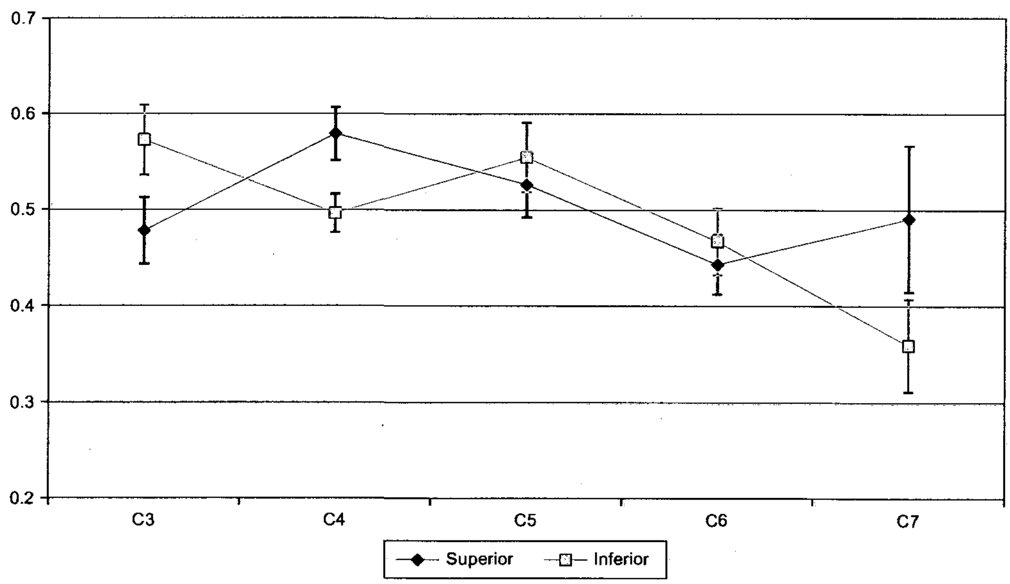

Fig. 9. Thickness distribution fit parameter k, with standard error. No significant differences were observed between inferior and superior facets overall, although differences were observed at the C3 and C4 levels ($P=0.04$ and $P=0.05$, respectively).

Please cite this article in press as: Womack W et al., Lower cervical spine facet cartilage thickness mapping, Osteoarthritis Cartilage (2008), doi:10.1016/j.joca.2008.01.007

thickness. More variation was observed in the ML direction than in the AP direction (Table I), which confirms the gross experimental observation of thickness variability between subsequent slices.

Discussion

AP facet widths observed fall within the range reported by previous researchers, but the gap between the cartilaginous boundary and the perimeter of the bony geometry of the facet reported by Yoganandan *et al.* was not found to be present on all facets[6]. Some facets exhibited a prominent gap, while others exhibited full coverage. Additionally, it was observed that the gap varied in size and presence between subsequent slices on individual facets. Facet cartilage gap was generally maximized in the mid-sagittal slice, decreasing or disappearing both medially and laterally.

The shape of the facet cartilage thickness distributions observed is in good agreement with the average mid-sagittal profile given by Yoganandan, using the mean observed value of the fit parameter $k = 0.5$; i.e., this work represents a three-dimensional generalization of the mid-sagittal case.

While the facet cartilage is generally difficult to accurately identify using radiographic methods such as qCT, the underlying osteochondral interface is generally discernable. Three-dimensional surface reconstructions based on bony geometry frequently yield a readily identifiable facet region due to the curvature of the osteochondral interface of the facets. It is anticipated that utilization of a more physiologic cartilage thickness distribution in FE models will result in greater predictive accuracy with respect to cervical spine kinematics internal mechanical parameters. The consistency observed in the thickness distribution function in this study indicates that such a representation can be generated relatively easily, using the thickness distribution function reported here and the maximum thickness from either direct measurement or literature. While limitations of this study include a limited number of cadavers and the presence of degeneration on excluded levels, the independence of the maximum cartilage thickness and the shape factor k indicate that the model may be used to represent both full and reduced thickness cartilage distributions.

It was observed that the osteochondral interfaces of the inferior facets were more concave in the sagittal plane than those of the superior facets, with the result that the inferior articulating surfaces were slightly concave, whereas the superior articulating surfaces tended to be slightly convex. The congruence of these mating surfaces is therefore a function of both the shapes of the osteochondral surfaces and the thickness distributions of the cartilage on both facets. As stated above, it is expected that facet contact pressures and their distribution, and to a lesser degree spine kinematics, will be affected by the geometry and thickness distribution of the facet cartilage. Because the facet cartilage is neither flat nor a constant thickness, it is expected that oversimplification of these geometric properties in some currently published FE models most likely results in mechanical parameter prediction artifact. Computational models of the lower cervical spine that fail to account for these factors will therefore be limited in their ability to accurately predict pressures, stresses, and strains in the zygophyseal joints.

Conflict of interest

The authors claim no conflict of interest.

Acknowledgements

The authors would like to thank Dr A.S. Turner for providing the ovine and bovine specimens. Institutional research support provided by Synthes, Inc.

References

1. Battie MC, Videman T. Lumbar disc degeneration: epidemiology and genetics. J Bone Joint Surg Am 2006;88:3–9.
2. Crawford NR, Duggal N, Chamberlain RH, Chan PS, Sonntag VHK, Dickman CA. Unilateral cervical facet dislocation: injury mechanism and biomechanical consequences. Spine 2002;27:1858–64.
3. Onan OA, Hipp JA, Heggeness MH. Use of computed tomography image processing for mapping of human cervical facet surface geometry. Med Eng Phys 1998;20:77–81.
4. Panjabi MM, Duranceau J, Goel V, Oxland T, Takata K. Cervical human vertebrae – quantitative three-dimensional anatomy of the middle and lower regions. Spine 1991;16:861–9.
5. Panjabi MM, Oxland T, Takata K, Goel V, Duranceau J, Kraq M. Articular facets of the human spine – quantitative three-dimensional anatomy. Spine 1993;18:1298–310.
6. Yoganandan N, Knowles SA, Maiman DJ, Pintar FA. Anatomic study of the morphology of human cervical facet joint. Spine 2003;28(20):2317–23.